<u>Final Report: DARPA exploratory program, MDA972-02-0010</u>

Title: Aligned Single-walled Carbon Nanotube Synthesis for Device Design

Project Period: April 1, 2002 to February 29, 2004

**Amount $350,000.**

DARPA manager: Dr. Leo Christodoulou

PI: Professor L.D. Pfefferle (Chemical Engineering) with Prof. G. L. Haller (Chemical Engineering) and Professor Mark Reed (Electrical Engineering)

Yale University, New Haven, CT

PI Contact information: E-mail: lisa.pfefferle@yale.edu
Phone: 203-488-7309

This project was highly successful demonstrating control of carbon nanotube diameter through control of the synthesis process. Mean tube diameter can be *preselected* from 0.5 to 0.9nm. A sample predominantly semiconducting with two main tubes (7,5 and 8,3), and a sample of smaller (0.5-0.6nm) and mainly metallic tubes were produced. The process also laid the ground for production of the first pure boron nanotubes. In our SWNT synthesis experiments using CO disproportionation at 6 atm and lower pressures, the Co-MCM-41 and Ni-MCM-41 catalysts produced more than 90% selectivity to SWNT with increasing yields as the pressure is increased. The key advantage of our technique is the incorporation of metals into the pore wall of the template, which allows ultra-small metal clusters to be formed and stabilized. These clusters then initiate the growth of highly uniform diameter SWNT. Examples of uniform small diameter SWNT formed with two of our catalysts are shown in Figure 1 below.
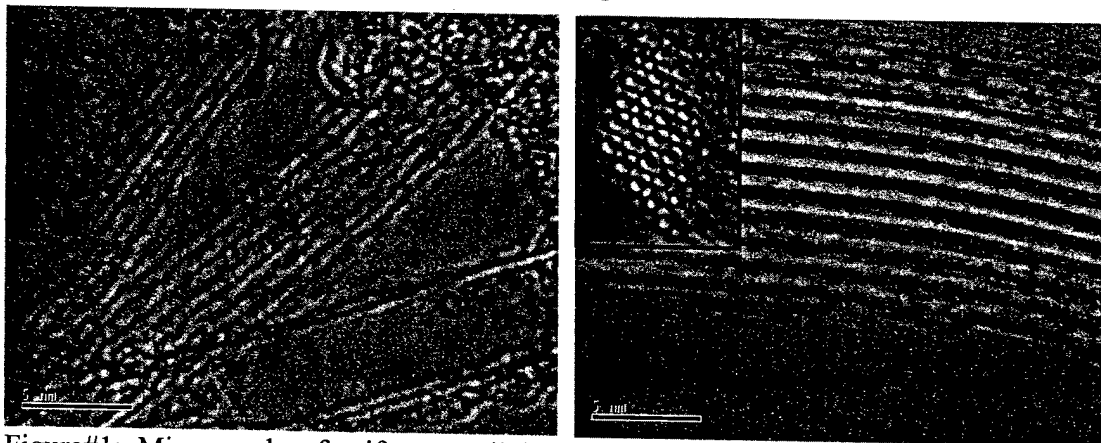
Figure#1: Micrographs of uniform small diameter SWNT from Co-MCM-41 catalysts (template pore size was 1.9nm on left and 2.85nm on right). Inset shows tube ends.

The narrow diameter distribution has been confirmed by several complementary techniques and this data is summarized on Figure #2 below for a Co-MCM-41 template. The Raman data for this sample were obtained at four excitation wavelengths from 488 to 785nm to cover the resonances of tubes with different diameters in the sample. In figure

20050303 288

#2 over 70% of the sample is in 2 specific tubes (the (8,3) and (7,5) tubes) and only two other semiconducting tubes are present on 10% level (the (7,6) and (6,5) tubes).

Smallest diameter predicted by Raman

Largest diameter predicted by Raman

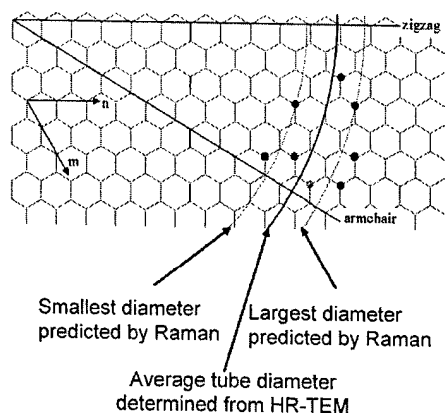Average tube diameter determined from HR-TEM

Figure #2. Distribution of SWNT diameters determined for SWNT grown in Co-MCM-41 with pores of 2.85nm. The background mesh represents the graphene sheet and the colored dots indicate the individual semiconducting tubes identified in our sample by fluorescence measurements. The straight solid lines represent the axes for wrapping the carbon net to form zigzag or armchair nanotubes. Data from DNA wrapping suggests 2 main tubes. Reaction at higher pressure will likely narrow the distribution.

Small (<0.7nm), uniform diameter SWNT have very special properties including high T semiconductors, they are the strongest 1 D material and they exhibit unusual, unpredicted electronic properties. High radius of curvature is associated with properties that vary dramatically with applied force this may also be especially advantageous for neat SWNT spinning because interactions between the tubes and packing density increases as the tube diameter decreases. To date, no economically feasible methods exist for varying tube diameter in the range < 0.9nm besides our process using cobalt incorporated MCM-41 catalytic templates.

Our process, which uses incorporation of the metal component in the pore framework, stabilizes the catalyst precursor against total reduction and sintering, allowing smaller SWNT diameter and tighter control of SWNT properties. For example, Figure #3a below shows the correlation between SWNT diameter and the template pore diameter as determined by TEM for fixed template synthesis conditions. Our results clearly show that our technique allows *pre-selected* control of SWNT diameter produced down to very small diameters.
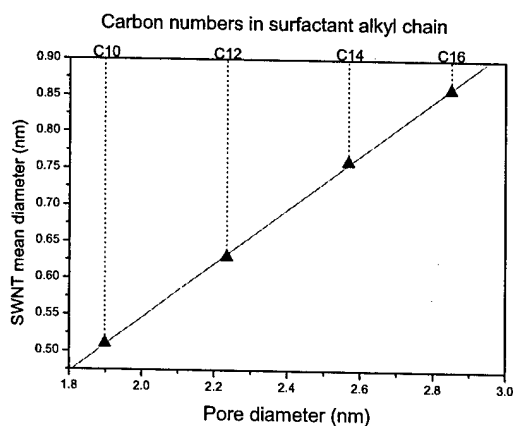

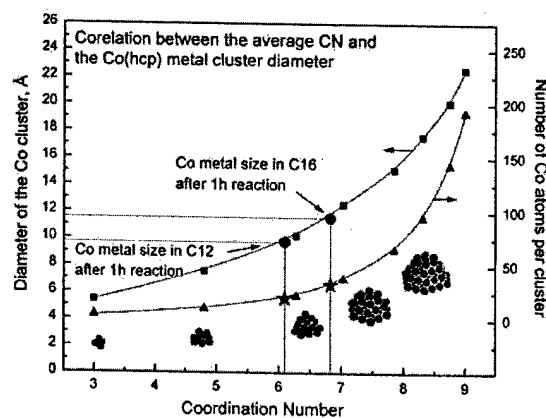Figure 3a. SWNT diameter produced with catalysts having different pore sizes.

Figure #3b. Metal cluster size from EXAFS

2

The diameters of the nanotubes we produce correlate with the template pore diameter as seen in figure #3a, but not in the 1:1 manner seen with physical templating. During our pretreatment and synthesis the catalyst precursor is partially reduced and produces ultra-small metallic clusters. The size of the metal cluster formed during pretreatment and reaction depends on the pore diameter of the MCM-41, as illustrated from our Extended X-Ray Absorption Fine Structure (EXAFS) data shown in Figure #3b. Metal particle size also depends on the chemical nature of the template wall, which can be independently controlled. A key advantage of this process is the ability to independently control the chemical composition of the template and its pore diameter. This enables control the diameter of the metallic clusters formed by reduction of the catalyst precursor, which allows tuning of their catalytic reactivity and diameter control of the SWNT produced.

Our tubes have been shown by at least two different independent characterizations to have much lower defect levels when compared with tubes from leading producers. Jia Chen (Dr. Avouris's group at IBM) ran conductivity tests of individual nanotubes. The current plateau in the I-V curve depicted in Figure#4 was expected to be at lower levels than previously tested SWNT because our tubes are of smaller diameter. Instead, they showed excellent conductivity (μV levels) postulated to be due to the low defect levels. These conclusions were also supported by tests at Dupont (Dr. Ming Zheng) showing much lower "rolling down" baseline in UV-vis spectra likely due to a lower defect level. When the (6,5) tubes were tested by redox titration a 50% greater extinction coefficient was observed for the same number of valence electrons than the next best sample from Prof. Resasco's laboratory. Our SWNT were also observed to be more resistant to oxidation, again suggesting a lower defect level.
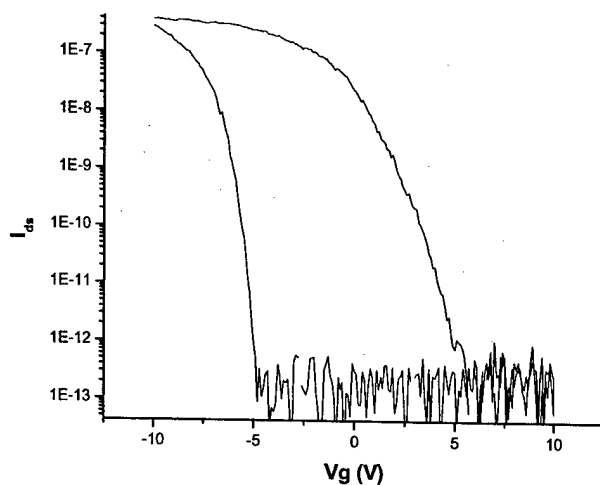

Figure #4. Transfer characteristics for a typical SWNT grown be CO disproportionation on Co-MCM-41 catalysts

A series of papers has been published that discuss diameter control, parameter optimization of the process (temperature, catalyst pretreatment, pressure, time and catalyst concentration) as well as explorations of the growth mechanism. These are detailed below.

Papers from this project:

Sangyun Lim, Dragos Ciuparu, Chanho Pak, Frank Dobek, Yuan Chen, David Harding, Lisa Pfefferle and Gary Haller, "Synthesis and Characterization of Highly Ordered Co-MCM-41 for Production of Aligned Single Walled Carbon Nanotubes (SWNT)", *J. Phys. Chem. B*, **107**(40) 2003, 11048.

D. Ciuparu, Y. Chen, S. Lim, G.L. Haller and L. Pfefferle, "Uniform-Diameter Single-Walled Carbon Nanotubes Catalytically Grown in Cobalt-Incorporated MCM-41", *J. Phys. Chem B*, **108**(2) (2004) 503.

Y. Chen, D. Ciuparu, S. Lim, G.L. Haller and L. Pfefferle, "Synthesis of Uniform-Diameter Single-Walled Carbon Nanotubes in Co-MCM-41: Effects of the Catalyst Prereduction and Nanotube Growth Temperatures", *J. Catalysis*, **225**(2) (2004) 453.

Y. Chen, D. Ciuparu, S. Lim, G.L. Haller and L. Pfefferle, "Sysnthesis of Uniform-Diameter Single-Walled Carbon Nanotubes in Co-MCM-41: Effect of CO pressure and reaction time, *J. Catalysis,* **226**(2) (2004) 351.

D. Ciuparu, Y. Chen, S. Lim, Y. Yang, G.L. Haller and L. Pfefferle, "Mechanism of Cobalt Cluster Size Control in Co-MCM-41 during Single-Wall Carbon Nanotubes Synthesis by CO Disproportionation", *J. Phys. Chem. B*, **108**(40) (2004) 15565.

S. Lim, D. Ciuparu, Y. Chen, L. Pfefferle and G.L. Haller, "Effect of Co-MCM-41 Conversion to Cobalt Silicate for Catalytic Growth of Single Wall Carbon Nanotubes", *J. Phys. Chem. B*, **108**(52) (2004) 20095.

P. Haider, Y. Chen, S. Lim, L. Haller Gary, L. Pfefferle and D. Ciuparu, "Application of the Generalized 2D Correlation Analysis to Dynamic Near-Edge X-ray Absorption Spectroscopy Data", *Journal of the American Chemical Society*, **127**(6) (2005) 1906.

P.B. Amama, S. Lim, D. Ciuparu, Y. Yang, L. Pfefferle and G.L. Haller, "Synthesis, Characterization, and Stability of Fe-MCM-41 for Production of Carbon Nanotubes by Acetylene Pyrolysis", *J. Phys. Chem. B*, **109**(7) (2005) 2645.

Yuan Chen, Dragos Ciuparu, Sangyun Lim, Gary L. Haller and Lisa Pfefferle, "The effect of the cobalt loading in Co-MCM-41 catalysts on the quality of the single wall carbon nanotubes grown by CO disproportionation", submitted to *Carbon*, 2004.

Although not part of the work of this project, the following papers were made possible by the project work:

D. Ciuparu, R.F. Klie, Y. Zhu and L. Pfefferle, "Synthesis of Pure Boron Single-Wall Nanotubes", *J. Phys. Chem. B*, **108**(13) (2004) 3967. (and related story in Nature, News in Brief, April 8, 2004).

4

Y. Li, Y. Chen, R. Xiang, D. Ciuparu, L.D. Pfefferle, C. Horvath and J.A. Wilkins, "Incorporation of Single-Wall Carbon Nanotubes into an Organic Polymer Monolithic Stationary Phase for m-HPLC and Capillary Electrochromatography", *Analytical Chemistry*, **77**(5) (2005) 1398.

S. Lim, D. Ciuparu, Y. Chen, Y. Yang, L. Pfefferle and G.L. Haller, "Pore Curvature Effect on the Stability of Co-MCM-41 and the Formation of Size-Controllable Subnanometer Co Clusters", *J. Phys. Chem. B*, **109**(6) (2005) 2285.

Placidus B. Amama, Sangyun Lim, Dragos Ciuparu, Lisa Pfefferle, Gary L. Haller, "Synthesis of highly ordered MCM-41: Engineering of pore size and optimization of silica ratios", *Microporous and Mesoporous Materials*, in press 2005.

LETTERS

Uniform-Diameter Single-Walled Carbon Nanotubes Catalytically Grown in Cobalt-Incorporated MCM-41

Dragos Ciuparu,* Yuan Chen, Sangyun Lim, Gary L. Haller, and Lisa Pfefferle

Department of Chemical Engineering, Yale University, New Haven, Connecticut 06520

Received: August 18, 2003; In Final Form: November 4, 2003

Single-walled carbon nanotubes of uniform diameter were grown in cobalt-substituted MCM-41 molecular sieves templated with C12 and C16 alkyl chains to result in pore diameters of 2.6 and 3.3 nm, respectively. The narrow diameter distribution of the tubes grown was probed by Raman, UV–visible, and NIR spectroscopy, as well as by high-resolution transmission electron microscopy. Tube diameters have been observed to vary with the size of the Co clusters formed during carbon deposition, as measured by extended X-ray absorption fine structure (EXAFS). It is proposed that the diameter of the carbon nanotubes grown in MCM-41 catalysts is controlled by the size of the metallic clusters formed in the template. Because MCM-41 catalysts of different pore diameter form Co clusters of different sizes, this mechanism can be exploited to grow carbon nanotubes of uniform, preselected diameters.

As widely reported,[1-5] carbon nanotubes exhibit technologically important electronic properties potentiating new device development. They can be found in both metallic and semiconducting structures. The structure of the single-walled nanotube (SWNT) is defined by how the graphitic sheet is aligned in the rolled up configuration. Metallic (m) nanotubes can carry extremely large current densities;[6] semiconducting (s) nanotubes can be electrically switched on and off as field-effect transistors (FETs) (e.g., ref 6). Most electronic applications of carbon nanotubes require aligned SWNTs that are reasonably homogeneous in diameter, length, and electronic properties. Odom et al.[7] used scanning tunneling microscopy (STM) to correlate atomic structure with electronic properties of SWNTs. They found that the electronic properties correlate both with the diameter and helicity (twist). This important work illustrates why control of SWNT diameter and structure is of crucial importance for the development of new electronic devices based on SWNTs.

* Corresponding author. Phone: 203-432-4383. Fax: 203-432-4387. E-mail: dragos.ciuparu@yale.edu.

The current state of the art of SWNT synthesis is given in a recent review.[8] Processes now exist that yield 90% selectivity for SWNT in scalable processes (for example, Dai and co-workers,[9,10] Resasco and co-workers,[11] Smalley and co-workers[12]). Cleaning, separation, and alignment steps are required for use in electronic applications. Due to the harsh reaction conditions required for SWNT synthesis, traditionally prepared metallic particulate catalysts will not likely lead directly to the desired very narrow diameter distributions. Catalysts, particularly metal catalysts, restructure and sinter leading to the formation of multifaceted crystals, each facet potentially initiating the growth of a SWNT and thus a spread of particle sizes and multiple nanotubes from each particle leading to heterogeneity in diameter and structure (e.g., see refs 13 and 14).

An important recent development is the use of zeolite channels as templates to synthesize SWNTs.[15-18] An intriguing finding from this zeolite work is that interactions with the channel walls during nanotube formation were observed to lead to selection of a particular nanotube structure.[17] If control could be achieved for a range of diameters, this could provide an important tool for controlling SWNT properties. Zeolites,

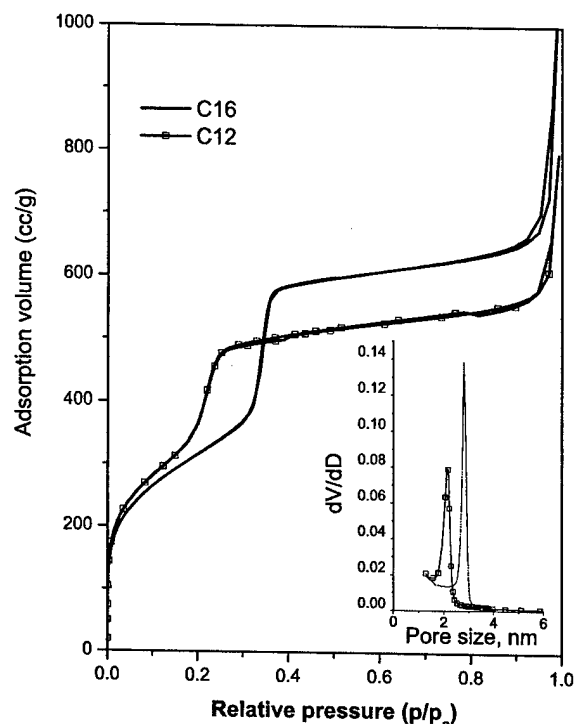**504** *J. Phys. Chem. B, Vol. 108, No. 2, 2004*

Letters

Figure 1. Physisorption isotherms measured with fresh C12 and C16 templates. The inset shows the pore size distribution derived from the desorption isotherms by the modified BJH method.[31]

Figure 2. Raman spectra recorded at different excitation wavelengths for unpurified SWNT samples grown without hydrogen prereduction in the C16 catalytic template. TEM inset shows SWNTs uniform in size evolving from the pores of the Co−MCM-41 catalyst with hydrogen prereduction.

however, because of their lack of composition and pore size flexibility, are not an ideal choice for a SWNT template. As used here, template does not imply a one to one pattern transfer of the template structure to the SWNT. Templating of the SWNTs is exercised through the influence of the pore wall on the size of the nucleating metal cluster. The ideal template material should allow independent control of both composition and channel size. The M41S class of mesoporous materials developed by Mobil[19] is ideal in that the walls are amorphous and structured pore arrangements with pore sizes from 1.5 to 4 nm can be produced independent of metal substitution in the framework (for dilute substitutions). We have found the wall thickness to be relatively uniform in this pore size regime at approximately 1 nm.

In this contribution, we demonstrate the formation of uniform-size SWNTs controllable by the properties of a cobalt-substituted template having a parallel system of pores. The nanotubes are uniform in diameter and spacing. The catalytically active site or site precursor is produced by MCM-41 framework substitution with cobalt. The catalytic component is highly dispersed in the pore wall and its oxidation state can be controllably modified by varying pretreatment conditions. The mesoporous molecular sieve used as a catalytic template for SWNT growth was produced using a surfactant-templated synthesis modified from the original Mobil method to improve structural order. The synthesis and characterization of the Co−MCM-41 is discussed elsewhere.[20] Two different Co−MCM-41 catalysts were used in this study, one with pore size by high-resolution transmission electron microscopy (HR-TEM) of 3.3 nm and the other with a pore size of 2.6 nm. The pore size distribution in the Co−MCM-41 catalysts measured by nitrogen physisorption in a static volumetric instrument Autosorb-1C (Quanta Chrome) is on the order of 0.1 nm full width at half-maximum, as observed in Figure 1. It should be mentioned that similar measurements performed with the MCM-41 templates after reduction with hydrogen at 500 °C and after carbon deposition
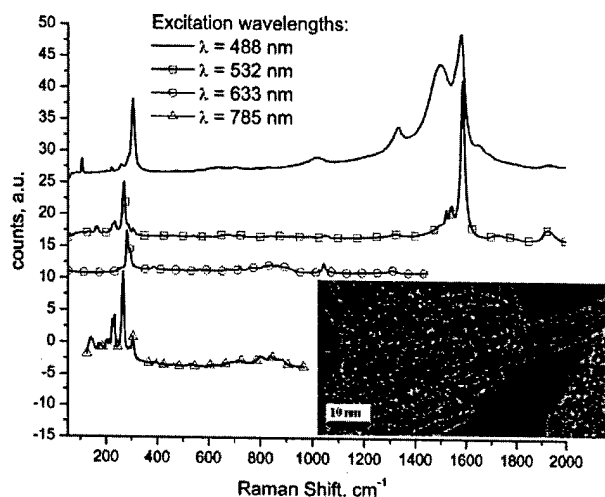
and subsequent removal by oxidation showed minor modifications of structure and pore size distribution, suggesting that these templates have good structural stability under both reduction and oxidation conditions.[20]

Single-walled carbon nanotubes were synthesized by CO disproportionation. The Co−MCM-41 catalyst was packed in a 10 mm internal diameter quartz reactor, heated in flowing oxygen to 750 °C, purged for 10 min with argon, and then reacted with CO for 2 h. In an optimized reaction strategy, before reaction the catalyst was heated in flowing hydrogen to 773 K at 20 K/min and held at that temperature for 15 min. Subsequently, the reactor was flushed with Ar, and the temperature was further raised at 20 K/min to 1023 K under flowing Ar. The Boudouard reaction was carried out for 1 h at 1023 K in a pure CO atmosphere; then the catalyst was again flushed with Ar and cooled to room temperature in Ar.

As-synthesized samples and purified carbon nanotube samples were characterized by HR-TEM and Raman, UV−vis, and near-IR spectroscopy. The purification process consisted of template removal by ultrasonication for 4 h in 48% HF to dissolve the silica and the cobalt from the sample. Nitrogen physisorption was also used to determine the diameter of the tubes removed from the catalyst and to measure the pore size distribution of the templates at different stages in the process.

The resonant Raman spectra in Figure 2 recorded at four different excitation wavelengths (488, 532, 633, and 785 nm) with a C16 catalyst without hydrogen prereduction indicate that the samples have a uniform diameter. The main peaks correspond to tube diameters ranging from 7.7 to 8.9 nm. It should be mentioned that spectra (not shown) recorded at the 532 nm excitation wavelength with a sample prepared by the optimized reaction strategy with hydrogen prereduction show a single peak at approximately 250 cm^{-1}. This indicates the nanotubes are of uniform size. This conclusion is also supported by analysis of over 60 locations on several TEM grids. An illustrative image of a tube bundle grown with a hydrogen-prereduced C16 catalyst is given in the inset of Figure 2. The inner diameter of SWNTs obtained using the optimized reaction strategy with the C16 template varied between 0.84 and 0.86 nm, while those grown on the C12 template averaged 0.67 nm in diameter. The Raman spectra shown in Figure 2 were recorded with an unpurified, as-synthesized sample without previous cleaning or any other
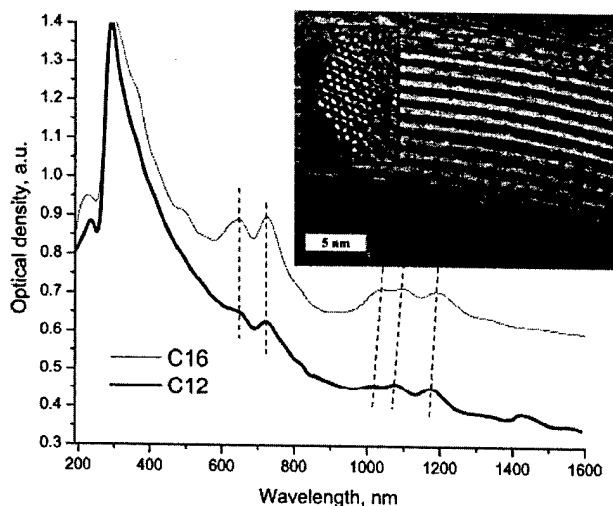
Letters

J. Phys. Chem. B, Vol. 108, No. 2, 2004 **505**

Figure 3. UV-visible and NIR spectra recorded for unpurified SWNT samples grown in C12 and C16 templates with hydrogen prereduction. TEM inset shows the uniformity of the SWNTs grown in the C12 template.

Figure 4. Tube size distribution measured for HF-purified SWNT samples by nitrogen physisorption.

form of postsynthesis treatment. These spectra also confirm high selectivity to SWNT with very little amorphous carbon: the area of the spectra indicating disordered carbon at 1350 cm^{-1} is reasonably flat. The ratio between the D band, characteristic for the disordered (amorphous) carbon, and the G band, attributed to ordered carbon, to our knowledge is much higher than those previously reported for unpurified SWNT samples.[21]

Figure 3 shows the UV—vis and near-IR spectra for the nanotubes grown in hydrogen-prereduced C12 and C16 catalysts, along with a TEM image showing the diameter uniformity of the SWNTs grown in the hydrogen-prereduced C12 template. The peak complex in the visible region was previously assigned to the second Van Hove transition of semiconducting tubes, while the peaks in the NIR region were attributed to the E_{11} interband transitions of the semiconducting tubes.[22] The blue shift of the E_{11} transition of the C12 sample in the NIR region is direct evidence for a smaller diameter of SWNTs grown in the C12 template.[22,23] However, the spectral feature in the visible domain is not shifted as much. Assignments are not necessarily definitive because adsorbates induce significant changes in the spectral features of the smaller nanotubes.

The diameter distribution measured by nitrogen physisorption on purified SWNT samples removed from the template by HF treatment is given in Figure 4. The average diameter values measured in the physisorption experiment are 0.68 and 0.76 nm for C12 and C16, respectively, thus showing smaller SWNT diameter for the template with smaller pore diameter. The differences between the physisorption measurements and the TEM results are most likely due to the assumption that the wetting angle (used in the Kelvin equation) for liquid nitrogen on carbon is zero. Most liquids with low surface tension have a smaller contact angle on graphite than on silica. Therefore, the nanotube diameter may be underestimated because it was calculated using the same angle as that used for the template material, which is mostly silica.[20] In addition, liquid nitrogen has different contact angles on walls of different pore diameters because of the pore curvature. Smaller pores contact a larger area with the nitrogen molecule than wider pores, resulting in smaller contact angle and underestimation of nanotube diameter. These nanoscale phenomena are likely responsible for the differences observed between the diameter measurements by TEM and nitrogen physisorption. Also, the relatively wider
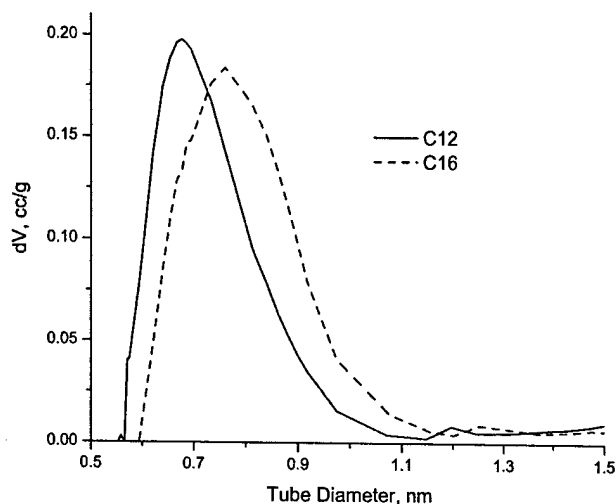
distribution of tube diameters observed in the physisorption results is most likely due to defects created in the SWNT structure during the HF treatment and to the interstitial spaces between tubes. The presence of defects may also create interstitial spaces that act as micropores during physisorption measurements.

On the basis of investigation of silica-supported Co—Mo catalysts, Resasco and co-workers[11] proposed that the high selectivity observed for Co—Mo catalysts as compared to monometallic Co catalysts is due to the stabilization effect of molybdenum, which impedes rapid Co reduction, thus leading to a slow Co reduction and formation of small Co clusters highly selective for SWNT synthesis. We propose that a similar role may be played by the silica matrix in our Co-substituted MCM-41 catalytic template.

The diameters of the SWNT produced are significantly smaller than the template pore diameter; however, the SWNT diameter correlates with the pore diameter; therefore, it is likely that control is obtained through the effect of the pore size on the size of the metal clusters formed during reduction. This is also consistent with the observation that harsher conditions are required to reduce cobalt in the MCM-41 framework and the reducibility decreases with the pore diameter. To test this hypothesis, catalyst samples previously exposed to the SWNT growth as discussed above were investigated by X-ray absorption fine structure (XAFS).

X-ray adsorption data of fresh Co—MCM-41, Co metal foil, and C12 and C16 Co—MCM-41 loaded with carbon were measured at beam line X 18-B equipped with a Si(111) crystal monochromator at the National Synchrotron Light Source at Brookhaven National Laboratory. The intensity of the incident beams (I_0) was measured with a 30 cm long ion chamber filled with pure N_2. X-ray adsorption data were collected in transmission mode by scanning from 200 eV to 16 keV above the Co K edge. The I_T value was measured with the ion chamber filled with a 4:1 N_2 in Ar mixture. Samples of approximately 45 mg of Co—MCM-41 were pressed into a rectangular wafer (ca. 1.5 cm × 1 cm) to form 0.5 mm thick pellets. The wafer was then placed between the ion chambers. The spectra were obtained by averaging three scans for each sample.

The X-ray absorption data were analyzed using the procedure described elsewhere.[24] First, the smooth isolated-atom background function was removed from the experimental X-ray absorption coefficient data by FEFFIT.[25] Then theoretical

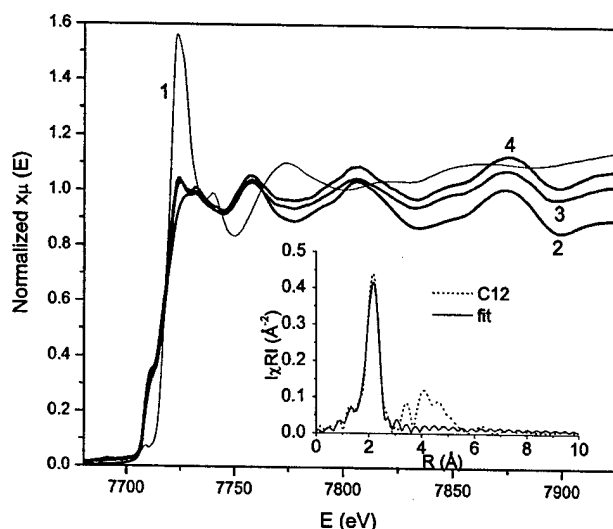**506** *J. Phys. Chem. B, Vol. 108, No. 2, 2004*

Letters

Figure 5. Near-edge spectra of Co K edge ($E_0 = 7709$ eV): (1) spectrum for the fresh Co−MCM-41; (2) spectrum for metallic cobalt foil; (3, 4) C12 and C16, respectively, Co−MCM-41 samples after SWNT growth. The inset shows an example of fitting the spectra with the model.

Figure 6. The upper limit of the diameter of the Co clusters determined from the analysis of the EXAFS spectra recorded for C12 and C16 samples exposed to pure CO at 750 °C for 1 h. Cobalt cluster sizes observed by Resasco[29] for a silica-supported Co−Mo catalyst exposed to CO at 700 °C for 30 min are given for comparison.

photoelectron scattering amplitudes and phase shifts of Co metal were calculated for a model structure. Finally, the theoretical extended X-ray absorption fine structure (EXAFS) signal of Co metal was fit to the experimental EXFAS data of C12 and C16 Co−MCM-41 (after reaction) in *R*-space by Fourier transforming both the theoretical and the experimental data using FEFF6 from the University of Washington.[26]

The near-edge spectra (XANES) of Co K edge ($E_0 = 7709$ eV) shown in Figure 5 suggests Co in the fresh Co−MCM-41 sample is in the oxidized state. However, after reaction, the XANES spectrum beyond the white line is almost identical to that of a Co foil; thus, the cobalt was mostly reduced after carbon deposition. Fitting the spectra recorded with C12 and C16 with the Co metal theoretical model, we obtained curves similar with the one depicted in the inset of Figure 5 for C12. The coordination numbers determined for C12 and C16 were 6.1 and 6.8, respectively. The differences in bond distances with respect to the theoretical references (ΔT) were 0.015 and 0.016, respectively, indicating that the fit is within acceptable limits.

The coordination number of particles smaller than 5 nm is a strong and nonlinear function of the particle diameter. This property has been widely used in EXAFS analysis to determine the size of nanoparticles.[27,28] As discussed by Frenkel,[24] although the geometry of clusters with different sizes, shapes, or lattice symmetries will generate different coordination numbers, the (111)-truncated hemispherical cubic octahedron model provides the best approximation for the relation between the average coordination number and the size of nanoparticles. We have built close packing models for cobalt (hcp) to determine the correlation depicted in Figure 6 between the average coordination number of the cobalt clusters and their diameters.

The coordination number determined from the EXAFS spectra of hexagonally closed packed Co atoms in the metallic clusters present in the C12 and C16 samples after SWNT growth for 1 h in pure CO at 750 °C are plotted on the theoretical curve showing the dependence of the cluster size on the coordination number of cobalt atoms in each cluster. These results suggest that our catalyst contains clusters with no more than 20 or 30 Co atoms, respectively, for the C12 and C16 samples. Since the EXAFS spectra shows a volume-average coordination number, the actual metallic cluster in the MCM-41 pore may
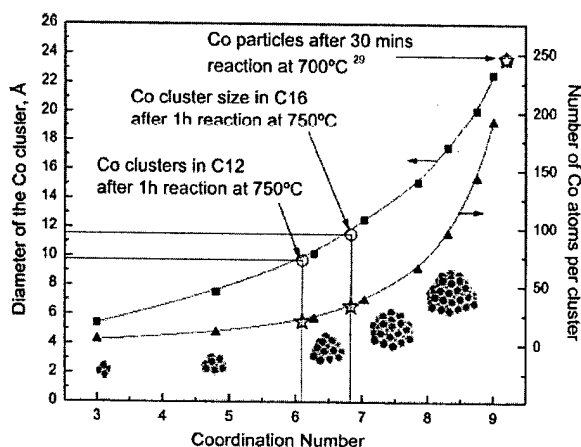
be even smaller than these because metallic particles formed outside the pore system are more mobile and can grow to larger sizes than those inside the pores. These results are consistent with TEM investigations that did not reveal the presence of metallic particles in samples after carbon deposition. It is therefore likely that the SWNT diameter is controlled by the size of the MCM-41-stabilized Co cluster, which fits in the range of the tube sizes determined from TEM images. If this is the case, we should note that the cobalt clusters produced with the MCM-41 catalyst are significantly smaller than the 9.2 coordination number observed by Resasco et al. with Co−Mo/SiO₂ catalysts, although our catalyst was exposed 30 min longer to even harsher reaction conditions (i.e., 750 vs 700 °C in the cited work).[29] Therefore, this catalytic system shows promise of improving selectivity and diameter control of SWNT for large scale applications.

The results presented here suggest that mesoporous molecular sieve templates with metals incorporated in the framework exhibit good structural stability and can be used for growth of ordered SWNT of uniform size and structure at yields and selectivity promising for large scale applications. The Co−MCM-41 catalysts become more reactive after being partially reduced in hydrogen. Reducibility of the catalytic component is strongly affected by the pore diameter of the MCM-41 material. Uniformity of SWNT diameter results most likely from the uniformity of the metallic Co clusters formed in the template. From related work, the size of these clusters appears to be controlled by the radius of curvature of the MCM-41 mesoporous molecular sieve.[30] In conclusion, this contribution shows the potential of mesoporous materials such as MCM-41 to control the properties of SWNT during synthesis.

References and Notes

(1) Bachtold, A.; Hadley, P.; Nakanishi, T.; Dekker, C. *Science* **2001**, *294*, 1317.

(2) Bockrath, M.; Liang, W.; Bozovic, D.; Hafner, J. H.; Lieber, C. M.; Tinkham, M.; Park, H. *Science* **2001**, *291*, 283.

Letters

(3) Collins, P. G.; Zettl, A.; Bando, H.; Thess, A.; Smalley, R. E. *Science* **1997**, *278*, 100.

(4) Ouyang, M.; Huang, J.-L.; Cheung, C. L.; Lieber, C. M. *Science* **2001**, *291*, 97.

(5) Tans, S. J.; Dekker, C. *Nature (London)* **2000**, *404*, 834.

(6) Collins, P. G.; Arnold, M. S.; Avouris, P. *Science* **2001**, *292*, 706.

(7) Odom, T. W.; Huang, J.-L.; Kim, P.; Lieber, C. M. *Nature (London)* **1998**, *391*, 62.

(8) Dai, H. *Acc. Chem. Res.*, in press, available on the web athttp://pubs.acs.org, Articles ASAP.

(9) Cassell, A. M.; Franklin, N. R.; Tombler, T. W.; Chan, E. M.; Han, J.; Dai, H. *J. Am. Chem. Soc.* **1999**, *121*, 7975.

(10) Cassell, A. M.; Raymakers, J. A.; Kong, J.; Dai, H. *J. Phys. Chem. B* **1999**, *103*, 6484.

(11) Resasco, D. E.; Alvarez, W. E.; Pompeo, F.; Balzano, L.; Herrera, J. E.; Kitiyanan, B.; Borgna, A. *J. Nanopart. Res.* **2002**, *4*, 131.

(12) Nikolaev, P.; Bronikowski, M. J.; Bradley, R. K.; Rohmund, F.; Colbert, D. T.; Smith, K. A.; Smalley, R. E. *Chem. Phys. Lett.* **1999**, *313*, 91.

(13) Laplaze, D.; Alvarez, L.; Guillard, T.; Badie, J. M.; Flamant, G. *Carbon* **2002**, *40*, 1621.

(14) Saito, Y.; Okuda, M.; Tomita, M.; Hayashi, T. *Chem. Phys. Lett.* **1995**, *236*, 419.

(15) Tang, Z. K.; Sun, H. D.; Wang, J.; Chen, J.; Li, G. *Bull. Mater. Sci.* **1999**, *22*, 329.

(16) Mukhopadhyay, K.; Koshio, A.; Tanaka, N.; Shinohara, H. *Jpn. J. Appl. Phys., Part 2* **1998**, *37*, L1257.

(17) Sun, H. D.; Tang, Z. K.; Chen, J.; Li, G. *Appl. Phys. A: Mater. Sci. Process.* **1999**, *69*, 381.

(18) Hayashi, T.; Kim, Y. A.; Matoba, T.; Esaka, M.; Nishimura, K.; Tsukada, T.; Endo, M.; Dresselhaus, M. S. *Nano Lett.* **2003**, *3*, 887.

(19) Beck, J. S.; Vartuli, J. C.; Roth, W. J.; Leonowicz, M. E.; Kresge, C. T.; Schmitt, K. D.; Chu, C. T. W.; Olson, D. H.; Sheppard, E. W.; McCullen, S. B.; Higgins, J. B.; Schlenker, J. L. *J. Am. Chem. Soc.* **1992**, *114*, 10834.

(20) Lim, S.; Ciuparu, D.; Pak, C.; Dobek, F.; Chen, Y.; Harding, D.; Pfefferle, L.; Haller, G. *J. Phys. Chem. B* **2003**, *107*, 11048.

(21) Herrera, J. E.; Resasco, D. E. *Chem. Phys. Lett.* **2003**, *376*, 302.

(22) Liu, X.; Pichler, T.; Knupfer, M.; Golden, M. S.; Fink, J.; Kataura, H.; Achiba, Y. *Phys. Rev. B* **2002**, *66*, 045411/1−045411/8.

(23) Chiang, I. W.; Brinson, B. E.; Smalley, R. E.; Margrave, J. L.; Hauge, R. H. *J. Phys. Chem. B* **2001**, *105*, 1157.

(24) Frenkel, A. I.; Hills, C. W.; Nuzzo, R. G. *J. Phys. Chem. B* **2001**, *105*, 12689.

(25) http://cars9.uchicago.edu/ifeffit/ (accessed August 2003).

(26) http://leonardo.phys.washington.edu/feff/ (accessed August 2003).

(27) Via, G. H.; Sinfelt, J. H.; Lytle, F. W. *J. Chem. Phys.* **1979**, *71*, 690.

(28) Greegor, R. B.; Lytle, F. W. *J. Catal.* **1980**, *63*, 476.

(29) Alvarez, W. E.; Kitiyanan, B.; Borgna, A.; Resasco, D. E. *Carbon* **2001**, *39*, 547.

(30) Lim, S.; Ciuparu, D.; Chen, Y.; Pfefferle, L.; Haller, G., manuscript in preparation, 2003.

(31) Barrett, E. P.; Joyner, L. G.; Halenda, P. P. *J. Am. Chem. Soc.* **1951**, *73*, 373.

Synthesis of uniform diameter single-wall carbon nanotubes in Co-MCM-41: effects of the catalyst prereduction and nanotube growth temperatures

Yuan Chen, Dragos Ciuparu, Sangyun Lim, Yanhui Yang, Gary L. Haller, and Lisa Pfefferle *

Department of Chemical Engineering, Yale University, New Haven, CT 06520, USA

Abstract

Catalyst pretreatment and CO disproportionation reaction conditions were observed to strongly affect the diameter uniformity of single-wall carbon nanotubes (SWNT) grown on Co-MCM-41 catalysts. The prereduction and CO disproportionation reaction temperatures were varied systematically while the carbon loading and the SWNT diameter uniformity were monitored by TGA, Raman spectroscopy, and TEM. The state of the catalyst during prereduction and the size of the cobalt clusters formed during the SWNT growth process were monitored by in situ XANES during the prereduction of the Co-MCM-41, and ex situ EXAFS of catalyst samples was performed after carbon deposition. These experiments allow development of correlations between the SWNT quality and the state of the catalyst. Control of the cobalt cluster size in the Co-MCM-41 catalyst is critical to the SWNT diameter control. The size of the cobalt cluster changes with both the prereduction and the SWNT synthesis temperatures. SWNT with a very narrow diameter distribution can be grown in Co-MCM-41 by controlling both the prereduction and the reaction temperatures.

1. Introduction

Many recent experimental studies have been dedicated to the synthesis of single wall carbon nanotubes (SWNT) due to their special electronic and mechanical properties [1–3]. SWNT growth techniques explored so far produce either a broad distribution of tube diameters [4] or SWNT of a narrow diameter distribution at a certain average diameter size imposed by the process used [5,6]. The electronic properties of the SWNT depend on their diameter and chirality. Most electronic applications require SWNT of uniform electronic properties. This requirement may be fulfilled by a synthesis process growing SWNT of uniform diameter and structure. We have recently developed a catalytic system that allows engineered diameter control of the SWNT produced within ±0.05 nm [7]. Mean diameter can be varied over the range from 0.5 to 1 nm. The cobalt catalytic component is in-

corporated into the pore wall of the MCM-41 mesoporous molecular sieve by isomorphous silicon substitution. During the SWNT growth process, cobalt is reduced and nucleates into metallic clusters that initiate the growth of the carbon nanotubes.

Our previous investigations of SWNT growth by carbon monoxide disproportionation showed SWNT yield, selectivity, and diameter uniformity to be strongly influenced by both catalyst pretreatment and the SWNT growth reaction conditions. Similar observations were previously reported by Resasco's research group working with a different catalytic system consisting of a silica-supported bimetallic cobalt–molybdenum particles [8–10]. The sensitivity of SWNT diameter distribution to growth temperature was also addressed by many other researchers [11–14]. The purpose of the present contribution is to investigate the influence of the process variables on the selectivity and the diameter uniformity of SWNT produced in a monometallic Co-MCM-41 catalyst and how these are affected by the state of the catalyst. This is a first critical step toward the optimization of

* Corresponding author.

E-mail address: lisa.pfefferle@yale.edu (L. Pfefferle).

the synthesis conditions. The prereduction and reaction temperatures were varied systematically while monitoring the carbon yield and selectivity, and the diameter uniformity of the SWNT produced. The states of the cobalt catalyst in the MCM-41 material at different stages of pretreatment and reaction were investigated by extended X-ray absorption fine structure (EXAFS), and X-ray absorption near-edge structure (XANES) was carried out in situ during the prereduction step. The ultimate goal is to understand the correlation between the state of the cobalt catalyst and the quality of the SWNT produced.

2. Experimental

2.1. Catalyst

A Co-MCM-41 catalyst with 1 wt% cobalt loading (analyzed by inductively coupled plasma (ICP) at Galbraith Laboratories, Inc.) was prepared following the procedure described in Ref. [15] using a hexadecyltrimethylammonium bromide ($C_{16}H_{33}(CH_3)_2NBr$) as templating material. All reagents used were research grade; the purity of the Cab-O-Sil fumed silica source was 99.8% with chlorine as the only identified impurity (78 ppm). Therefore, cobalt is of very high purity with respect to metals present in our catalyst. The resulting catalyst showed a high structural order with an average pore diameter (by the BJH method [16]) of 2.85 nm and 0.1 nm full width at half-maximum pore size distribution. The pore-size distribution was determined from the nitrogen adsorption-desorption isotherms measured at $-196\,°C$ with a static volumetric instrument Autosorb-1C (Quanta Chrome).

2.2. SWNT synthesis

SWNT were synthesized by CO disproportionation. For a typical batch, 200 mg of fresh Co-MCM-41 was loaded into a 10 mm internal diameter quartz reactor placed in an Omega ceramic fiber radiant heater which allows precise temperature control throughout the catalyst bed. Prior to exposure to pure CO (99.5% from Airgas, CO passes through a carbonyl trap to eliminate Fe pentacarbonyl originating from the CO container before entering the reactor) the catalyst was heated in flowing hydrogen at 1 atm at 20 °C/min from room temperature to a desired reduction temperature in the 400 to 700 °C range and reduced isothermally for 30 min. After the prereduction, the catalyst was purged with ultrahigh-purity argon (99.999% from Airgas) at the reduction temperature, and then heated from the reduction temperature to the desired reaction temperature at 20 °C/min in flowing argon. SWNT were grown for 60 min at different temperatures ranging from 650 to 900 °C under 6 atm CO pressure.

2.3. TGA

Thermal gravimetric analysis (TGA) data were collected in a Setaram Setsys 1750 instrument under oxygen flow. Samples were held at 150 °C for 1 h before initiating the temperature program. The weight change in the sample was monitored over the temperature program from 150 to 1000 °C at 10 °C/min for two successive ramps; the second was used as baseline correction for the first. A holey crucible was used to limit mass-transfer interference.

2.4. Raman spectroscopy

Raman spectra of the as-synthesized SWNT without any purification or pretreatment were recorded using an excitation wavelength of 532 nm on a LabRam instrument from Jobin Yvon Horiba equipped with an Olympus confocal microscope. The sample having the narrowest diameter distribution was compared with spectra for multiple excitation wavelength Raman previously reported to confirm these conclusions [7].

2.5. High-resolution transmission electron microscopy (HR-TEM)

HR-TEM images of the fresh Co-MCM-41 and of SWNT were collected on a Tecnai F20 200 kV microscope. The solid samples were dispersed in pure ethanol by sonication and 0.05 ml of this suspension was dropped on a copper mesh coated with an amorphous holey carbon film. The ethanol evaporated prior to the TEM analysis.

2.6. X-ray absorption spectroscopy

All X-ray absorption data were collected at beam line X23A2, National Synchrotron Light Source, Brookhaven National Laboratory. Two 30-cm-long ion chambers filled with pure N_2 were placed collinearly with the beam, in front and behind samples, to measure the incident beams I_0 and transmissive beams I_T. Two types of samples were measured: (i) ex situ samples consisting of Co-MCM-41 samples loaded with carbon after reaction, and (ii) in situ fresh Co-MCM-41 samples during hydrogen reduction. For the ex situ samples, approximately 45 mg of carbon loaded Co-MCM-41 was pressed into a rectangular wafer (ca. 1.5 × 1 cm) to form 0.5-mm-thick pellets. The thickness of pellets satisfied the condition that the absorption edge steps $\Delta \mu x$ at Co K absorption edges are smaller or equal to 1. EXAFS of ex situ samples in transmission mode were recorded from 200 eV below to 1000 eV above the Co K edge. The absorption edge of Co (7709 eV) was determined by placing a Co foil between the ion chambers and this value was used for the edge energy calibration of each sample.

In situ hydrogen reduction experiments were performed at 500 and 700 °C with the fresh Co-MCM-41 catalyst in

order to monitor the state of the catalysts during the hydrogen pretreatment. At the end of these experiments the Co cluster size was determined by EXAFS at room temperature. For the in situ experiments 50 mg of fresh Co-MCM-41 was pressed at ~5 tons into a round self-supporting wafer (1.5 cm in diameter) using a hydraulic pellet press. Wafers were placed into the stainless-steel reaction chamber, which allowed in situ gas treatment and measurement. The chamber is equipped with beryllium windows (0.5 mm thick), gas inlet, outlet, liquid nitrogen cooling system, and heating elements in the sample holder. The temperature was monitored with a K thermocouple (Omega) placed near the center of the sample holder. Pressure in the chamber was monitored by a pressure gauge (Omega). During the in situ experiment the sample was heated in flowing hydrogen from room temperature to the desired temperature at 20 °C/min and reduced isothermally for 30 min. During this period, XANES data were continuously collected from 30 eV below to 50 eV above Co K edge, averaging 5 min per scan, for in situ measurement of the state of the catalyst during reduction. After the in situ reduction, samples were quickly cooled in He flow to room temperature using a liquid nitrogen heat exchanger in the chamber. EXAFS measurements were then performed to assess the size of the Co clusters formed.

3. Results and discussion

The experiments were designed to systematically follow the influence of the pretreatment and synthesis temperatures on the overall carbon yield, and the selectivity and diameter uniformity of the SWNT produced. Cobalt states were investigated before and after reaction and in situ during reduction at two temperatures by EXAFS and XANES. We will further discuss the effect of each investigated process variable in separate sections below.

3.1. Hydrogen pretreatment

SWNT were grown for 60 min with the catalyst heated to 800 °C in argon flow or with hydrogen prereduction at different temperatures, as described in the experimental section. The Raman spectra recorded with the catalysts after SWNT growth as a function of different catalyst pretreatment conditions are given in Fig. 1. Each spectrum was obtained as the average of five spectra recorded at different locations on the same sample. All spectra showed three types of spectral features: the Raman breathing mode peaks at approximately 256 cm^{-1} characteristic for the SWNT, the D band around 1300 cm^{-1} assigned to disordered carbon species, and the peak complex between 1560 and 1600 cm^{-1} known as the G band, which is characteristic for ordered carbon species such as carbon nanotubes and graphite.

The Raman spectrum for the sample without prereduction in Fig. 1 shows several weak peaks in the RBM region

suggesting a wide diameter distribution. Most of the low-frequency, weak RBM peaks were less intense when the catalyst was prereduced at 400 °C and were almost completely removed after the catalyst was prereduced at 600 °C. As reduction temperature was further increased to 700 °C, low-frequency RBM peaks corresponding to larger tubes increased again. These results indicate that catalyst prereduction plays a crucial role for the quality of the SWNT grown with this method. The diameter uniformity of the nanotubes grown with the catalyst prereduced at 500 °C was previously demonstrated with multiple excitation wavelength Raman spectroscopy [7]. One sample was also analyzed by fluorescence spectroscopy in the laboratory of professor Weisman at Rice [17]. The florescence spectrum obtained using an excitation wavelength of 671 nm is shown in Fig. 2 along with a graphene map showing the (n, m) tubes identified in the fluorescence experiment, the average diameter observed in TEM experiments, and the largest and smallest diameters predicted by the multiple excitation wavelength Raman experiment described in [7]. Taking into account the RBM upshift by inter-tube or intrabundle interactions as discussed in [13], for the 532-nm laser used in this study, the main RBM peak at 256 cm^{-1} corresponds to tubes with diameter around 0.8–0.9 nm determined by several modified models [18–20], which is consistent with fluorescence, multiple excitation wavelength Raman, and TEM results. These results show that the diameter uniformity of the SWNT samples grown in Co-MCM-41 can be assessed using the 532-nm laser. The wider diameter distribution suggested by the Raman spectra of the SWNT grown without catalyst prereduction was confirmed by TEM. Moreover, the increase in the intensity of the RBM peak at 256 cm^{-1} as the reduction temperature increased from 400 to 600 °C is likely due to the increase of the selectivity for the SWNT identified in fluorescence.

TGA analysis was used to characterize the total carbon loading. Temperature-programmed oxidation was previously used to distinguish among different carbon species in samples [8]. While the amorphous carbon is completely oxidized at temperatures below 350 °C and graphite burns above 750 °C, the oxidation temperature of the SWNT has been observed to vary considerably for samples prepared under different conditions [21,22]. The wide range of the SWNT oxidation temperatures have been attributed to the differences in the catalytic activity of the metallic particles present in the SWNT samples [23]. The presence of tubes both inside and outside the pores of the MCM-41 catalyst may induce oxygen mass-transfer limitations and broaden the distribution of SWNT oxidation temperatures. We only used the TPO data collected in our TGA instrument as a measure of total carbon loading. The total carbon loading is given in Fig. 3 for samples synthesized at different prereduction temperatures. In agreement with the Raman spectra in Fig. 1, the carbon yield increased as the prereduction temperature increased. This behavior is consistent with metallic cobalt clusters initiating the growth of SWNT; more cobalt
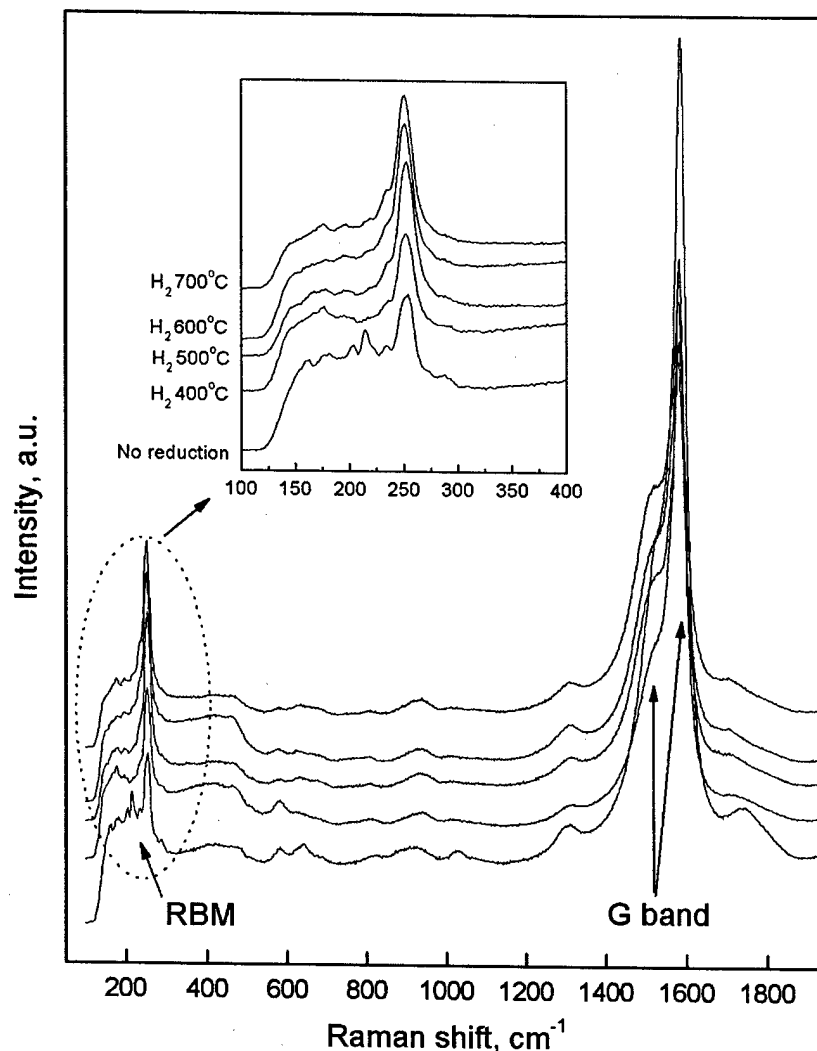
Fig. 1. Raman spectra recorded after SWNT growth with catalyst samples prereduced at different temperatures. The inset shows an enlargement of the Raman breathing mode region.

clusters are generated at higher prereduction temperatures and produce more SWNT. However, as the concentration of metallic cobalt increases in the MCM-41 pores, its nucleation in larger clusters becomes important and SWNT diameter distribution becomes wider.

Whether the metallic cobalt clusters are generated during prereduction or during subsequent exposure to CO is not clear from the experiments described above. Therefore, we employed in situ XANES spectroscopy during hydrogen reduction to investigate the effect of hydrogen pretreatment on the state of the cobalt in the Co-MCM-41. The results of this investigation were then correlated with the carbon yield discussed above.

The normalized in situ XANES data collected during the hydrogen temperature-programmed reduction of Co-MCM-41 are shown in Fig. 4. The temperature program followed the same pretreatment program used for the catalysts prior to SWNT synthesis described above. Two 30-min

plateau temperatures were used, 500 and 700 °C, to probe the effect of higher prereduction temperature on the formation of cobalt clusters. XANES spectra were calibrated to the same energy grid using a cobalt foil reference.

Spectra were normalized by FEFFIT [24]. Cobalt foil in the XANES region was also included in Fig. 4 for comparison. The spectral features associated with different cobalt states were observed clearly during the reduction process. First, a preedge peak near 7710 eV related to metallic cobalt was seen to develop as the temperature was increased. After reduction at 500 °C for 30 min, the preedge peak was similar to that observed with the fresh catalyst, suggesting incomplete reduction of Co to the metallic state, while after reduction at 700 °C a clear metallic preedge peak emerged, suggesting the presence of fully reduced metallic cobalt clusters. In addition to the preedge feature, the evolution of the white line at 7725 eV also correlates with the state of the cobalt in the catalyst. The intensity of the white line, which char-
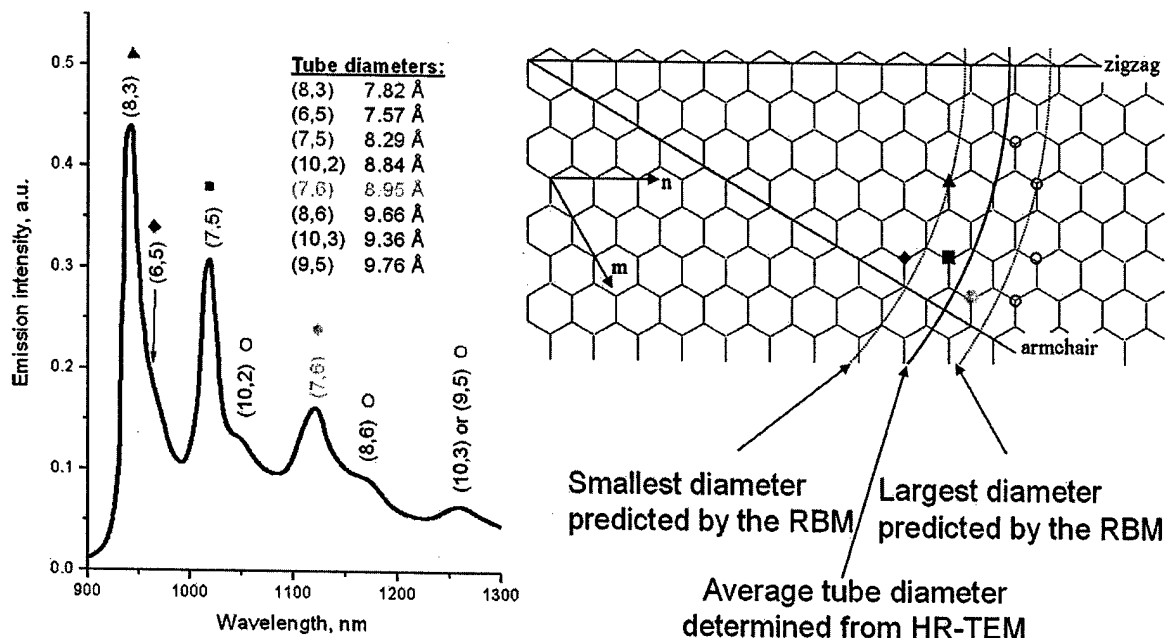
Fig. 2. Fluorescence spectra for a SWNT sample grown in Co-MCM-41 pretreated at 500 °C in H_2 and exposed for 60 min to 6 atm CO at 750 °C. The graphene map shows the tubes identified in fluorescence, the average tube diameter determined by TEM, and the diameter range determined from a multiexcitation wavelength Raman experiment reported elsewhere [7].

and the Co–O shells being 4.86 and 1.73, respectively. The analysis of the EXAFS spectra is discussed in a separate section below.

Fig. 1 shows that SWNT can be synthesized even without catalyst prereduction. However, prereduction increases the carbon yield, suggesting that hydrogen prereduction may be more effective in the extractive reduction of cobalt and/or make the cobalt ions more susceptible to further reduction in a CO environment during SWNT synthesis. This allows more cobalt clusters to form and initiate the growth of SWNT. On the other hand, complete reduction to metal leads to the formation of metallic clusters during the prereduction treatment. These clusters may sinter into larger clusters during heating to the SWNT synthesis temperature, which will grow SWNT of larger diameters with a broader diameter distribution, consistent with the presence of lower frequency RBM peaks observed in the Raman spectra of the sample prereduced at 700 °C in Fig. 1. The effect of hydrogen reduction temperature on the size and state of cobalt clusters formed on Co-MCM-41 is discussed in more detail elsewhere [25]. From these results it becomes evident that the silica matrix in the Co-MCM-41 impedes rapid cobalt reduction, leading to slow reduction of cobalt and the formation of small cobalt clusters highly selective for SWNT synthesis, consistent with our previous reports [7]. It should be noted here that the silica matrix in the Co-MCM-41 may play a similar role to that of molybdenum in the Co–Mo catalyst, which stabilizes the Co in a cobalt molybdate-like compound [9].

Without hydrogen reduction, cobalt was slowly reduced by CO even at elevated temperatures up to 900 °C, resulting
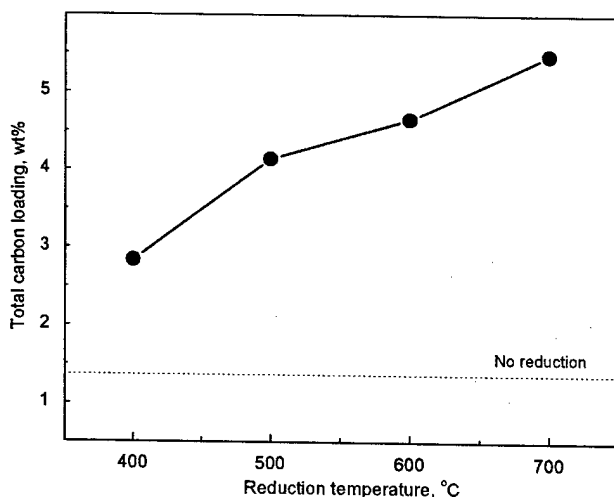

Fig. 3. The carbon yield as a function of the catalyst prereduction temperature.

acterizes cobalt ions, slightly decreased during reduction at 500 °C, suggesting the cobalt is partially reduced by hydrogen at this temperature by removing some of the oxygen from its coordination sphere and creating oxygen vacancies. During reduction for 30 min at 700 °C, however, the intensity of the white line decreased significantly and a preedge spectral feature became apparent, giving evidence for the presence of some completely reduced cobalt clusters. The analysis of the EXAFS spectra recorded at room temperature with the sample prereduced at 700 °C also confirmed the presence of coexisting oxidized and completely reduced cobalt species, with the coordination numbers for the Co–Co
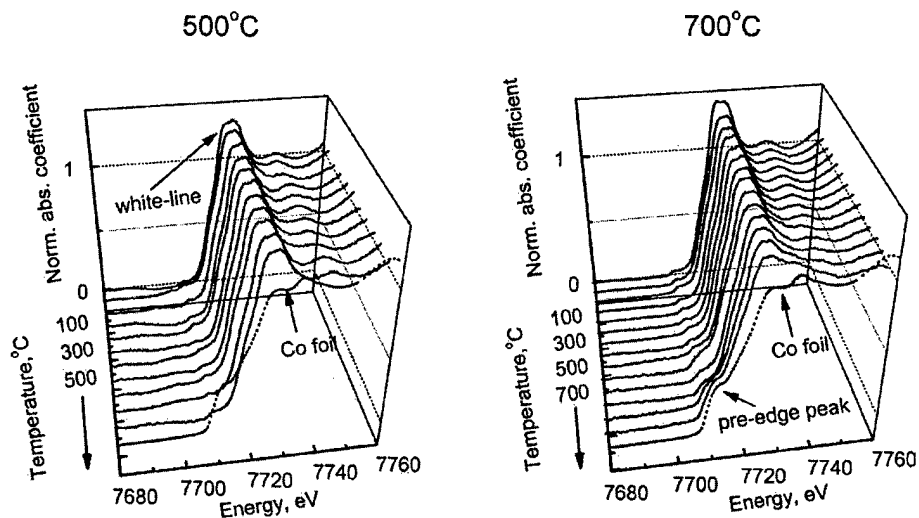
Fig. 4. Normalized XANES spectra near the Co *K* edge recorded during the temperature-programmed reduction of Co-MCM-41 in hydrogen at 500 and 700 °C.

in a weak RBM feature and low carbon loading. When the catalyst is prereduced in hydrogen at too high a temperature (e.g., 900 °C), cobalt aggregates into large particles outside the MCM-41 pores resulting in poor selectivity for SWNT. By controlling the hydrogen prereduction at specified conditions, we can produce partially reduced cobalt and obtain small Co clusters of a narrow size distribution highly selective for SWNT. We have observed that the reducibility of the cobalt is affected by pore size and template synthesis conditions; thus, the optimum prereduction conditions must be determined for each set of synthesis variables.

Prereduction at 500 °C has been used for further investigation of the influence of the SWNT synthesis temperature on the SWNT growth process performance.

3.2. SWNT synthesis temperature

First, the effect of reaction temperature on the quality of SWNT was investigated. Raman spectra recorded for SWNT samples resulting from synthesis at different reaction temperatures are given in Fig. 5. Each spectrum is the average of five spectra recorded at different locations in the same sample. The ratio between the areas of the D and G bands (I_D/I_G) was used as a purity index to qualitatively assess the amount of defective carbon in samples reacted at different temperatures. It should be noted here that this is only a relative assessment as these bands arise from both resonant and nonresonant contributions.

All of the Co-MCM-41 samples were prereduced at 500 °C and reacted for 60 min at 6 atm with pure CO at constant temperatures ranging from 650 to 900 °C. All of these catalysts produced SWNT. From the spectral features in the RBM region in Fig. 5, the Raman spectra of the sample reacted at 650 °C shows many weak peaks over a broad region indicative of a broad diameter distribution. The wide distribution of tube diameters was also evident in TEM
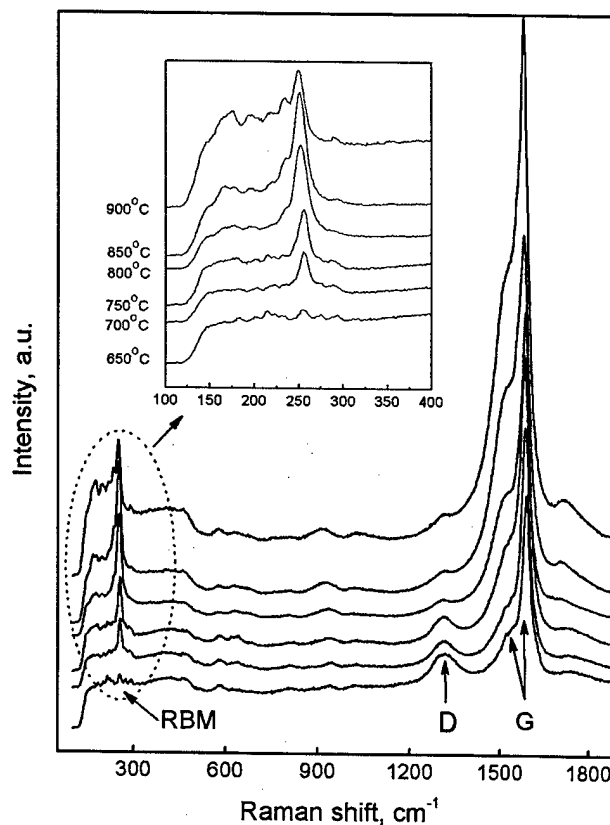
Fig. 5. Raman spectra recorded for catalyst samples after SWNT synthesis at different temperatures using a catalyst pretreated 30 min in hydrogen at 500 °C. The inset shows an enlargement of the Raman breathing mode region.

analysis. As the reaction temperature increases, the peaks in the RBM region become stronger with a narrow, single peak centered at 256 cm^{-1}. The diameter uniformity of the nanotubes suggested by the Raman spectra obtained using the
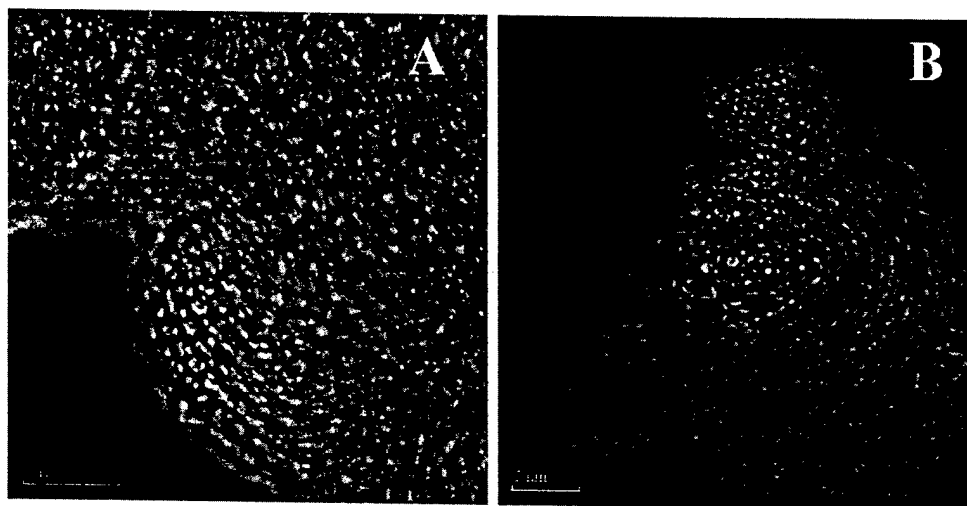
Fig. 6. TEM images showing the diameter distribution of SWNT synthesized at 750 °C (A) and 900 °C (B).

532-nm laser was confirmed by TEM experiments on several grids with specimens grown in different batches under identical experimental conditions, and by a multiple excitation wavelength Raman spectroscopy experiment on one of these samples as reported elsewhere [7]. The diameter distribution becomes broader as the reaction temperatures increases beyond 750 °C, with spectra recorded for the sample obtained after reaction at 900 °C showing several peaks, indicative of SWNT of several diameters. The wide diameter distribution resulting after reaction at 900 °C was also confirmed by TEM; an example of the images is shown in Fig. 6. Note that the SWNT synthesized at 750 °C (micrograph A in Fig. 6) are in a close-packed hexagonal arrangement, characteristic of tubular structures having uniform diameters [26]. By contrast, the tubes imaged in the sample grown at 900 °C (image B in Fig. 6) give evidence of tubes of several different diameters. Observation of several peaks in the RBM region for the SWNT grown with the Co-MCM-41 catalyst is direct evidence that the Raman spectroscopy using the 532-nm laser line is sensitive to the broadening of the diameter distribution of the SWNT in our samples, and can be used as a relative measure of diameter uniformity.

The total carbon loading is shown in Fig. 7 for the samples synthesized at different temperatures, along with the purity index defined above. As the SWNT synthesis temperature increased from 650 to 900 °C, the purity index I_D/I_G decreased from 0.29 to less than 0.01, suggesting the amount of ordered carbon (SWNT or graphite) increased with increasing temperature. The total carbon loading determined by TGA increased from 2.1 to 4.1% when the reaction temperature increased from 650 to 800 °C, then decreased to 2.1% as reaction temperature increased to 900 °C, which indicates a maximum in the carbon yield at approximately 800 °C. Although the decrease of the carbon yield at temperatures higher than 800 °C may convolute the effect of the thermodynamic equilibrium of the CO disproportionation reaction which is disfavored by higher temperatures, these
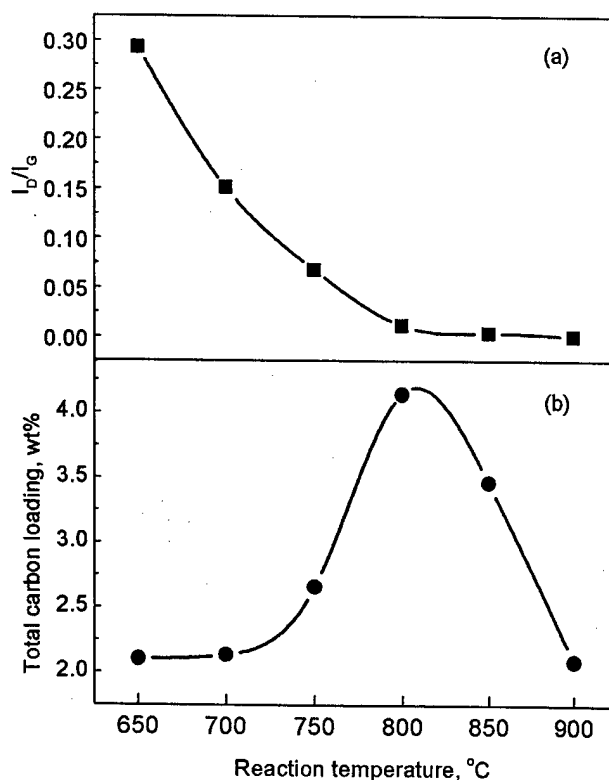
Fig. 7. Variation of the purity I_D/I_G index (a) and of the total carbon yield (b) as functions of the SWNT synthesis temperature.

results suggest that at higher temperatures the Co-MCM-41 is less active for carbon deposition. The temperature corresponding to the maximum carbon yield was observed to increase as the pore size of the MCM-41 template decreases, and this effect is most likely related to the reducibility of the metal in the MCM-41 framework which was observed to decrease as the pore size decreases [25].

A broader distribution of SWNT diameter, as determined by Raman spectroscopy using the 532-nm laser excita-

Fig. 8. Transmission electron micrograph showing a large cobalt particle formed during reaction at 900 °C and covered with a continuous layer of carbon.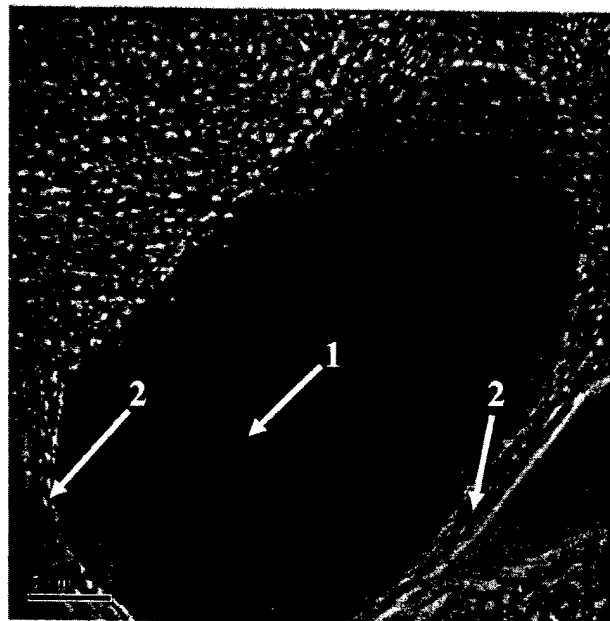 Arrows indicate the lattice spacing of the Co particle (1) and the continuous carbon layer covering the Co particle (2).

tion wavelength, was previously reported by Resasco and co-workers for SWNT samples grown at higher temperatures [27]. However, when compared to the Co–Mo catalyst, the Co-MCM-41 catalyst behaves differently with respect to the carbon yield observed in the same temperature range. The carbon yield obtained with the Co–Mo catalyst decreases as the SWNT growth temperature increases from 600 to 800 °C [28]. The authors explained the decrease of the carbon yield by an increased rate of catalyst deactivation at higher temperatures. The carbon yield observed with the Co-MCM-41 catalyst increased when the temperature increased from 650 to 800 °C and only decreased as the temperature further increased above 800 °C.

Along the lines of the proposed mechanism in which the initially atomically dispersed cobalt ions are partially reduced in the pretreatment stage, and then further reduced to metallic cobalt clusters during SWNT growth, we explain both the low carbon yield and the poor selectivity of the sample reacted at 650 °C by the low number of Co clusters available for SWNT growth. As the reaction temperature increases, the rate of cobalt reduction increases and more cobalt clusters nucleate to reach the optimal size for SWNT growth. This is consistent with the carbon yield increasing as the reaction temperature increases between 650 and 800 °C. However, as the temperature increases, so does the mobility of Co clusters in the MCM-41 pores and the rate of sintering, in agreement with the hypothesis proposed by the Resasco group [27,28]. On the other hand, as a cobalt cluster initiates the growth of a SWNT, it becomes covered with carbon and cannot further sinter into larger metallic clusters. At a certain temperature the rate of cobalt cluster formation surpasses the

rate of initiation of the SWNT growth, so that, before the cobalt cluster initiates the growth of a SWNT, it migrates and combines with other Co clusters to give larger metallic clusters, mostly outside the MCM-41 pores. As the size of the cobalt clusters increases, their selectivity for SWNT decreases; they form a surface graphite layer which makes them inactive for CO disproportionation. This is consistent with lower carbon yield at synthesis temperatures higher than 800 °C and more graphite on the surface as the synthesis temperature increases beyond 800 °C. Indeed, the TEM micrograph in Fig. 8 recorded with the sample reacted at 900 °C gives clear evidence of the presence of large cobalt particles covered with graphite. These particles cannot be dissolved in HCl from the SWNT samples removed from the template, likely because the compact graphite layer impedes the access of the acid to the metallic particle. When a prepurified SWNT sample was exposed to microwave radiation, partial oxidation of the covering graphite layer resulted allowing more cobalt to dissolve in a subsequent HCl treatment.

If the proposed mechanism is valid, a slow cobalt reduction process during reaction produces smaller cobalt clusters at lower temperatures, highly selective for SWNT synthesis, and the size of the cobalt clusters should vary with reaction temperature. Such differences in the cobalt clusters size were investigated for samples reacted at different temperatures by EXAFS. The X-ray absorption spectra were analyzed following the procedure described elsewhere [29,30] in four steps. (1) The edge energies were referenced to the edge energy measured with the cobalt foil; background removal and edge-step normalization were performed using the FEFFIT [24]. Full range spectra are shown in Fig. 9. (2) The white line features and the preedge peak details near the Co K edge (7709 eV) were investigated as depicted in Fig. 10. (3) FEFFIT was subsequently used to fit the EXAFS function using paths for metallic and oxidized cobalt species (Co, Co_3O_4) as generated by the FEFF6 program [31]. The fitting was limited to a k range of 2.2–10.0 Å^{-1}, k weighted, with modified Hanning windows, $dk = 1.0$ Å^{-1}, and an R range from 1.2 to 2.7 Å. The parametric sensitivity analysis performed for different windows, R ranges, and dk values showed that the fitting results were not significantly affected, while the best fittings were obtained with the values given above. The fitting results are plotted in Fig. 11 and the resulting Co–Co and Co–O first shell coordination numbers are given in Table 1 and plotted against the reaction temperature in Fig. 12. (4) The Co–Co first shell coordination numbers were used to estimate the average cobalt clusters size in the Co-MCM-41 catalysts after reaction at different temperatures.

Fig. 9a shows the reaction temperature-dependent normalized absorption coefficient as a function of the scanning energy. Several changes in the EXAFS were observed in this data. The fresh Co-MCM-41 has a strong white line centered at 7725 eV, while the cobalt foil has only a very weak white line. The spectra recorded for samples reacted at dif-
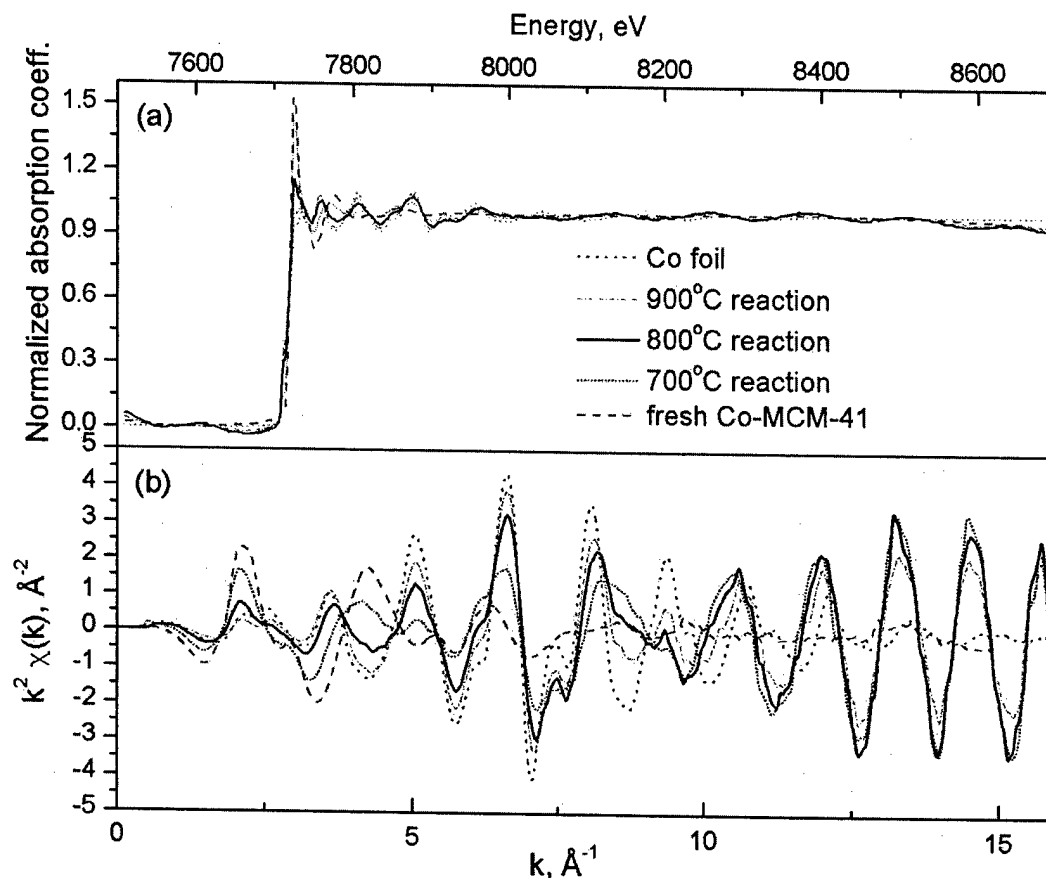
Fig. 9. EXAFS data for Co-MCM-41 catalysts after reaction at different temperatures. The fresh Co-MCM-41 and the cobalt foil are given as references. (a) Normalized EXAFS data calibrated relative to the cobalt foil. (b) The k^2-weighted EXAFS data in the k space.

Table 1

Structure parameters of Co-MCM-41 catalysts from EXAFS fitting

Reaction temperature (°C)	Co–O first shell			Co–Co first shell		
	N_{Co-O}[a]	dR[b] (Å)	σ^{2c}	N_{Co-Co}[d]	dR[b] (Å)	σ^{2c}
700	1.98 ± 0.85	0.14 ± 0.02	0.88	3.46 ± 1.51	−0.05 ± 0.02	1.16
750	1.31 ± 0.60	0.14 ± 0.02	0.89	5.01 ± 1.26	−0.03 ± 0.01	0.83
800	0.73 ± 0.27	0.13 ± 0.01	1.48	7.10 ± 0.87	−0.02 ± 0.01	0.80
850	0.24 ± 0.20	0.12 ± 0.02	1.94	8.62 ± 0.85	−0.02 ± 0.01	0.72
900	0.17 ± 0.20	0.12 ± 0.03	2.15	8.97 ± 1.05	−0.02 ± 0.01	0.71

[a] N_{Co-O} average first shell coordination of cobalt–oxygen.

[b] dR deviation from the effective half-path-length R (R is the interatomic distance for single scattering paths).

[c] $\sigma^2 (\times 10^{-2}\ Å^2)$ mean-square deviation in R.

[d] N_{Co-Co} average first shell coordination of cobalt.

ferent temperature were located between the spectrum of the fresh Co-MCM-41 and that of the cobalt foil. The effect of the reaction temperature is also illustrated by the changes in EXAFS amplitude seen across the higher energy range. Fig. 9b shows the same EXFAS data shown in Fig. 9a in a k^2-weighted k space (k is the photoelectron wavenumber). The effect of the reaction temperature is even more clearly presented in k space. The peaks for the cobalt foil (cobalt in a metallic state) and for the fresh Co-MCM-41 (Co in the oxidized state) exhibit different positions and magnitudes in

k space. The shifts in the peak position and magnitude are related to both different cobalt states and cluster sizes. The spectrum recorded for the Co-MCM-41 reacted at 900 °C is close to that of the cobalt foil with respect to both position and magnitude, suggesting that cobalt was almost completely reduced after reaction at 900 °C, while the spectra of the Co-MCM-41 reacted at 700 °C is very close to that of the fresh Co-MCM-41, showing that a significant fraction of cobalt is still in the oxidized state after reaction at this lower temperature. The spectrum of the sample reacted at 800 °C
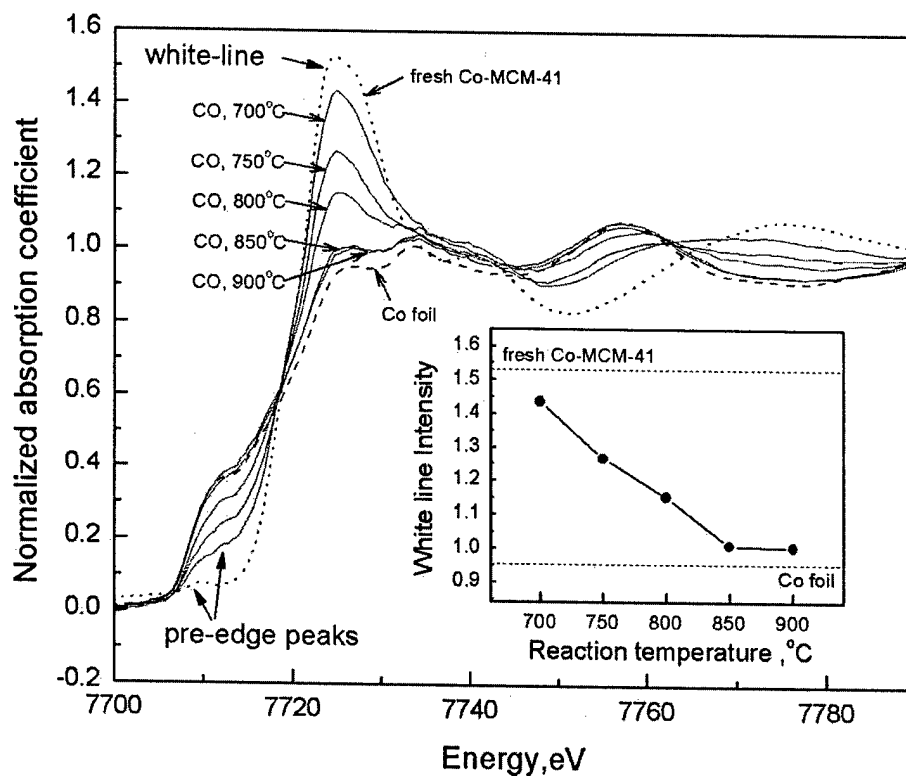
Fig. 10. Normalized EXFAS spectra near Co K edge recorded for Co-MCM-41 loaded with carbon after reaction at different temperatures. Spectra for the fresh Co-MCM-41 and cobalt foil are given as references. The inset shows the correlation between the intensity of the white line and the SWNT synthesis temperature.

Fig. 11. EXAFS spectra in R space for Co-MCM-41 catalysts after reaction at different temperatures along with the fitting of the spectra with theoretical models.

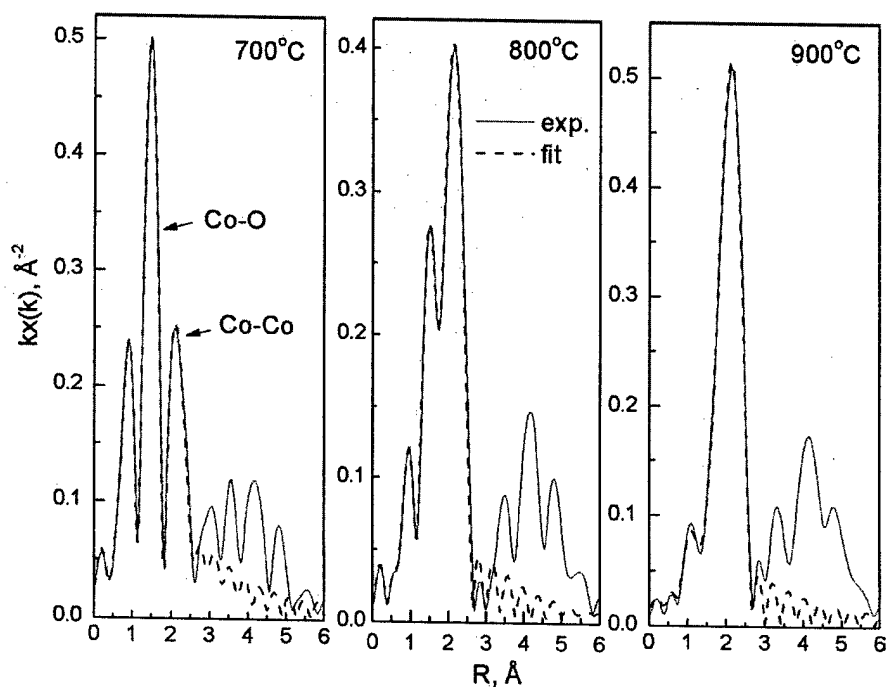showed, as expected, an intermediate state between those of the samples reacted at 700 and 900 °C.

Fig. 10 illustrates the EXAFS spectra near the Co *K* edge (7709 eV) obtained with Co-MCM-41 samples after reaction at different temperatures. The spectrum recorded with the Co foil reference is also given for comparison. The preedge peaks indicate that cobalt in the fresh Co-MCM-41 is a mixture of Co^{2+} and Co^{3+} in tetrahedral and distorted tetrahedral coordinations with a pseudo-octahedral environment, most likely due to hydration, as discussed elsewhere [15]. The cobalt foil has a strong preedge peak assigned to metallic cobalt. The increase of the preedge feature for the Co-MCM-41 catalyst as the reaction temperature increased constitutes direct evidence for the increase in the cobalt reduction to metallic cobalt as SWNT are synthesized at higher temperatures.

The white line feature is assigned to unfilled d states at the Fermi level. For metals with completely filled d states (e.g., copper) the absorption edge is of the form of a simple step function; the intensity of the white line increases with the number of unfilled d states [32]. The changes in the white-line intensity have been used to characterize the d-hole populations in alloys [33]. For metallic cobalt the presence of 7 electrons in d orbitals gives a weak white line, while for the oxidized cobalt with fewer electrons in d states the white line is stronger. Partial reduction of cobalt in the Co-MCM-41 catalyst during SWNT synthesis was evident from the decrease in the intensity of the white line between the fresh Co-MCM-41 and the completely reduced Co foil observed in Fig. 10. The inset in Fig. 10 shows the variation of the intensity of the white line with the reaction temperature. The spectra of the fresh Co-MCM-41 and of the Co foil have white-line intensities of 1.53 and 0.95, respectively. As the reaction temperature increases from 700 to 900 °C, the intensity of the white line decreased from 1.44 to 1.00, clearly showing different degrees of cobalt reduction for reaction at different temperatures. Higher reaction temperatures cause more cobalt reduction. After reaction at low temperatures (lower than 750 °C), a large fraction of the cobalt remained oxidized, consistent with the lower carbon yield observed in Fig. 7. As the reaction temperature increased above 800 °C, the cobalt was almost quantitatively reduced.

Because in Co-MCM-41 there is a mixture of Co^{2+} and Co^{3+}, there are two different Co–O bonds: a short Co–O bond in Co_2O_3 and a longer Co–O bond in CoO. FEFF6 generated two main Co–O paths from the crystalline structure of Co_3O_4 [34] related to the two different Co–O bond lengths. Using each of these two paths, and both of them simultaneously, to fit the fresh Co-MCM-41 we observed that the path corresponding to the short Co–O bond gave an acceptable fitting for a coordination number of 4, and adding the second path did not significantly improve the fitting. Therefore, we used only two scattering paths to fit the data: the first Co–O path in Co_3O_4 and the first Co–Co path in Co metal. The energy shifts for each shell were observed to have small changes for samples reacted at different temper-
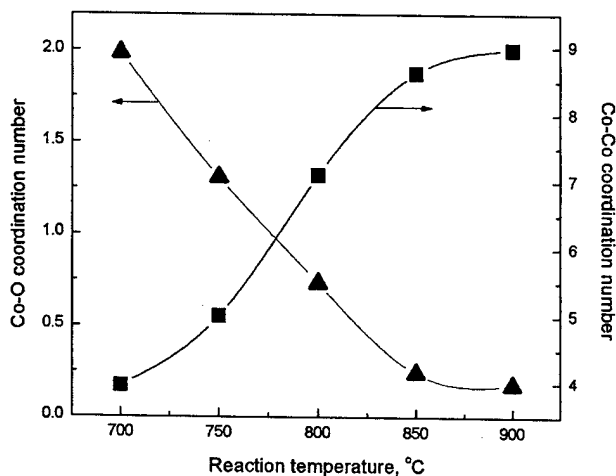

Fig. 12. Coordination numbers of the first Co–O and Co–Co shells as a function of reaction temperature, as fitted from the EXFAS spectra.

atures, and thus were subsequently set constant at 5.57 eV for the Co–Co shells and 2.41 eV for the Co–O shells. The passive electron reduction factor (S_0^2) was set to 0.9, as recommended by Rehr and co-workers [35]. Consequently, the fitting was performed having only the coordination numbers and the radial distance of each shell as variables.

The k-weighted EXAFS spectra recorded with the samples after reaction at 700, 800, and 900 °C are shown in Fig. 11 along with the fitting results obtained using the two theoretically calculated paths. There is good overall agreement between the fitting and the experimental data for all samples. The peaks related to the Co–O bond decreased when the reaction temperature increased, most likely because of the higher degree of reduction in the samples reacted at higher temperatures. In contrast, the intensity of the Co–Co peak increased for samples reacted at higher temperatures consistent with a higher degree of Co reduction to metallic clusters. The structural parameters resulting from the fitting using the two paths and their estimated errors are presented in Table 1, and the decrease of Co–O coordination numbers and the increase of Co–Co coordination number with the increase of reaction temperature are illustrated graphically in Fig. 12.

As previously reported, EXAFS has been widely used to determine the size of nanoparticles because of the strong and nonlinear correlation between the particle diameter and the coordination number of atoms in small clusters [7]. We also used the Co–Co first shell coordination number fitted from EXAFS spectra recorded with catalyst samples after reaction at different temperatures to determine the approximate size of the cobalt cluster formed during SWNT growth in an attempt to establish a correlation with the diameter distribution of SWNT produced. We have built a (111)-truncated hemispherical cuboctahedron model to correlate the cobalt cluster diameter with the average first shell coordination number. The variation in the Co coordination number with the cluster size is given by the curve in Fig. 13. Average
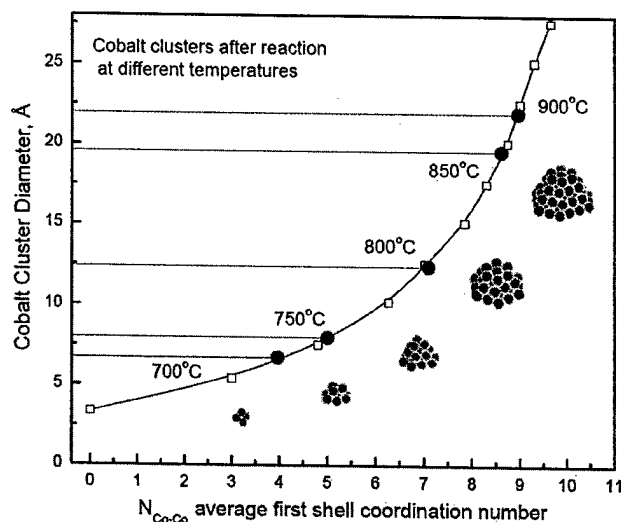
Fig. 13. Variation of the Co–Co coordination number with the first shell with the cluster diameter determined for the cobalt (111)-truncated hemispherical cubic octahedron model. The round gray symbols show the coordination numbers determined from the analysis of the EXAFS spectra.

coordination numbers for cobalt in Co-MCM-41 after reaction are plotted on the theoretical curve along with approximate cluster sizes. The results show the expected increase in cluster size as a function of reaction temperature with a jump between 800 and 850 °C. Correlating these results with the Raman spectra in Fig. 5 provides a direct confirmation of our hypothesis that small cobalt clusters form SWNT of very narrow diameter distribution. However, it is important to note here that, as discussed by Frenkel et al. [30], the geometry of clusters with different sizes, shapes, or lattice symmetries generate different coordination numbers. Although the (111)-truncated hemispherical cuboctahedron model provides a good approximation, the cobalt clusters may have different shapes. In fact, the shapes are likely influenced by ultrasmall particles interacting with the pore wall of the MCM-41 material. These cluster diameters determined by EXAFS only give an average approximation for the cluster sizes. Also, as discussed in [7], the metallic particles formed outside the pore system are more likely to sinter and grow into larger particles than those inside the pores. These larger cobalt particles are likely selective for the growth of graphite and amorphous carbon, depending on the reaction conditions (i.e., higher temperatures produce more graphite, while lower reaction temperature form more amorphous carbon). The EXAFS spectra reported here provide a volume average coordination number which includes larger particles outside the pores. The actual metallic clusters in the Co-MCM-41 pore may be smaller than the average estimated. The EXAFS data correlate well with the Raman characterization of the SWNT produced and confirms that small Co clusters are required for production of SWNT with good selectivity and a narrow diameter distribution.

4. Conclusions

A systematic investigation of the influence of the catalyst pretreatment and nanotube synthesis temperature on the characteristics of the SWNT diameter distribution produced in Co-MCM-41 was carried out. The results obtained by TGA, Raman spectroscopy, and HR-TEM, combined with EXAFS and XANES spectroscopy suggest that the diameter distribution and quality of SWNT in Co-MCM-41 can be engineered by controlling cobalt cluster size through the hydrogen prereduction and the reaction temperature. Cobalt in Co-MCM-41 becomes more active for SWNT growth after partial reduction by hydrogen. The catalysts that are excessively reduced prior to exposure to CO form SWNT with a wider diameter distribution. A narrow distribution of SWNT diameter can be achieved at an optimized prereduction and reaction temperature, i.e., prereduction at 500–600 °C and reaction at 750–800 °C. The control of cobalt cluster sizes in Co-MCM-41 is the key to SWNT diameter control. The Co^{2+} isomorphously substituted for silica in the MCM-41 framework is stable under severe reaction conditions, allowing slow reduction and nucleation of metallic clusters for production of large carbon yields at high reaction temperatures with high selectivity for SWNT and narrow tube diameter distribution.

References

[1] H.J. Dai, Acc. Chem. Res. 35 (2002) 1035.
[2] A. Huczko, Appl. Phys. A 74 (2002) 617.
[3] S.B. Sinnott, R. Andrews, Crit. Rev. Solid State Mater. Sci. 26 (2001) 145.
[4] R.R. Bacsa, C. Laurent, A. Peigney, W.S. Bacsa, T. Vaugien, A. Rousset, Chem. Phys. Lett. 323 (2000) 566.
[5] G.D. Li, Z.K. Tang, N. Wang, J.S. Chen, Carbon 40 (2002) 917.
[6] S.M. Bachilo, L. Balzano, J.E. Herrera, F. Pompeo, D.E. Resasco, R.B. Weisman, J. Am. Chem. Soc. 125 (2003) 11186.
[7] D. Ciuparu, Y. Chen, S. Lim, G.L. Haller, L. Pfefferle, J. Phys. Chem. B 108 (2004) 503.
[8] W.E. Alvarez, F. Pompeo, J.E. Herrera, L. Balzano, D.E. Resasco, Chem. Mater. 14 (2002) 1853.
[9] J.E. Herrera, L. Balzano, A. Borgna, W.E. Alvarez, D.E. Resasco, J. Catal. 204 (2001) 129.
[10] B. Kitiyanan, W.E. Alvarez, J.H. Harwell, D.E. Resasco, Chem. Phys. Lett. 317 (2000) 497.
[11] M. Sugano, A. Kasuya, K. Tohji, Y. Saito, Y. Nishina, Chem. Phys. Lett. 292 (1998) 575.
[12] H. Kuzmany, B. Burger, M. Hulman, J. Kurti, A.G. Rinzler, R.E. Smalley, EuroPhys. Lett. 44 (1998) 518.
[13] M.S. Dresselhaus, P.C. Eklund, Adv. Phys. 49 (2000) 705.

[14] C. Journet, W.K. Maser, P. Bernier, A. Loiseau, M.L. delaChapelle, S. Lefrant, P. Deniard, R. Lee, J.E. Fischer, Nature 388 (1997) 756.

[15] S. Lim, D. Ciuparu, C. Pak, F. Dobek, Y. Chen, D. Harding, L. Pfefferle, G. Haller, J. Phys. Chem. B 107 (2003) 11048.

[16] E.P. Barrett, L.G. Joyner, P.P. Halenda, J. Am. Chem. Soc. 73 (1951) 373.

[17] M.J. O'Connell, S.M. Bachilo, C.B. Huffman, V.C. Moore, M.S. Strano, E.H. Haroz, K.L. Rialon, P.J. Boul, W.H. Noon, C. Kittrell, J.P. Ma, R.H. Hauge, R.B. Weisman, R.E. Smalley, Science 297 (2002) 593.

[18] L. Alvarez, A. Righi, T. Guillard, S. Rols, E. Anglaret, D. Laplaze, J.L. Sauvajol, Chem. Phys. Lett. 316 (2000) 186.

[19] U.D. Venkateswaran, A.M. Rao, E. Richter, M. Menon, A. Rinzler, R.E. Smalley, P.C. Eklund, Phys. Rev. B 59 (1999) 10928.

[20] D. Kahn, J.P. Lu, Phys. Rev. B 60 (1999) 6535.

[21] A.G. Rinzler, J. Liu, H. Dai, P. Nikolaev, C.B. Huffman, F.J. Rodriguez-Macias, P.J. Boul, A.H. Lu, D. Heymann, D.T. Colbert, R.S. Lee, J.E. Fischer, A.M. Rao, P.C. Eklund, R.E. Smalley, Appl. Phys. A 67 (1998) 29.

[22] Z.J. Shi, Y.F. Lian, F.H. Liao, X.H. Zhou, Z.N. Gu, Y.G. Zhang, S. Iijima, Solid State Commun. 112 (1999) 35.

[23] J.E. Herrera, D.E. Resasco, Chem. Phys. Lett. 376 (2003) 302.

[24] E.A. Stern, M. Newville, B. Ravel, Y. Yacoby, D. Haskel, Phys. B 209 (1995) 117.

[25] S. Lim, D. Ciuparu, Y. Chen, Y. Yang, L. Pfefferle, G.L. Haller, J. Phys. Chem. B (2004), in press.

[26] W. Shi, J.K. Johnson, Phys. Rev. Lett. 91 (2003) art. no. 015504.

[27] D.E. Resasco, W.E. Alvarez, F. Pompeo, L. Balzano, J.E. Herrera, B. Kitiyanan, A. Borgna, J. Nanoparticle Res. 4 (2002) 131.

[28] W.E. Alvarez, B. Kitiyanan, A. Borgna, D.E. Resasco, Carbon 39 (2001) 547.

[29] M.K. Neylon, C.L. Marshall, A.J. Kropf, J. Am. Chem. Soc. 124 (2002) 5457.

[30] A.I. Frenkel, C.W. Hills, R.G. Nuzzo, J. Phys. Chem. B 105 (2001) 12689.

[31] A.L. Ankudinov, B. Ravel, J.J. Rehr, S.D. Conradson, Phys. Rev. B 58 (1998) 7565.

[32] J.M. Thomas, W.J. Thomos, Principels and Practice of Heterogeneous Catalysis, VCH, New York, 1997.

[33] I. Coulthard, T.K. Sham, Phys. Rev. Lett. 77 (1996) 4824.

[34] R.W.G. Wychoff, Crystal Structures, vol. 3, second ed., Interscience, New York, 1963, p. 78.

[35] L. Campbell, L. Hedin, J.J. Rehr, W. Bardyszewski, Phys. Rev. B 65 (2002).

ELSEVIER

Synthesis of uniform diameter single wall carbon nanotubes in Co-MCM-41: effects of CO pressure and reaction time

Yuan Chen, Dragos Ciuparu, Sangyun Lim, Yanhui Yang, Gary L. Haller, Lisa Pfefferle *

Department of Chemical Engineering, Yale University, New Haven, CT 06520, USA

Abstract

The influence of the CO pressure and of the duration of catalyst exposure to CO was systematically investigated with respect to the carbon yield, selectivity, and diameter uniformity of single wall carbon nanotubes (SWNT) produced by CO disproportionation over Co-MCM-41 catalysts. The SWNT were characterized by Raman and near infrared (NIR) spectroscopy, while the state of the catalyst and the size of the metallic cobalt clusters were investigated by X-ray absorption spectroscopy (XAS). The experimental results suggest that both the selectivity to SWNT and the uniformity of their diameters are controlled by the relative rates of the following competing processes: cobalt reduction, nucleation of cobalt into clusters, and SWNT growth. It was found that reaction at low CO pressures leads to a wider distribution of diameters and lower SWNT selectivity. The duration of catalyst exposure to CO was found to strongly affect the SWNT selectivity at the early stages of SWNT growth, while it has a minor effect on the SWNT diameter uniformity.
© 2004 Elsevier Inc. All rights reserved.

Keywords: Single wall carbon nanotubes; Cobalt clusters; CO pressure; Reaction time

1. Introduction

Incorporation of single wall carbon nanotubes (SWNT) in electronic devices requires materials of uniform electronic properties. Because the electronic properties of the carbon nanotubes depend on their n and m vectors [1], thus on diameter and chirality, SWNT synthesis methods producing a narrow diameter distribution are highly desirable. We have shown that SWNT can be produced by CO disproportionation on a cobalt catalyst incorporated by isomorphous substitution of silicon in the pore walls of the MCM-41 mesoporous molecular sieve [2]. We have also shown that the diameter of SWNT produced with this catalytic system can be engineered by controlling the size of the metallic Co clusters that initiate the growth of the SWNT [3].

Several studies have been dedicated to the investigation of the effects of the SWNT synthesis process variables on the overall process performance [4–21]. Many of these studies have reported various effects of the reaction time and pressure on the purity, diameter control, and uniformity of the

SWNT produced. The differences in the observed effects are mainly due to the use of different processes [4–6], carbon sources [7–10], or catalytic systems [11–15] for the growth of SWNT. For the Co–Mo catalytic system, which is somewhat similar to our Co-MCM-41 catalyst, the carbon yield and SWNT selectivity increased when the catalyst was exposed to CO for longer than 2 h [15,16].

In our prior investigations we observed that the diameter uniformity of the SWNT produced using this synthesis technique is strongly influenced by the catalyst pretreatment conditions (i.e., prereduction temperature) and CO disproportionation conditions such as the reaction temperature, pressure, and duration. In a recent paper we reported the effects of the template prereduction temperature and CO disproportionation temperature on the diameter uniformity of the nanotubes produced [22]. We have shown that the diameter distribution and quality of SWNT grown in Co-MCM-41 can be engineered by controlling the hydrogen prereduction and reaction temperatures, and that the cobalt incorporated in the MCM-41 matrix becomes more selective to SWNT after partial reduction by hydrogen, while the catalysts that were excessively reduced prior to exposure to CO became less selective for SWNT, producing more amorphous car-

---

* Corresponding author.

E-mail address: dragos.ciuparu@yale.edu (L. Pfefferle).

bon and/or graphite. We have also demonstrated that uniform SWNT diameter (± 0.05 nm) can be achieved by using optimized prereduction and reaction temperatures, and that control of cobalt cluster sizes in Co-MCM-41 is the key to SWNT diameter control [22].

In the present contribution we report our investigations on the effects of the growth time and CO pressure during SWNT growth on the diameter uniformity and the quality of the SWNTs produced as qualitatively determined from Raman and near-infrared spectroscopy.

2. Experimental

The Co-MCM-41 catalyst with a 1.00 wt% Co loading and a pore diameter of 2.85 ± 0.1 nm was synthesized using the $C_{16}H_{33}(CH_3)_2NBr$ alkyl template following the procedure described elsewhere [2]. The purity of the silica source affected the reducibility of the cobalt ions in the framework. The catalysts employed in these studies were synthesized using the highly pure Cab-O-Sil silica. Approximately 200 mg of fresh catalysts was loaded into a quartz reactor placed in an electric furnace with very good temperature control for the entire length of the catalyst bed. Prior to exposure to pure CO the catalyst was heated in flowing hydrogen (1 atm) at $20\,°C$/min from room temperature to $500\,°C$ and reduced isothermally for 30 min. After this prereduction treatment, the catalyst was purged with ultrahigh-purity argon at $500\,°C$ and then heated to $800\,°C$ at $20\,°C$/min in flowing argon (4 atm). SWNT were grown for 5–120 min at $800\,°C$ under different CO partial pressures ranging from 2 to 6 atm.

The carbon yields were determined from the thermogravimetrical analysis performed in a Setaram SetSys 1750 instrument using a holey crucible that prevents mass-transfer limitations. The weight of the sample was monitored during two consecutive temperature programs for each sample, the second being used as a baseline for the first.

Raman spectra were recorded with as-synthesized SWNT samples, without any purification or pretreatment, on a LabRam instrument from Jobin Yvon Horiba equipped with an Olympus confocal microscope (at 532 nm excitation wavelength). Integration times were around 15 s for each spectrum, and each spectrum was the average of five scans. Multiexcitation wavelength Raman spectra were collected at the University of Connecticut with a Renishaw Ramanscope in the backscattering configuration under the same experimental conditions with different integration times. The spectra were obtained using four different lasers with wavelengths of 488 nm (2.54 eV), 514.5 nm (2.41 eV), 633 nm (1.96 eV), and 785 nm (1.58 eV).

Absorption spectra in the near-infrared (NIR) region were recorded for SWNT samples dispersed by sonication in N,N-dimethylformamide (DMF) using a Nicolet NEXUS Fourier transform infrared spectrometer equipped with a quartz beam splitter.

Diameter distribution was also probed by high-resolution transmission electron microscopy (HR-TEM). Micrographs were obtained on a Tecnai F20 (200 kV) microscope from Phillips.

The state of the cobalt catalyst and assessment of the cobalt cluster sizes were determined from the X-ray absorption spectra collected at the beam line X23A2 of the National Synchrotron Light Source at Brookhaven National Laboratory. Analysis of the X-ray absorption spectra was performed following the procedures described in detail in our previous work [22].

3. Results and discussion

Two series of experiments were designed to investigate the influence of the CO pressure and the duration of nanotube growth on the overall carbon yield, and the selectivity and diameter uniformity of the SWNT produced. Catalyst samples removed from the reactor after SWNT growth under different conditions, without any purification or pretreatment, were studied by extended X-ray absorption fine structure (EXAFS) spectroscopy to determine the cobalt oxidation state and the size of the cobalt clusters in the catalysts after reaction. These results were further correlated with the carbon yield and SWNT selectivity determined from the complementary thermo-gravimetrical analysis, and Raman and NIR spectroscopy in order to understand the mechanism by which the CO pressure and growth duration influence the SWNT synthesis performance. The effect of each investigated process variable is discussed in separate sections below.

3.1. Carbon monoxide pressure

For the first series of experiments catalyst samples pretreated in pure hydrogen at $500\,°C$ for 30 min were exposed to pure CO for 60 min at $800\,°C$ under different CO pressures ranging from 2 to 6 atm.

The Raman spectra recorded with the catalyst after SWNT growth under different CO pressures are given in Fig. 1. Each spectrum is the average of five spectra recorded at different locations in the same sample. Three types of spectral features are observed in each spectrum: the peaks in the Raman breathing mode (RBM) region ($\bar{\nu} \leqslant 350$ cm^{-1}), characteristic for SWNT, provide information about tube diameters [23,24] and chirality [25,26]; the D band at approximately 1300 cm^{-1} is assigned to disordered and/or defective carbon species; and the peak complex around 1600 cm^{-1}, known as the G band, is characteristic of ordered carbon species such as carbon nanotubes and graphite.

The Raman spectrum of the SWNT grown at 2 atm shows several peaks in the RBM region, suggesting that the diameters of the nanotubes produced at this reaction pressure have a wide distribution. The intensity of the lower frequency RBM peaks, corresponding to SWNT of larger diameters,
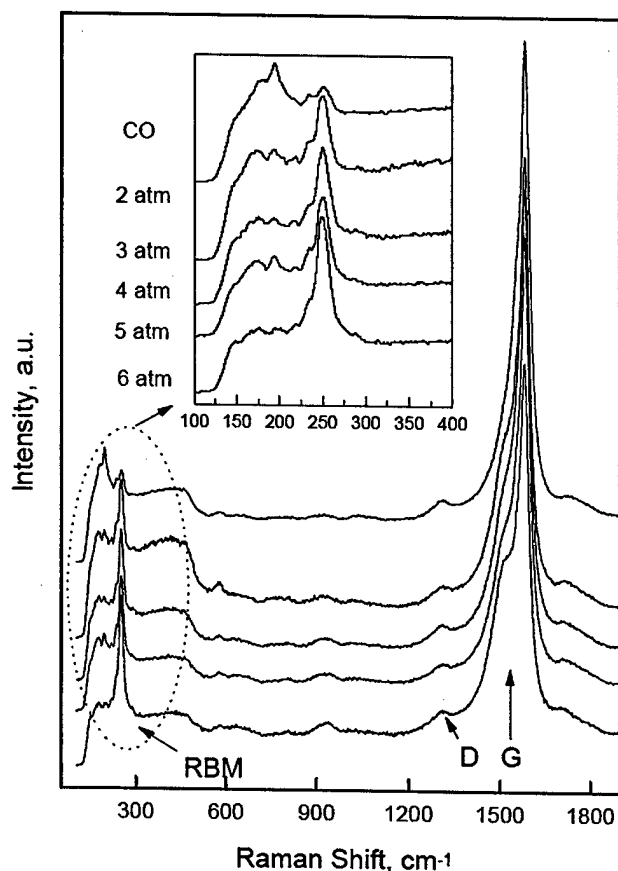
Fig. 1. Raman spectra recorded for SWNT grown at different CO pressures. The inset shows an enlargement of the Raman breathing mode region.

decreases as the CO pressure increases. The RBM region of the spectrum recorded with the SWNT grown at 6 atm shows a single, strong peak, indicative of a narrow diameter distribution of the SWNT produced. The presence of a narrow distribution of tube diameters in the SWNT sample grown at 6 atm has been confirmed by multiexcitation wavelength Raman spectroscopy as depicted in Fig. 2a. In contrast with the spectra recorded for the sample synthesized at 2 atm CO given in Fig. 2b, the spectra for the high-pressure sample show only one peak for each laser frequency. It should be noted that the laser frequencies at 633 nm (1.96 eV) and 785 nm (1.58 eV) are more sensitive to the larger tubes in the samples grown at 2 atm CO than the higher energy lasers. The intensity of the RBM peaks relative to the intensity of the G band determined from the multiple excitation Raman spectra increased when the reaction pressure increased. The total carbon loading determined by TGA and plotted as a function of pressure in Fig. 3 also shows an increasing trend as the CO pressure increases. These results indicate a strong effect of the CO pressure on both carbon yield and selectivity for SWNT, and diameter uniformity. At higher CO pressures larger amounts of carbon deposit on the surface in the form of SWNT of a narrower diameter distribution. These results are consistent with previous experimental observations of Nikolaev et al. for SWNT synthesis by thermal decomposition of iron pentacarbonyl in a heated flow of carbon monoxide [12].

Because of their weak intensity and the strong dependence of resonances on the tube diameter [27,28], the relative peak intensities for the several peaks in the RBM region
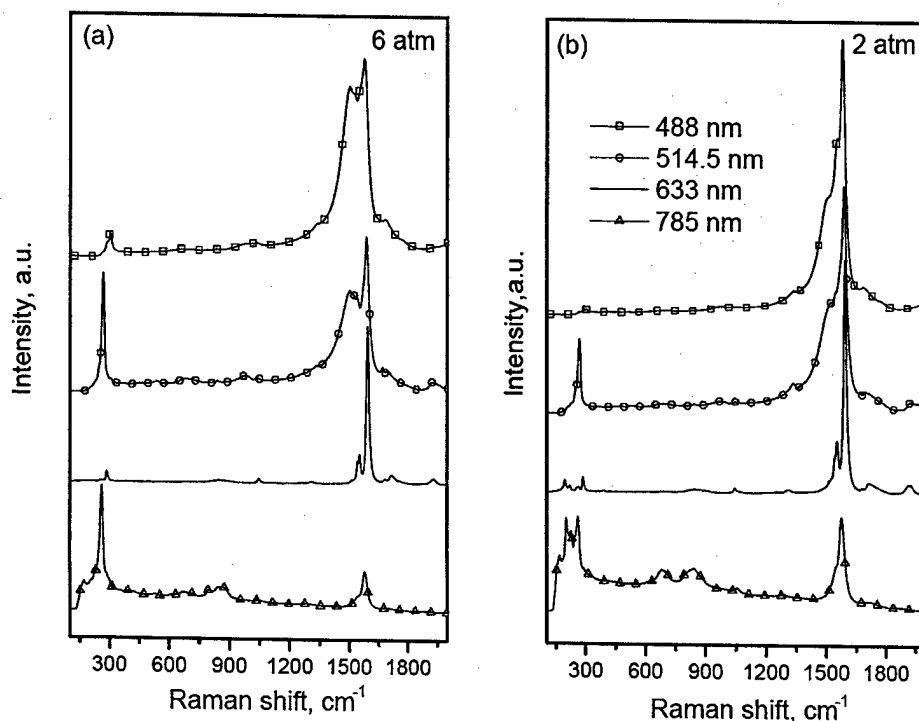

Fig. 2. Multiexcitation wavelength Raman spectra recorded for SWNT grown at 6 (a) and 2 atm CO pressure (b).
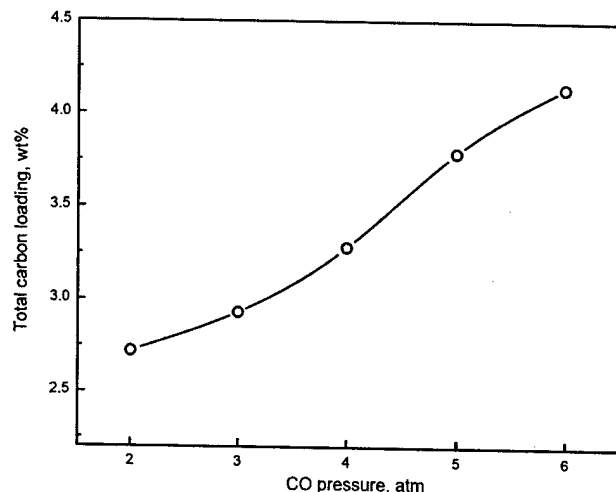
Fig. 3. Total carbon yield as a function of the CO pressure.

cause of its wide transmission window, and because it was reported to require a minimal application of ultrasound to disperse the SWNT [30].

The NIR absorption spectra in Fig. 4a recorded for nanotubes grown at different CO pressures show the main characteristic absorption band centered at approximately 1200 nm. This band can be assigned to the electronic transitions between the first pair or the second pair of van Hove singularities (VHS), depending on the diameter of the SWNT in the sample. According to the SWNT electronic band theory [31], if the band at 1200 nm comes from the second VHS, the diameter of the SWNT should be around 2–3 nm, while if it belongs to the first VHS, the diameter is about 1 nm. From the Raman spectra and the TEM results we can only identify SWNT with diameters below 1 nm, therefore this band is assigned to the first VHS, i.e., E_{11}^S.

Optical spectroscopy has been previously employed to perform analysis of the SWNT mean diameter and diameter distribution in carbon nanotube samples [32]. Aggregation of nanotubes into bundles substantially broadens and redshifts the absorption features [33,34]. Akasaka et al. used a three-step wet chemistry procedure to purify and separate the SWNT, and observed fine structures in the optical absorption spectra of the carbon nanotube samples, which were assigned to SWNT with different diameters and helicity [35]. The short-time sonication performed in our sample preparation procedure does not isolate the SWNT from bundles, as suggested by the broad spectra shown in Fig. 4a and confirmed by many TEM experiments. However, the rela-

cannot be easily related to the abundance of each tube diameter in the sample. Optical spectroscopy of the SWNT produced at different pressures provides a more sensitive diagnostic technique for analyzing the relative concentrations of tubes of different diameters in our samples.

The electronic structure of the SWNT can be easily altered by adsorption of chemical species on their surface [29]. To minimize such processes and preserve their original electronic structure we dispersed the SWNT samples, without purification or any other treatment, in dimethylformamide by sonication for 5 min. The DMF solvent was preferred be-
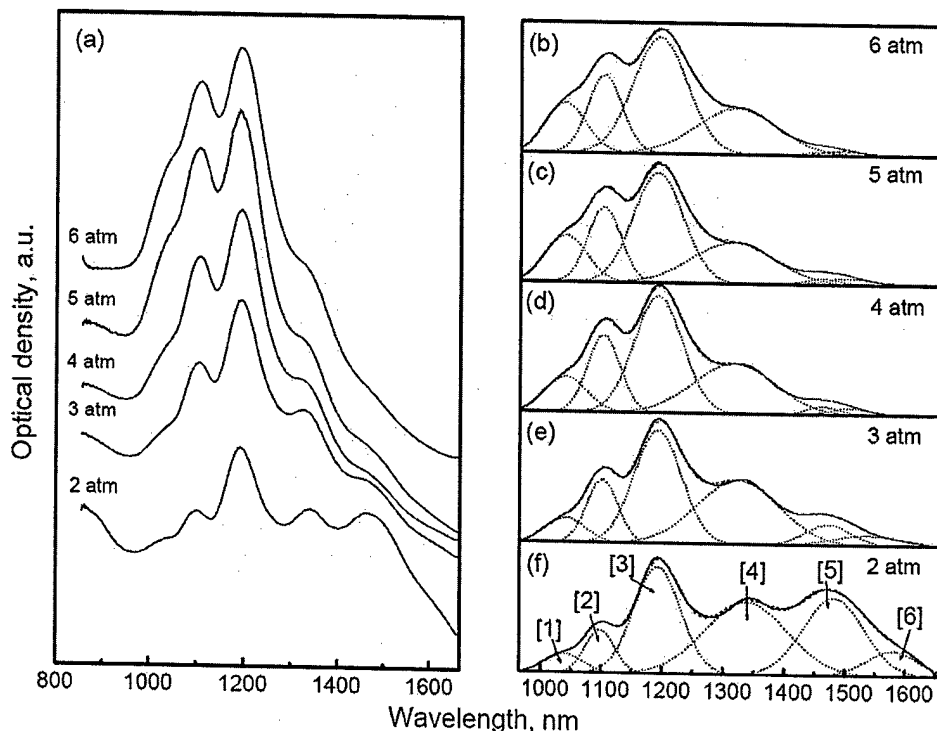

Fig. 4. NIR spectra of SWNT dispersed in DMF: (a) Spectra of SWNT synthesized at different CO pressures from 2 to 6 atm; (b–f) spectra after background correction (solid lines), and the six peaks resulting from deconvolution using a Gaussian-fitting function (dot lines).

tive differences in the diameter of these SWNT samples are clearly evidenced in these spectra. The solid lines in Figs. 4b to 4f show the baseline-corrected NIR absorption spectra in the range of 960–1660 nm for SWNT samples grown at different pressures. These spectra were deconvoluted into six peaks identified and resolved in our spectra using a Gaussian fitting function. As discussed above, because our tubes are most likely bundled, the peaks resulting from deconvolution correspond to the average electronic properties of SWNT in bundles. Weisman et al. pointed out that the tight-binding model badly underestimated the apparent scattering arising from chiral variation at a given diameter [36]. Using the empirical Kataura plot developed by these authors we assigned the six peaks to six groups of bundled SWNT having average diameters from 0.68 to 1.38 nm. Groups 1 and 2 have smaller diameters than groups 5 and 6, while SWNT with absorptions in groups 3 and 4 have intermediate diameters and are the major species produced in each sample.

Assuming the SWNT synthesized in Co-MCM-41 show the normal 1:2 distribution between metallic and semiconducting tubes [1], respectively, the narrow diameter distribution suggested for the semiconducting tubes in the NIR spectroscopy was verified in the multiple excitation wavelength Raman spectroscopy experiment, which shows a single peak at each laser line for the samples grown at high CO pressure. Therefore, the diameter distribution of the semiconducting SWNT determined here from optical spectroscopy is representative for the overall diameter distribution of the SWNT sample, including the metallic tubes. Plotting the normalized area of each peak resulting from deconvolution in Fig. 5a for samples grown at different pressures we observed that

the fraction of smaller diameter tubes in groups 1 and 2 increased when the CO pressure increased, while the fraction of larger diameter tubes in groups 5 and 6 decreased with the increase in CO pressure, as depicted in Fig. 5b. Therefore it is concluded that higher CO pressure produces smaller diameter SWNT while lower CO pressure produces larger diameter SWNT.

We have previously demonstrated that the isomorphous substitution of Si ions in the MCM-41 by cobalt ions impedes the complete reduction of cobalt to metal under moderate reduction conditions, i.e., treatment at 500 °C in pure hydrogen [3]. A direct consequence of this stabilization effect of the MCM-41 framework on the Co^{2+} ions is that exposure of a catalyst pretreated in hydrogen at 500 °C to pure CO at SWNT synthesis temperatures leads to the formation of very small metallic cobalt clusters in the MCM-41 molecular sieve. We have demonstrated that these cobalt clusters control the diameter of SWNT grown [3]. Along these lines, the diameter distribution of the SWNT provides indirect information on the size distribution of the cobalt clusters formed during SWNT synthesis. The signatures of the large SWNT observed in the Raman spectra in Figs. 1 and 2b and in the NIR spectra in Fig. 4a suggest that catalyst exposure to 2 atm CO produces larger cobalt clusters than those produced by exposure to 6 atm CO at the same reaction temperature. On the other hand, the larger number of cobalt clusters presumably formed during reduction at higher CO pressure should provide more sites for SWNT growth and, assuming at least first-order SWNT growth kinetics with respect to the CO concentration, the higher CO pressure should increase the SWNT growth rate. These two rationales are consistent
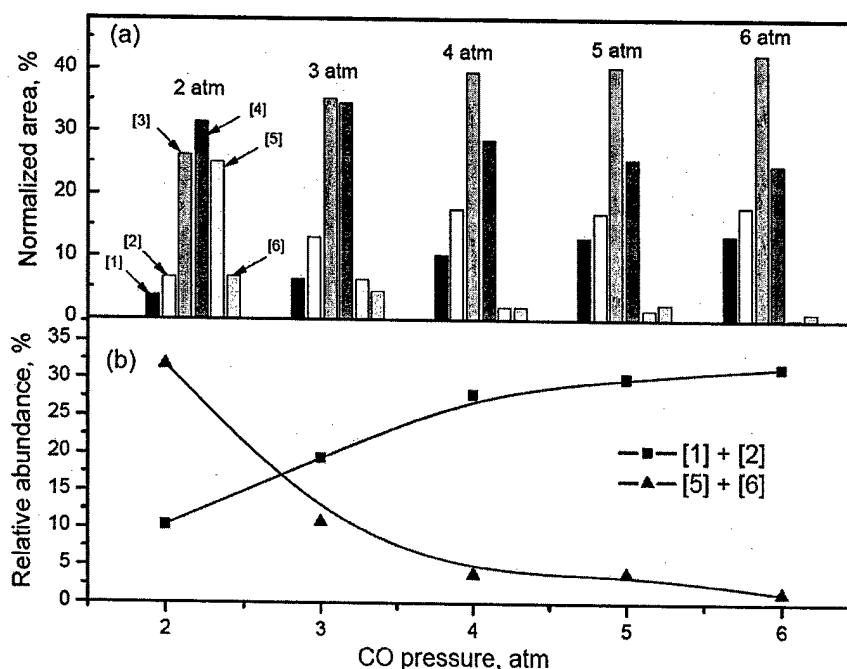

Fig. 5. (a) The size distribution of semiconducting SWNT synthesized at different CO pressures as determined from NIR spectra. (b) The relative abundances of small and large tubes as functions of CO pressure during SWNT synthesis.
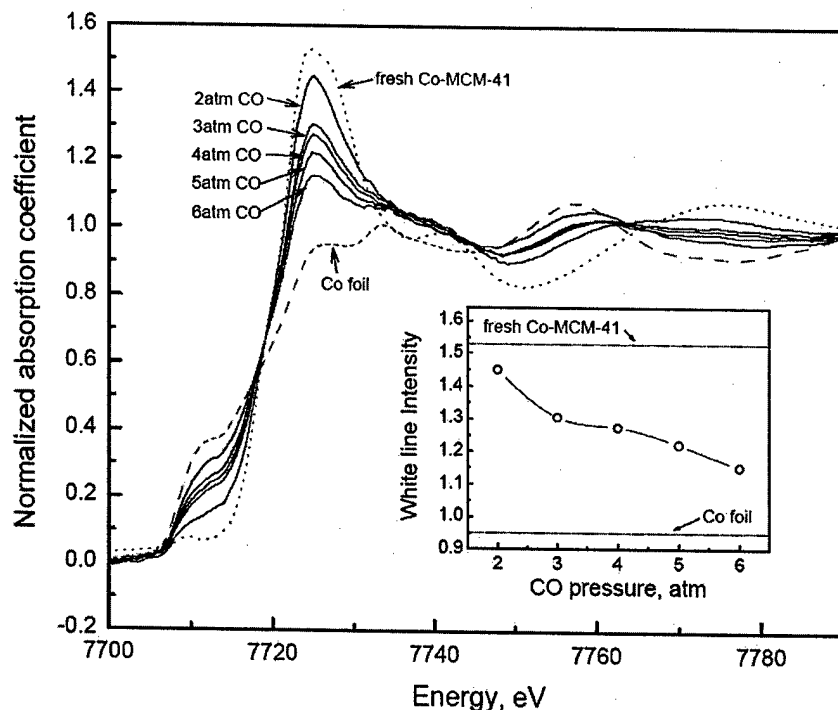
Fig. 6. Normalized EXAFS spectra near Co K edge recorded for Co-MCM-41 loaded with carbon after reaction at different CO pressures. Spectra for the fresh Co-MCM-41 and cobalt foil are given as references. The inset shows the correlation between the intensity of the white line and the CO pressure.

with the increase in the carbon yield when the CO pressure increases, as observed in Fig. 3. It should be noted that the intensity of the RBM peak relative to the intensity of the G band for all 4 laser frequencies also increases as the pressure increases, suggesting that more graphitic carbon is formed at lower pressures. Since we have shown that small particles are selective for SWNT growth and large particles form predominantly graphite [22], this evolution is a second reason to propose that exposure at lower CO pressures leads to the formation of larger cobalt particles.

These observations are intriguing as, assuming a non-zero positive order for the kinetics of cobalt reduction with respect to CO, one would expect a higher CO partial pressure to accelerate Co reduction, generate a higher metallic cobalt concentration on the pore wall surface, and, thus, form larger metallic clusters. Quantitative determinations of the cobalt cluster sizes after reaction at different pressures are thus required to understand these intriguing experimental results. The state of cobalt and the size of the metallic clusters in the catalyst samples were investigated by EXAFS. The white line features and the preedge peak details near the Co K edge (7709 eV) were obtained after energy edge calibration using a cobalt foil reference, background removal, and edge-step normalization using the FEFFIT program [37], following a procedure described elsewhere [22]. The resulting spectra for samples reacted at different pressures are shown in Fig. 6, along with the spectra for the fresh, fully oxidized catalyst and that of the cobalt foil, given as references.

The near-edge region of the X-ray absorption spectra recorded for the cobalt foil shows a strong preedge peak characteristic of metallic cobalt. The white line feature resulting from the density of unoccupied states above the Fermi level is attributed to the oxidized cobalt. The increase of the preedge spectral feature for the Co-MCM-41 catalyst after SWNT growth, associated with the decrease in the white line intensity (the white line peak height) as the CO pressure increased, is direct evidence for the increase in the amount of completely reduced cobalt in the catalyst as the SWNT are synthesized at higher CO pressure. The inset in Fig. 6 shows the variation of the intensity of the white line with the CO pressure, indicative of the degree of cobalt reduction in the catalyst. While some of the cobalt reduced during reaction may be reoxidized after catalyst exposure to the atmosphere leading to the increase of the white line intensity, the strong intensity of the preedge feature suggests that the concentration of the reoxidized cobalt is small and should not affect the overall trend of the variation of the white line intensity with the CO pressure. The spectra of the fresh Co-MCM-41 and of the Co foil have white line intensities of 1.53 and 0.95, respectively. As the CO pressure increases from 2 to 6 atm, the intensity of the white lines decrease from 1.44 to 1.15, clearly showing different degrees of cobalt reduction for reaction at different CO pressures. The intermediate intensity of white line and the position of the preedge peaks for the Co-MCM-41 samples after SWNT growth indicate that Co in MCM-41 is a mixture of metallic Co clusters and oxidized cobalt isomorphously substituted for Si^{4+} in the MCM-41 framework.

The FEFFIT program was employed to fit the EXAFS spectra using the first shell for both reduced and oxidized
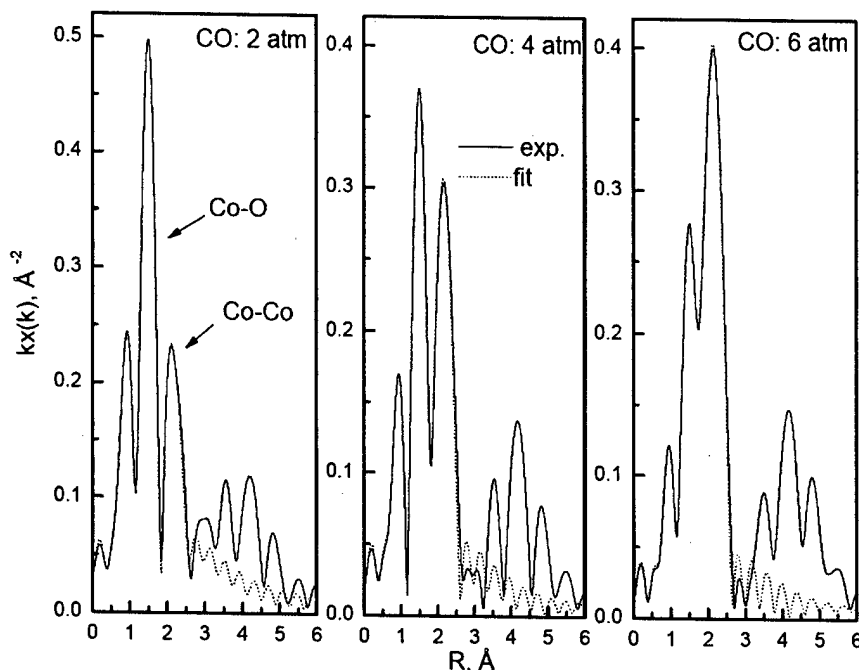
Fig. 7. EXAFS data for Co-MCM-41 catalysts after reaction at different CO pressures in R space along with the fittings of the spectra with theoretical models.

cobalt species (Co and Co_3O_4), as generated by the FEFF6 program [38]. In a previous study we observed that there was no significant contribution of the Co–C interaction to the fitting results for the spectra collected for catalyst samples reacted with CO under the conditions used in this study [39]. The fitting was limited to a k range from 2.2 to 10.0 Å^{-1}, k weight, with modified Hanning window, $dk = 1.0$ Å^{-1}, and an R range from 1.2 to 2.7 Å. The energy shifts for each shell varied insignificantly for samples reacted under different CO pressures; therefore the energy shift was set constant at 5.57 eV for the Co–Co shells and 2.41 eV for the Co–O shells, respectively. The passive electron reduction factor (S_0^2) was set to 0.9, as recommended by Rehr and co-workers [40]. Examples of the fitting results are shown in Fig. 7, and the corresponding Co–Co and Co–O first-shell coordination numbers are given in Table 1.

The k-weighted EXAFS spectra and the fitting results for samples reacted under 2, 4, and 6 atm CO pressure given in Fig. 7 show good agreement between the fittings and the experimental data in the selected fitting window. The fitting results were not highly sensitive to the windowing parameters. As expected, the two major peaks corresponding to the Co–O and Co–Co bonds show that the concentration of reduced cobalt increases with the CO pressure.

The changes in the structural parameters resulting from the fitting and presented in Table 1 confirm the different degrees of Co reduction suggested by the evolution of the white line intensity and the preedge peaks in Fig. 6. The Co–O coordination number decreases when CO pressure increases.

The X-ray absorption spectroscopy has been used previously to determine the size of nanoparticles because of the strong and nonlinear correlation between the particle diameter and the coordination number of atoms in clusters smaller than 2 nm [3,41,42]. However, application of EXAFS to determine the size of finely dispersed clusters is limited by the insensitivity of this technique to polydispersity [43,44]. While in our previous EXAFS studies of SWNT growth on Co-MCM-41 we noted that the Co cluster size determined from EXAFS analysis averages in the large Co particles outside the pores of the MCM-41 material, the uniform distribution of the diameters of the SWNT produced, and the high selectivity for SWNT led us to conclude that the values predicted from the EXAFS spectra were close to the actual values because the Co particles growing SWNT were fairly uniform in size [3]. The presence of significant amounts of large Co particles should have altered both the SWNT diameter uniformity and the SWNT selectivity by production of graphite and amorphous carbon. Therefore, in these previ-

Table 1

Structure parameters determined from the EXAFS fittings for Co-MCM-41 catalysts reacted at different CO pressures

CO pressure (atm)	Co–O first shell			Co–Co first shell		
	N_{Co-O}[a]	dR (Å)[b]	σ^{2c}	N_{Co-Co}[d]	dR (Å)[b]	σ^{2c}
2	1.87 ± 0.91	0.14 ± 0.02	0.85	2.44 ± 1.92	−0.04 ± 0.05	0.85
3	1.31 ± 0.66	0.13 ± 0.02	0.67	3.95 ± 1.43	−0.03 ± 0.02	0.67
4	1.13 ± 0.55	0.13 ± 0.02	0.75	4.60 ± 1.34	−0.03 ± 0.02	0.75
5	0.93 ± 0.51	0.13 ± 0.02	0.68	4.95 ± 1.17	−0.03 ± 0.01	0.68
6	0.73 ± 0.27	0.13 ± 0.01	1.48	7.10 ± 0.87	−0.02 ± 0.01	0.80

[a] N_{Co-O} average first-shell coordination of cobalt–oxygen.

[b] dR deviation from the effective half-path-length R (R is the interatomic distance for single scattering paths).

[c] σ^2 ($\times 10^{-2}$ Å^2) mean-square deviation in R.

[d] N_{Co-Co} average first-shell coordination of cobalt.

ous high CO pressure studies, there were no contradictions between the EXAFS results and the Raman spectra of the SWNT produced. However, the EXAFS results in this study are in an apparent contradiction with the diameter distributions of the SWNT grown on Co-MCM-41 at different CO pressures as characterized by TEM, and Raman and NIR spectroscopy: after reaction at 6 atm CO the catalyst shows cobalt clusters with larger Co–Co coordination numbers than those observed after reaction at 2 atm CO, but grows SWNT of smaller diameters with uniform distribution. In contrast, metallic clusters with lower Co–Co coordination number observed in the sample reacted at 2 atm CO produced SWNT with larger diameters and a wider diameter distribution.

The starting point in the interpretation of these experimental data is the understanding of the physical and chemical processes taking place in the catalytic system during the SWNT synthesis process. Our previous studies showed that the hydrogen prereduction treatment only partially reduces the cobalt in the catalyst without generating any metallic cobalt clusters [22]. During exposure to pure CO at higher temperature, however, cobalt is gradually completely reduced to metal and becomes more mobile on the surface. The EXAFS spectra plotted in the R space in Fig. 7 clearly show that the intensity of the Co–Co peak increases and that of the Co–O decreases as the reaction pressure increases for catalysts prereduced under identical conditions and reacted for the same duration of time at different CO pressures, giving direct evidence that more cobalt is reduced as the catalyst is exposed to higher CO pressures. Whether the cobalt migrates through the silica framework as an ion or a metal atom is not yet understood and the clarification of this mechanism is beyond the scope of this study. However, once the reduced atoms reach the pore wall surface, they start to nucleate into clusters of increasing size before they initiate the growth of a carbon nanotube or of other types of carbon on their surface. Since both the solubility of carbon into metallic particles [45] and the ability of the particle to dissociate CO decrease with the particle size, there is likely a minimum size required for the metallic Co cluster to initiate the growth of a SWNT. Along these lines, under certain reaction conditions, very small cobalt metal clusters that are not active for SWNT growth would likely be present in the pores. It should also be noted that we have observed that the growth of the Co clusters likely ceases once their surface is covered with carbon. Therefore, the final size and the size distribution of the cobalt clusters is controlled by the relative rates of the several physical and chemical processes affecting the structure and the state of the catalyst during the SWNT synthesis: cobalt reduction and migration through the pore wall to the pore wall surface, cobalt nucleation and growth into clusters, and carbon deposition.

With respect to the kinetics of cobalt nucleation and cluster growth, a weak interaction between the cobalt clusters and the pore wall would lead to rapid sintering and formation of large particles. Because in many instances the cobalt clusters formed in our Co-MCM-41 catalysts during

SWNT growth are very small (subnanometer), there is likely a strong interaction between the metallic clusters and the pore wall. This strong interaction may be an effect of the radius of curvature; i.e., a smaller pore radius of curvature would cause a stronger interaction between the Co clusters and the pore wall. This effect has been systematically investigated elsewhere [39]. In addition to the pore radius of curvature effect, a chemical-anchoring effect of the Co^{2+} ions still in the silica framework may also stabilize small Co metallic clusters against sintering. Stabilization of small metallic clusters by chemical anchoring has been previously observed in NaY zeolites where Fe^{2+} and Cr^{3+} ions stabilized small Pt clusters against sintering [46]. The same effect has also been reported for rhodium clusters in chromium ion-exchanged NaY zeolites [47]. Although these two effects are hard to demonstrate individually, they may both contribute to the stabilization of small metallic clusters in the MCM-41 molecular sieve.

Taking into account the above mechanisms, it is likely that a multimodal distribution of the Co particle size is responsible for the apparent contradiction between the EXAFS data and the Raman and NIR spectroscopy results, respectively. First, it should be noted that the overall carbon yield is considerably lower at low CO pressure, suggesting that fewer Co species are available for carbon deposition, as confirmed by the X-ray absorption results shown in Fig. 7. Assuming first-order reduction kinetics with respect to CO, a lower surface Co concentration is consistent with a lower degree of Co reduction at lower CO pressure, as suggested by the variations of the white line intensity and the preedge spectral feature depicted in Fig. 6. The Raman spectra suggest that a larger fraction of the carbon is graphite in the sample produced at lower pressure, consistent with the presence of large Co particles. SWNT with a broad distribution of diameters are also observed in the TEM micrograph in Fig. 8A recorded for the sample reacted at 2 atm, while the image in Fig. 8B shows uniform diameter SWNTs in the characteristic closed hexagonal packing [3]. TEM analysis did not give evidence of large Co particles on the surface most likely because there are just a few large particles in one specimen and their size may still be below 2.85 nm, thus still being accommodated inside the pores of the MCM-41 material. These results suggest a small fraction of reduced cobalt can be converted into larger particles at lower CO pressures. Second, the lower Co–Co coordination number can be explained by the presence of many clusters of smaller diameter that counterbalance the contribution of the large diameter particles to the overall Co–Co coordination number observed experimentally. Therefore, the overall picture consistent with these results is an interior pore wall surface decorated with many cobalt clusters with sizes below the minimum size required to grow carbon nanotubes, and a few larger cobalt clusters with a wide distribution of sizes and able to grow SWNT, graphite, and amorphous carbon. The small Co clusters are strongly anchored to the pore wall surface, most likely on Co^{2+} ions embedded into the pore wall near the surface. This
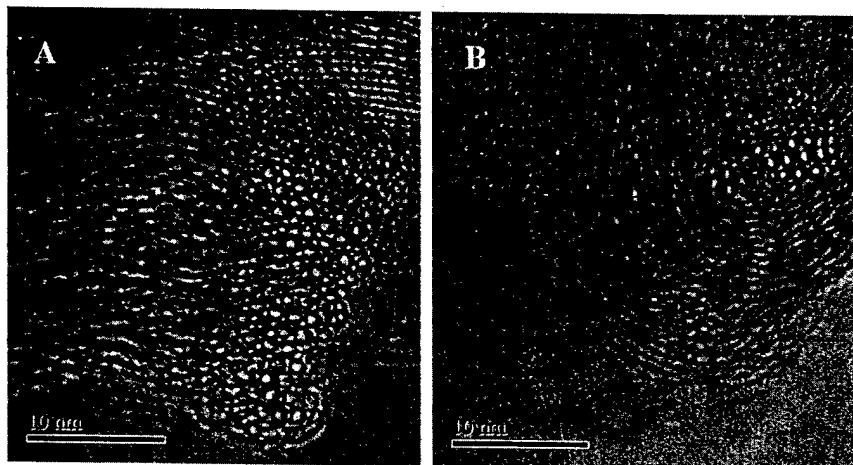
Fig. 8. Transmission electron micrographs showing (A) as-synthesized SWNT of different diameters grown on Co-MCM-41 at 2 atm CO pressure and 800 °C, and (B) as-synthesized uniform diameter SWNT grown at 6 atm CO pressure and 800 °C.

bimodal distribution of Co cluster sizes will result in an average Co–Co coordination number (weighted by the volume of particles of each size, not by their diameter) corresponding to a cluster size somewhere between the diameters of the large and the small Co clusters present in our sample. Depending on the relative concentration of these two populations of clusters/particles, the resulting average size could be closer to the smaller or to the lager particles size. It has been shown from calculations that, for example, a particular bidisperse system containing Pt clusters of 13 and 1415 atoms will show the same Pt–Pt coordination number with a system containing monodisperse clusters formed from 147 Pt atoms [44]. Taking into account the low carbon yield and low Co–Co coordination number observed for the sample reacted at 2 atm CO, it is likely that most of the reduced cobalt in this sample is in the form of cobalt clusters of sizes smaller than the critical size required for carbon growth and/or unreduced Co^{2+}. The presence of few large Co clusters that generate SWNT, graphite, and amorphous carbon is most likely due to the slower rate of carbon growth at lower pressures, thus giving more time to the small clusters to nucleate before they can grow either SWNT or other carbon species. This is also consistent with the low carbon yield and SWNT selectivity at low CO pressures and with the X-ray absorption experiments showing less metallic cobalt evolved after reaction at 2 atm. However, some larger cobalt particles may also be a product of the more rapid reduction of the small concentration of Co^{3+} species (~ 4% from the total cobalt loading) initially present in the sample. This species reduces at lower temperatures, as discussed elsewhere [39]. This would contribute a larger fraction of the metal clusters in the 2 atm case because the total fraction of reduced cobalt at this pressure is smaller.

3.2. Reaction time

A separate series of experiments was designed to investigate the influence of duration of the catalyst exposure to CO

on the SWNT synthesis performance quantified by the yield, selectivity, and diameter uniformity of the nanotubes produced. SWNT were grown by catalyst exposure to CO for different times between 5 and 120 min following the same pretreatment by hydrogen at 500 °C. The reaction conditions were controlled at 800 °C and 6 atm CO pressure. The Raman spectra of the Co-MCM-41 loaded with carbon after exposure to CO for different durations are shown in Fig. 9.
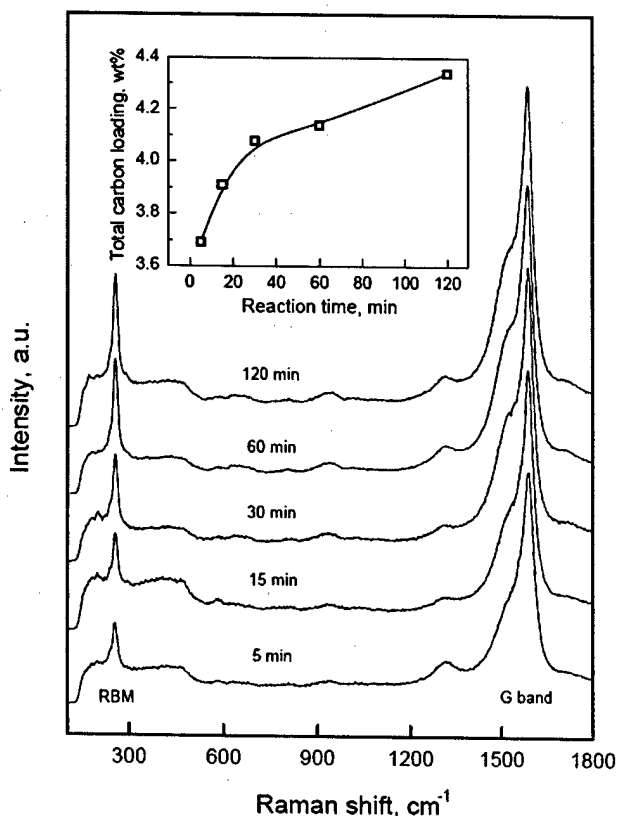

Fig. 9. Raman spectra recorded for SWNT grown at different reaction times. The inset shows the total carbon yield as a function of reaction time.
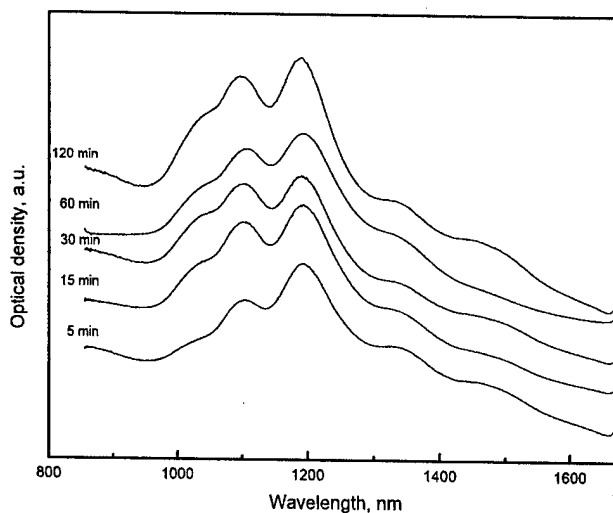
Fig. 10. NIR spectra of SWNT synthesized at different reaction times.

The positions of the peaks in Raman breathing mode region did not show significant changes when the duration of CO exposure increased from 5 to 120 min. Also, all the spectra showed rather weak D bands, indicating small amounts of amorphous carbon. The intensity of the Raman breathing mode peak observed for all four laser lines used have a slightly increasing trend relative to the intensity of the G bands as the catalyst is exposed to CO for a longer time, indicating that the selectivity to SWNT slightly increased. This behavior suggests that both the amorphous and graphitic, non-SWNT carbon species form at the early stages of carbon deposition rather than continuously during SWNT synthesis, possibly because they are formed on the more reducible cobalt. Similar results were previously reported by Alvarez et al. [15]. This behavior is consistent with large metallic particles being covered with graphitic carbon as soon as they are contacted with CO, while the SWNT growth initiated on Co clusters produced reduction of the cobalt ions from the pore walls on exposure to CO. Once they reach a critical size, these clusters initiate the growth of SWNT increasing the SWNT selectivity in the final product.

The diameter distribution of SWNT produced after catalyst exposure to CO for different durations was also characterized by NIR absorption spectroscopy, as shown in Fig. 10. The spectra recorded with catalyst samples exposed to CO for different durations are almost identical, indicating that the SWNT diameter distribution does not change significantly when the exposure to CO increased from 5 to 120 min, consistent with the conclusions drawn from the Raman results.

The carbon loading increased when the CO exposure increased from 5 to 30 min, as shown in the inset of Fig. 9. This behavior indicates that cobalt reduction and nucleation into metallic clusters and the CO disproportionation to grow carbon species are simultaneous and, thus, competitive processes. The carbon yield increases steeply during the first 30 min of CO exposure, and increases at a lower

rate after subsequent exposure, consistent with previous results reported by Alvarez and co-workers [15]. However, the SWNT selectivity of the carbon grown at the early stages of CO exposure is lower compared to that of the carbon grown for longer time, as suggested by the weaker intensity of the RBM peak. This behavior suggests that cobalt reduction is faster at the early stages of CO exposure and some of the clusters nucleate into large particles selective for graphite deposition. The large particles are most likely formed from a small portion of the incorporated Co in the form of Co^{3+} ions that are not as strongly bound to the framework. Earlier studies showed a small portion of the incorporated Co (less than 4%) reduces at lower temperatures [39]. After the complete reduction of this Co^{3+} species, the Co reduction slows along with nucleation into clusters, and the SWNT growth rate exceeds the cluster growth rate. Thus the Co clusters have a higher probability of initiating SWNT growth (which stops cluster growth) before growing large enough to be nonselective for SWNT. Therefore, a slower rate of cobalt reduction is associated with a better SWNT selectivity.

Researchers have found that the growth rate of individual SWNT is very rapid, from a few milliseconds to about 1 s [4]. Alvarez and co-workers [16] have proposed that the yield of SWNT grown by CVD increases for hours [8,17,18]. This behavior has been attributed to a slow rate for the nucleation of metal particles. In these studies of SWNT growth on Co-Mo catalysts, the authors found that the carbon yield increased rapidly with reaction time during the first 2 h of CO exposure, while the SWNT selectivity remained relatively high. Our results obtained at different reaction times are consistent with these previously reported results.

Interestingly, unlike the strong effects of the prereduction and reaction temperatures, and of the CO pressure on the uniformity of SWNT diameter, the duration of catalyst exposure to CO does not seem to affect the diameter distribution of the SWNT. This behavior suggests that there is a rather narrow window of clusters sizes in which cobalt is selective for SWNT growth under high CO pressure and once that size is reached the SWNTs grow at a very fast rate and impede the further growth of the Co cluster initiating the growth of the nanotube.

The Co-MCM-41 catalysts loaded with carbon following exposure to CO for different durations were also investigated by X-ray absorption. Fig. 11 illustrates the near edge region of the spectra of Co-MCM-41 samples after exposure to 6 atm CO for different durations at 800 °C. While the intensity of the white line feature decreased and the intensity of the preedge peak increased as the duration of exposure of the catalyst to CO is increased from 5 to 15 to 30 min, the spectra recorded after catalyst exposure to CO for 60 and 120 min did not change significantly, suggesting that the cobalt clusters did not grow larger after 30 min exposure to CO. This has been confirmed by the evolution of the Co–Co and Co–O coordination numbers given in Table 2 as determined from the EXAFS spectra using the same procedure discussed above. The variation of Co–O coordination number with the
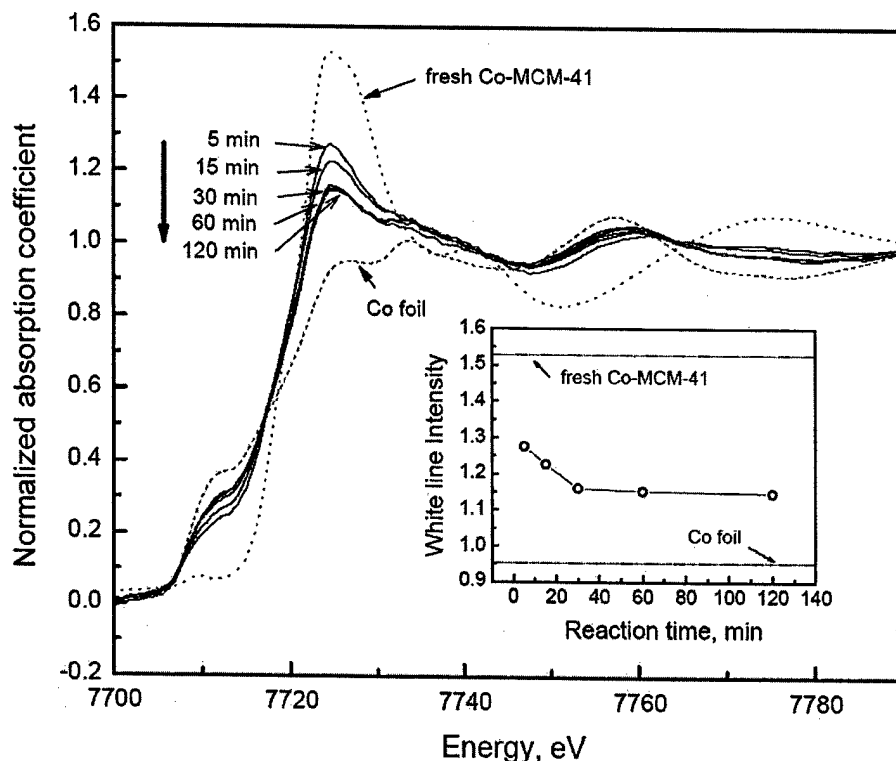
Fig. 11. Normalized EXFAS spectra near Co K edge recorded for Co-MCM-41 loaded with carbon at different reaction times. Spectra for the fresh Co-MCM-41 and cobalt foil are given as references. The inset shows the variation of the intensity of the white line with the reaction time.

Table 2
Structure parameters obtained from EXAFS fitting for Co-MCM-41 catalysts reacted for different durations

Reaction time (min)	Co–O first shell			Co–Co first shell		
	N_{Co-O}[a]	dR (Å)[b]	σ^{2}[c]	N_{Co-Co}[d]	dR (Å)[b]	σ^{2}[c]
5	1.18 ± 0.66	0.13 ± 0.02	1.05	4.43 ± 1.42	-0.03 ± 0.02	0.71
15	1.03 ± 0.47	0.13 ± 0.02	1.32	5.20 ± 1.25	-0.03 ± 0.01	0.74
30	0.78 ± 0.46	0.13 ± 0.02	1.26	6.81 ± 1.31	-0.02 ± 0.01	0.86
60	0.73 ± 0.27	0.13 ± 0.01	1.48	7.10 ± 0.87	-0.02 ± 0.01	0.80
120	0.71 ± 0.43	0.13 ± 0.03	1.29	7.13 ± 0.87	-0.03 ± 0.01	0.74

[a] N_{Co-O} average first-shell coordination of cobalt–oxygen.
[b] dR deviation from the effective half-path-length R (R is the interatomic distance for single scattering paths).
[c] σ^{2} ($\times 10^{-2}$ Å^{2}) mean-square deviation in R.
[d] N_{Co-Co} average first-shell coordination of cobalt.

duration of CO exposure mirrors the changes in the intensity of the white line, showing the same plateau for CO exposures longer than 30 min.

4. Conclusion

For SWNT synthesis by CO disproportionation on Co-MCM-41 catalysts both selectivity to SWNT and their diameter uniformity depend on the relative rates of the following three competitive processes: reduction of cobalt, nucleation of the reduced cobalt atoms into clusters, and initiation and

growth of the carbon nanotubes. The results presented here show that reaction at low CO pressures causes a slow rate of Co reduction, but also a slow rate of SWNT growth, allowing cobalt clusters to grow into larger sizes before they initiate the growth of SWNT, and leads to a wider distribution of SWNT diameters. In contrast, at high CO pressures, despite the higher Co reduction rates, the catalyst generates SWNT of uniform diameters likely because SWNT growth proceeds quickly once the catalyst cluster reaches the required size/conformation.

The experiments performed exposing the catalyst to CO for different durations indicated that this process variable significantly affects the SWNT synthesis performance only during the first 30 min of reaction. It has been shown that an initial amount of Co—likely the Co^{3+} species present in the fresh catalyst—is rapidly reduced and this process is associated with production of larger amounts of graphitic carbon. Exposure time to CO, however, does not significantly affect the diameter uniformity of the SWNT produced.

Acknowledgments

References

[1] T.W. Odom, J.-L. Huang, C.M. Lieber, Ann. N.Y. Acad. Sci. 960 (2002) 203.

[2] S. Lim, D. Ciuparu, C. Pak, F. Dobek, Y. Chen, D. Harding, L. Pfefferle, G. Haller, J. Phys. Chem. B 107 (2003) 11048.

[3] D. Ciuparu, Y. Chen, S. Lim, G.L. Haller, L. Pfefferle, J. Phys. Chem. B 108 (2004) 503.

[4] F. Kokai, K. Takahashi, M. Yudasaka, R. Yamada, T. Ichihashi, S. Iijima, J. Phys. Chem. B 103 (1999) 4346.

[5] E. Munoz, W.K. Maser, A.M. Benito, M.T. Martinez, G.F. de la Fuente, Y. Maniette, A. Righi, E. Anglaret, J.L. Sauvajol, Carbon 38 (2000) 1445.

[6] Y. Saito, Y. Tani, A. Kasuya, J. Phys. Chem. B 104 (2000) 2495.

[7] R. Zhang, R.K. Tsui, J. Tresek, A.M. Rawlett, I. Amlani, T. Hopson, P. Fejes, J. Phys. Chem. B 107 (2003) 3137.

[8] A.M. Cassell, J.A. Raymakers, J. Kong, H.J. Dai, J. Phys. Chem. B 103 (1999) 6484.

[9] W.Z. Li, J.G. Wen, Y. Tu, Z.F. Ren, Appl. Phys. A 73 (2001) 259.

[10] W. Liu, W. Cai, L. Yao, X. Li, Z. Yao, J. Mater. Sci. 38 (2003) 3051.

[11] M.J. Bronikowski, P.A. Willis, D.T. Colbert, K.A. Smith, R.E. Smalley, J. Vac. Sci. Technol. A 19 (2001) 1800.

[12] P. Nikolaev, M.J. Bronikowski, R.K. Bradley, F. Rohmund, D.T. Colbert, K.A. Smith, R.E. Smalley, Chem. Phys. Lett. 313 (1999) 91.

[13] C.E. Dateo, T. Gokcen, M. Meyyappan, J. Nanosci. Nanotechnol. 2 (2002) 523.

[14] T. Gokcen, C.E. Dateo, M. Meyyappan, J. Nanosci. Nanotechnol. 2 (2002) 535.

[15] W.E. Alvarez, B. Kitiyanan, A. Borgna, D.E. Resasco, Carbon 39 (2001) 547.

[16] W.E. Alvarez, F. Pompeo, J.E. Herrera, L. Balzano, D.E. Resasco, Chem. Mater. 14 (2002) 1853.

[17] M. Su, B. Zheng, J. Liu, Chem. Phys. Lett. 322 (2000) 321.

[18] J.H. Hafner, M.J. Bronikowski, B.R. Azamian, P. Nikolaev, A.G. Rinzler, D.T. Colbert, K.A. Smith, R.E. Smalley, Chem. Phys. Lett. 296 (1998) 195.

[19] H.J. Jeong, Y.M. Shin, S.Y. Jeong, Y.C. Choi, Y.S. Park, S.C. Lim, G.-S. Park, I.-T. Han, J.M. Kim, Y.H. Lee, Chem. Vapor Deposition 8 (2002) 11.

[20] O.A. Louchev, Y. Sato, H. Kanda, Appl. Phys. Lett. 80 (2002) 2752.

[21] Z.E. Horvath, L.P. Biro, G. Van Tendeloo, C. Tondeur, G. Bister, N. Pierard, A. Fonseca, J.B. Nagy, Diffus. Defect Data, Pt. B 94 (2003) 271.

[22] Y. Chen, D. Ciuparu, S. Lim, Y.Y., G.L. Haller, L. Pfefferle, J. Catal. 225 (2004) 453.

[23] A.M. Rao, E. Richter, S. Bandow, B. Chase, P.C. Eklund, K.A. Williams, S. Fang, K.R. Subbaswamy, M. Menon, A. Thess, R.E. Smalley, G. Dresselhaus, M.S. Dresselhaus, Science 292 (1997) 575.

[24] A.M. Rao, A. Jorio, M.A. Pimenta, M.S.S. Dantas, R. Saito, G. Dresselhaus, M.S. Dresselhaus, Phys. Rev. Lett. 84 (2000) 1820.

[25] M.S. Dresselhaus, A. Jorio, A.G. Souza, G. Dresselhaus, R. Saito, Phys. B 323 (2002) 15.

[26] R. Saito, A. Jorio, A.G. Souza, A. Grueneis, M.A. Pimenta, G. Dresselhaus, M.S. Dresselhaus, Phys. B 323 (2002) 100.

[27] M. Sugano, A. Kasuya, K. Tohji, Y. Saito, Y. Nishina, Chem. Phys. Lett. 292 (1998) 575.

[28] M.S. Dresselhaus, P.C. Eklund, Adv. Phys. 49 (2000) 705.

[29] M.S. Strano, C.A. Dyke, M.L. Usrey, P.W. Barone, M.J. Allen, H.W. Shan, C. Kittrell, R.H. Hauge, J.M. Tour, R.E. Smalley, Science 301 (2003) 1519.

[30] M.E. Itkis, D.E. Perea, S. Niyogi, S.M. Rickard, M.A. Hamon, B. Zhao, R.C. Haddon, Nano Lett. 3 (2003) 309.

[31] J.C. Charlier, P. Lambin, Phys. Rev. B 57 (1998) R15037.

[32] X. Liu, T. Pichler, M. Knupfer, M.S. Golden, J. Fink, H. Kataura, Y. Achiba, Phys. Rev. B 66 (2002) 045411.

[33] S.M. Bachilo, M.S. Strano, C. Kittrell, R.H. Hauge, R.E. Smalley, R.B. Weisman, Science 298 (2002) 2361.

[34] M.J. O'Connell, S.M. Bachilo, C.B. Huffman, V.C. Moore, M.S. Strano, E.H. Haroz, K.L. Rialon, P.J. Boul, W.H. Noon, C. Kittrell, J.P. Ma, R.H. Hauge, R.B. Weisman, R.E. Smalley, Science 297 (2002) 593.

[35] Y.F. Lian, Y. Maeda, T. Wakahara, T. Akasaka, S. Kazaoui, N. Minami, N. Choi, H. Tokumoto, J. Phys. Chem. B 107 (2003) 12082.

[36] R.B. Weisman, S.M. Bachilo, Nano Lett. 3 (2003) 1235.

[37] E.A. Stern, M. Newville, B. Ravel, Y. Yacoby, D. Haskel, Phys. B 209 (1995) 117.

[38] A.L. Ankudinov, B. Ravel, J.J. Rehr, S.D. Conradson, Phys. Rev. B 58 (1998) 7565.

[39] S. Lim, D. Ciuparu, Y. Chen, Y. Yang, L. Pfefferle, G.L. Haller, J. Phys. Chem. B (2004), in press.

[40] L. Campbell, L. Hedin, J.J. Rehr, W. Bardyszewski, Phys. Rev. B 65 (2002).

[41] R.B. Greegor, F.W. Lytle, J. Catal. 63 (1980) 476.

[42] G.H. Via, J.H. Sinfelt, F.W. Lytle, J. Chem. Phys. 71 (1979) 690.

[43] J. Moonen, J. Slot, L. Lefferts, D. Bazin, H. Dexpert, Phys. B 209 (1995) 689.

[44] D. Bazin, J.J. Rehr, J. Phys. Chem. B 107 (2003) 12398.

[45] J. Rostrup-Nielsen, D.L. Trimm, J. Catal. 48 (1977) 155.

[46] M.S. Tzou, H.J. Jiang, W.M.H. Sachtler, Appl. Catal. 20 (1986) 231.

[47] M.S. Tzou, B.K. Teo, W.M.H. Sachtler, Langmuir 2 (1986) 773.

Mechanism of Cobalt Cluster Size Control in Co-MCM-41 during Single-Wall Carbon Nanotubes Synthesis by CO Disproportionation

Dragos Ciuparu,* Yuan Chen, Sangyun Lim, Yanhui Yang, Gary L. Haller, and Lisa Pfefferle

Department of Chemical Engineering, Yale University, New Haven, Connecticut 06520

Received: May 5, 2004; In Final Form: July 26, 2004

The mechanisms controlling the reduction of cobalt and the growth of metallic cobalt clusters in Co-MCM-41 catalysts at different stages in the process of single-wall carbon nanotubes (SWNT) synthesis were investigated both by in-situ and ex-situ X-ray absorption spectroscopy. We have found that prereduction of the catalyst in hydrogen at temperatures below 700 °C does not reduce the cobalt ions to metallic cobalt, but removes hydroxyl groups and oxygen ions creating oxygen vacancies and/or a partially reduced cobalt species. The prereduction treatment, however, does increase the density of electrons at the Fermi level weakening the interaction of Co^{2+} with the silica framework. Subsequent exposure of the catalyst to CO at 750 °C causes CO to strongly interact with the cobalt clusters most likely by the transfer of electrons into the d orbitals of Co. This strong interaction makes the cobalt more mobile at the surface and allows it to nucleate into clusters capable of dissociating CO and initiating the growth of SWNT. Prior to exposure to CO, the reduced cobalt species strongly interacting with the silica framework do not nucleate into larger clusters in the presence of He or H_2, preserving near atomic cobalt dispersion, as determined by EXAFS.

Introduction

Because the electronic properties of the single-wall carbon nanotubes (SWNT) depend on their diameter and chirality,[1] their use in large scale production of electronic devices is hindered by the high purity and diameter uniformity of the SWNT required for such applications. Several processes[2–4] synthesize SWNT of relatively high purity, among which the HiPCO and CoMoCAT processes are widely known. The CoMoCAT process was shown to produce SWNT with a narrow distribution of tube diameters with high selectivity.[5]

We have recently reported on our preliminary results moving toward the goal of being able to controllably preselect the diameter of the SWNT grown on a Co-MCM-41 catalyst.[6] We observed that the diameter of the SWNT produced correlates with the size of the cobalt clusters formed in our catalyst during the SWNT synthesis process and that by controlling process conditions and catalyst design, we can control the metal cluster size/state.[7] We have also observed a strong influence of the size of the cobalt clusters on their selectivity for SWNT and concluded that large cobalt particles are selective for amorphous carbon and graphite,[8] in agreement with results reported by other groups.[5] No metal particles were ever observed on the ends of the SWNT grown on Co-MCM-41 catalysts.

The good selectivity of the CoMoCAT process has been attributed to the presence of the molybdenum component in the catalyst, which stabilizes the oxidized cobalt against reduction and allows formation of small Co particles highly selective for production of SWNT.[9] The mechanism behind this stabilization effect has been proposed to derive from the formation of a very stable surface Co molybdate-like structure, which is slowly disrupted in the presence of CO by the formation of Mo carbide. The released cobalt agglomerates into small clusters that subsequently initiate the growth of SWNT.[10]

In our Co-MCM-41 catalyst, the oxidized cobalt species were also observed to be stabilized against reduction under severe reducing conditions.[7] We have proposed that the final size/state of the cobalt cluster and, thus, the uniformity of the diameter of the SWNT produced are most likely controlled by the relative rates of the several physical and chemical processes affecting the structure and the state of the catalyst during the SWNT synthesis: cobalt reduction and migration through the pore wall to the pore wall surface, cobalt nucleation and growth into clusters, and carbon deposition.[11] The experiments reported here were designed to investigate the mechanisms controlling the rates of cobalt reduction and cluster nucleation at different stages of the SWNT synthesis process.

Experimental Section

A Co-MCM-41 catalyst with 1 wt % cobalt loading (as determined by ICP-MS at Galbraith Laboratories, Knoxville, TN) was synthesized using a C16 organic template and a high purity Cab-O-Sil fumed silica source from Cabot Corporation. Because we have found the pH to strongly affect the reducibility of cobalt in the silica framework,[12] the pH was carefully controlled at 11.5 during the initial stage of the synthesis. Although this is likely near optimal for synthesizing Co-MCM-41 for carbon nanotube growth using the C16 alkyl template, SWNT growth as a function of pH during catalyst synthesis has not yet been optimized and likely varies with the alkyl chain length used as templating agent. The catalyst resulting from removal of the organic template by calcination had an average pore diameter of 28.5 ± 1 Å as determined from the nitrogen physisorption measurement using the BJH method.[13] The nitrogen adsorption–desorption isotherms were measured at −196 °C with a static volumetric instrument Autosorb-1C (Quantachrome).

The state of the cobalt catalyst and the size of the cobalt clusters were determined from the X-ray absorption spectra

* To whom correspondence should be addressed.

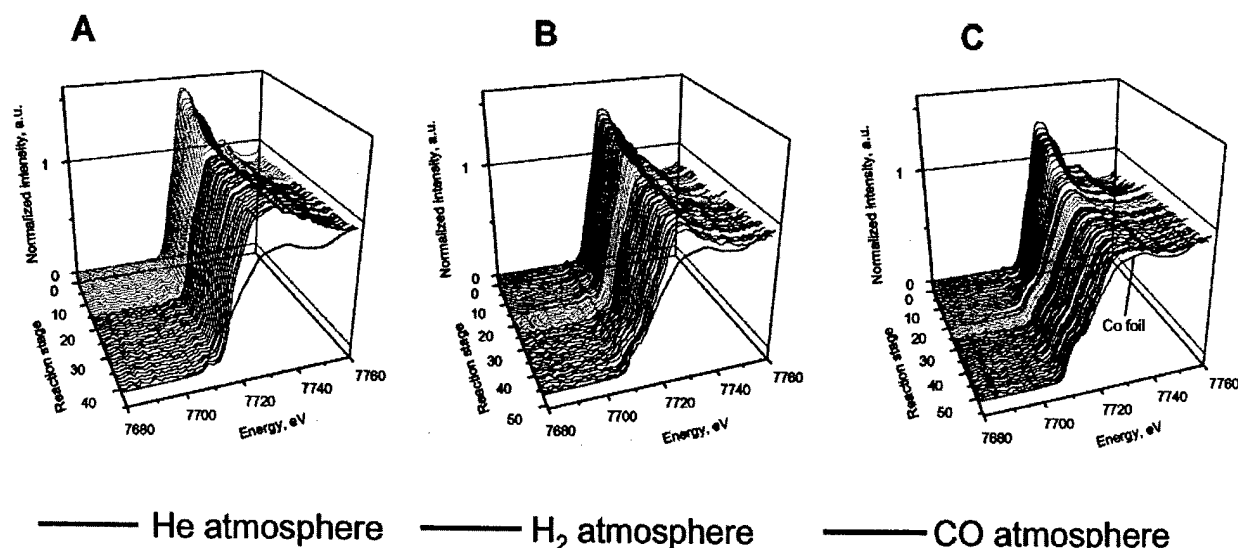15566 *J. Phys. Chem. B, Vol. 108, No. 40, 2004*

Ciuparu et al.

Figure 1. The XANES spectra recorded during Co-MCM-41 pretreatment under different conditions and SWNT synthesis at 750 °C for 1 h under 6 atm CO pressure: (A) no catalyst prereduction; (B) catalyst heating and prereduction in hydrogen at 500 °C for 30 min; (C) catalyst heating and prereduction in hydrogen at 700 °C for 30 min.

collected at beam line X23A2, National Synchrotron Light Source, Brookhaven National Laboratory. Two types of samples were measured: (i) ex-situ samples, consisting of catalysts submitted to different treatments and subsequently exposed to the ambient atmosphere, and (ii) in-situ samples, quenched at different stages of the carbon nanotube synthesis process and characterized before exposure to the ambient atmosphere. In-situ carbon nanotube growth experiments were performed to monitor the state of the catalyst during the SWNT synthesis process, consisting of the catalyst prereduction in hydrogen, heating in helium to the reaction temperature, and SWNT growth at CO pressures of 6 or 2 atm. For the in-situ experiments, 80 mg of fresh Co-MCM-41 were pressed at ~5 tons into a round self-supporting wafer (1.5 cm in diameter) using a hydraulic pellet press. The wafer was placed in the in-situ stainless steel reaction chamber described elsewhere.[8] During the in-situ experiment, the sample was heated in flowing hydrogen from room temperature to 500 °C (or 700 °C) at 20 °C/min and reduced isothermally for 30 min. Then, the catalyst was purged with ultrahigh purity helium at 500 °C (or 700 °C) and then heated to 750 °C at 20 °C/min in flowing helium. For the in-situ assessment of the state of the catalyst during different reaction conditions, X-ray absorption near-edge structure (XANES) spectra were continuously collected from 30 eV below to 50 eV above Co K edge in 1 eV steps, averaging approximately 3 min per scan.

Analysis of the spectra collected for the ex-situ samples followed the procedures described in detail in our previous work.[8] The EXAFS spectra recorded for ex-situ samples were calibrated to the edge energy of the cobalt foil internal reference. The background removal and edge-step normalization were performed using the FEFFIT code.[14] The theoretical EXAFS functions for different cobalt species (Co, Co_3O_4) generated by the FEFF6 program[15] were used to fit the experimental data to obtain the corresponding Co—Co and Co—O first-shell coordination numbers. Because of the short energy range of the in-situ XANES spectra, the postedge background of the XANES spectra was not long enough to obtain an accurate edge energy jump at E_0. To compare the XANES features observed in different experiments, assuming a constant Co atom concentration under the X-ray beam during reaction, we used the energy edge intensity measured from the EXAFS spectrum of the same

sample recorded after each in-situ reaction XANES series. The normalized XANES spectra for each series of in-situ experiments were obtained by subtracting the smooth preedge absorption and the fixed edge step determined from the analysis of the final EXAFS spectrum, as described above.

Results and Discussion

A first series of in-situ XANES experiments was performed varying the catalyst pretreatment conditions but maintaining reaction conditions. For the first experiment, the catalyst was simply heated to 750 °C under flowing helium and then reacted for 1 h under 6 atm of CO pressure at 750 °C. For the next two experiments, the catalyst was heated in hydrogen to 500 °C or 700 °C, held at this temperature for 30 min, then purged with helium and heated in flowing helium to 750 °C prior to exposure to 6 atm CO for 1 h at 750 °C. The normalized XANES spectra collected during these treatments are given in Figure 1. The spectra in Figure 1 are gray density coded so that those recorded under flowing helium have a light gray hue, while those recorded while catalysts are reduced in hydrogen at the early stage of the experiment (reaction stage values below 15 and 20 in Figures 1B and 1C, respectively) or during exposure to CO at 750 °C (reaction stage values higher than 24 in Figures 1B and 1C) are plotted in dark gray hue. The spectrum of the cobalt foil is given in each plot for reference.

A few spectra from Figure 1B are plotted in Figure 2 without any offset to clearly observe the changes in the main spectral features. The insert of Figure 2 shows the derivative of the Co foil spectrum. Three regions of the XANES spectrum provide information concerning the state of the catalyst. The first region of interest in the XANES spectrum is the preedge peak, which was assigned to the dipole forbidden 1s → 3d transitions whose intensities are strong functions of the local symmetry of the Co species.[16] The second region of interest is the energy of the Co K edge, as defined by the second peak in the derivative of the EXAFS spectrum given in the inset of Figure 2. The position of the K edge varies linearly with the valence of the Co species. The K edge of the fully reduced Co shifts to lower energy compared to the edge of the fully oxidized Co. Unlike vanadium, however, whose reduction from V^{5+} to V^0 produces a relatively large shift in the energy of the K edge,[17] Co exhibits a narrower

Mechanism of Cobalt Cluster Size Control

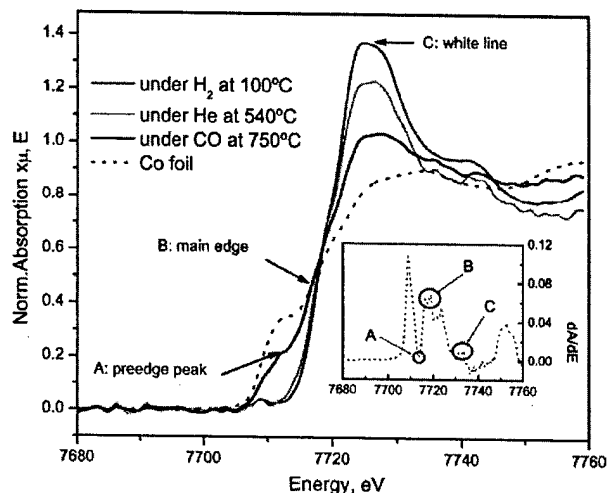*J. Phys. Chem. B, Vol. 108, No. 40, 2004* **15567**

Figure 2. The XANES region of the EXAFS spectra recorded for Co-MCM-41 under different atmospheres and for the cobalt foil reference. The inset shows the energy values corresponding to the preedge peak (A), main edge energy (B), and white line (C) as determined from the first derivative of the EXAFS spectrum recorded for the Co foil. The maximum intensity of the white line (~7725 eV) observed with the Co-MCM-41 samples is shifted to lower energy compared to that observed for the Co foil (~7730 eV).

range of oxidation states (0 to +3) and our starting material, Co-MCM-41, has Co^{2+} isomorphously substituted for silicon ions.[7] In our experiment, the K edge does not show significant shifts, in contrast with the other two spectral features. The intensity of the white line is the third region of interest since it is a direct measure of the density of empty states at the Fermi level of the cobalt species, with oxidized cobalt having a strong white line intensity, while the fully reduced Co metal produces a very weak white line feature.

The intensities of the preedge peak and of the white line were therefore selected as the two main features to monitor the

changes of the Co-MCM-41 catalyst during in-situ reaction. The normalized absorption intensity determined in the XANES spectra at the energy corresponding to the first minimum in the derivative of the Co foil spectra depicted by A in the inset of Figure 2 (i.e., 7713 eV) was considered the preedge peak intensity. The intensities of the white line peaks were determined similarly from the position of the second minimum depicted by C in the inset of Figure 2 (i.e., 7725 eV). The changes in the intensities of these spectral features determined for the experiments depicted in Figure 1 are given in Figure 3. The intensity of the white line was observed to decrease continuously as the samples were heated from room temperature to 500 °C in either flowing He or hydrogen (Figure 1A and 1B and Figure 3A and 3B). The initial decrease in the white line was not associated with any visible changes in the preedge feature of the spectra. These results indicate that during heating in hydrogen or helium the density of the electrons at the Fermi level of the oxidized cobalt increases. This is likely due to the surface dehydroxylation associated with formation of oxygen vacancies trapping one or two electrons each. Dehydroxylation, however, does not change significantly the symmetry of the cobalt ions since the preedge feature does not change. This implies that the hydroxyls removed from the surface are bound to silicon ions; thus, most of the cobalt ions are likely located inside the pore wall rather than exposed to the surface. Moreover, if the hydroxyls were bound to cobalt ions, their removal should have increased the oxidation state of the cobalt, which should have resulted in an increase in the white line intensity. Assuming an oxygen-terminated pore wall surface, as proposed by Feuston,[18] and an oxygen ionic radius of 1.24 Å and 0.72 Å for Co^{2+}, since the pore wall thickness determined from X-ray diffraction data is approximately 10 Å,[7] the minimum and the maximum depths in the pore wall at which a Co^{2+} ion can be found are approximately 2 and 4.3 Å, respectively. If the cobalt ions were located close to the surface, removal of their neighboring oxygen should affect both the white

−□− H_2 atmosphere −●− He atmosphere −▲− CO atmosphere

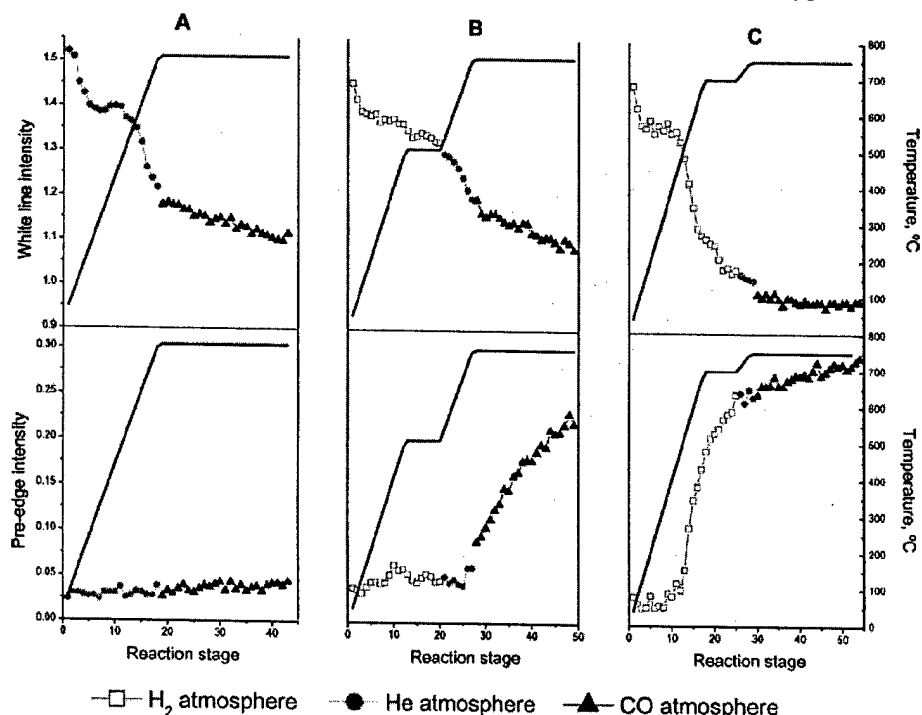**Figure 3.** Variation of the intensities of the preedge feature and of the white line during different treatments. The scales are the same for both temperature (right side) and intensity (left side) for the two spectral feature series. The solid lines show the temperature profile corresponding to each experiment. Graphs A, B, and C were built using the XANES spectra in Figure 1A, 1B, and 1C, respectively.

15568 *J. Phys. Chem. B, Vol. 108, No. 40, 2004*

Ciuparu et al.

line intensity and the preedge peak by changing both its oxidation state and symmetry. Along these lines, the cobalt ions are most likely located deeper in the pore wall. However, if the oxygen ion is replaced by an oxygen vacancy trapping two electrons, the preedge should not change, while the intensity of the white line can change significantly.

When the catalyst was heated in hydrogen to 700 °C (Figure 1C), a further decrease in the intensity of the white line was associated with a significant change of the preedge feature. The narrow and weak peak observed initially with the fully oxidized Co-MCM-41 samples at about 7709 eV becomes wider and more intense and shifts to 7713 eV, suggesting both a major change in the symmetry of the cobalt species and a broader distribution of the energy levels of the d orbitals that can accommodate the photoexcited core electron. These changes are most likely indicative of the formation of fully reduced, metallic cobalt clusters. In contrast, the catalyst heated in flowing helium after the pretreatment in hydrogen between room temperature and 500 °C with 30 min isothermal hydrogen reduction at 500 °C (Figure 1B) did not show any modification of the XANES spectra in the preedge region although the white line intensity continuously decreased. The cobalt could not be completely reduced when exposed to pure CO for 1 h even at 750 °C if the catalyst was not prereduced in hydrogen prior to the CO treatment (Figure 1A). In contrast, exposure to CO at 750 °C after prereduction with hydrogen at 500 °C does produce modifications of the preedge peak (Figure 1B). This behavior suggests that hydrogen prereduction at 500 °C produces changes in the electron density at the Fermi level of cobalt most likely due to the change of one or more of its ligands, or the $\equiv$Si$-$O coordinated to Co (i.e., exchange of a OH ligand with an oxygen ion or an oxygen vacancy, either directly in the coordination sphere of Co, or of the Si bonded through oxygen to Co), or to the partial reduction to an intermediary state (i.e., Co^{+x}), but higher temperatures and the presence of a reducing atmosphere (CO or hydrogen) are required for the complete reduction of cobalt to metal (Co^0). The main question arising from these experiments is how are the two reduction processes, by CO and by hydrogen, different. At high enough temperatures, treatment in hydrogen can completely reduce the cobalt; however, reduction of the Co by CO requires pretreatment of the catalyst in hydrogen at 500 °C.

It is postulated that hydrogen can penetrate the silica pore wall and, by removal of surface oxygen from silica, causes formation and migration of oxygen vacancies that allow cobalt to become mobile in the silica. Thus, prereduction of the catalyst facilitates the access of the CO to the partially reduced cobalt species embedded in the MCM-41 pore wall. After prereduction in hydrogen at 500 °C, the reduced cobalt is still atomically dispersed and chemically interacting with the silica. No change in preedge peak is evidenced, consistent with cobalt preserving its local symmetry in tetrahedral coordination.

To characterize the degree of reduction at different stages in the process, samples quenched at different stages were investigated by EXAFS. The spectra recorded for samples quenched after prereduction at 500 and 700 °C for 30 min are plotted in R space in Figure 4 along with the spectrum recorded for a sample prereduced 30 min at 700 °C, heated in He to 750 °C, and exposed for 1 h to 6 atm CO at 750 °C. The major peaks centered at R values of approximately 1.6 and 2.2 Å correspond to the Co$-$O and Co$-$Co interactions, respectively. The spectrum for the sample prereduced at 500 °C shows an insignificant Co$-$Co peak suggesting a very small fraction, if any, of the cobalt ions in the silica framework has been
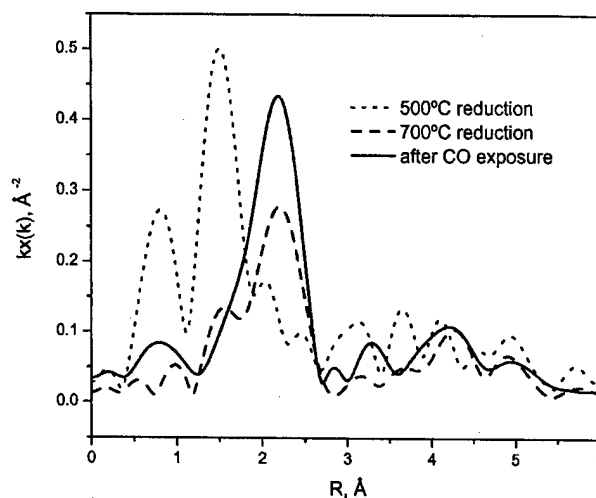
Figure 4. The EXAFS spectra plotted in R space for Co-MCM-41 samples exposed to different reducing treatments.

completely reduced to metal and made mobile to nucleate into small clusters to produce a Co$-$Co peak in the R space EXAFS spectrum. It is possible that there is some fully reduced cobalt after prereduction at 500 °C, but because these atoms remain isolated from other cobalt atoms in the silica framework they do not produce a Co$-$Co peak or a significant metallic preedge peak.

Prereduction at 700 °C, however, causes substantial Co reduction to the metal and nucleation into large clusters showing a strong Co$-$Co interaction in the EXAFS spectrum in Figure 4, as well as a significant metallic preedge peak (see Figure 3C). Despite the large fraction of reduced cobalt and, thus, the relatively high concentration of cobalt at the surface, the Co$-$Co coordination number is 4.2 indicating the metallic Co clusters contain approximately 12 atoms each, assuming the (111)-truncated hemispherical cubic octahedron model that was shown to provide the best approximation for the relation between the average coordination number and the size of small nanoparticles.[19] That such a Co cluster is stable in hydrogen at 700 °C is unprecedented; a possible mechanism for cobalt cluster stabilization consists of anchoring on cobalt ions stabilized in the oxidized state by the radius of curvature effects and was discussed in detail elsewhere.[7] Further 1-h exposure of the sample prereduced at 700 °C to CO at 750 °C results in almost complete reduction and allows cobalt particles to grow until the Co$-$Co coordination number reaches 6.4 (corresponding to clusters of 24 atoms), indicating some growth of the metallic clusters formed after prereduction at 700 °C.

The next experiments were performed to test the hypothesis of partially reduced Co remaining in the silica lattice after prereduction in hydrogen. Our previous experiments demonstrated that Co-MCM-41 samples in which all or some fraction of the cobalt ions were completely reduced to metal were easily reoxidized simply by exposure to the ambient atmosphere. A mild rereduction treatment in hydrogen at 400 °C for 30 min restored the state of the cobalt clusters observed prior to reoxidation by exposure to the ambient atmosphere. Such reoxidation should not be possible if the reduced cobalt clusters were not exposed at the surface, that is, if they were embedded within the silica framework. Two fresh Co-MCM-41 samples were reduced for 30 min in flowing hydrogen at 650 and 700 °C, respectively. After these pretreatments, the samples were exposed to the ambient atmosphere for several days prior to the measurement of their EXAFS spectra. The samples were pressed into self-supported pellets weighting 80 mg and mounted
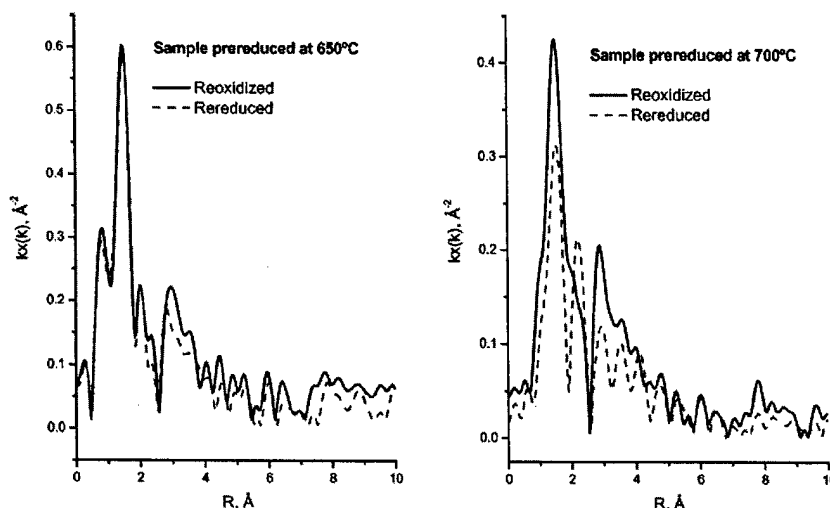
Mechanism of Cobalt Cluster Size Control

J. Phys. Chem. B, Vol. 108, No. 40, 2004 **15569**

Figure 5. The EXAFS spectra in R space for samples prereduced at 650 and 700 °C after exposure to ambient air and mild rereduction in flowing hydrogen for 30 min at 400 °C.

in the in-situ X-ray absorption cell. The EXAFS spectra recorded both before and after the mild rereduction treatment at 400 °C described above are plotted in Figure 5. It becomes evident in the spectra in Figure 5 that the mild rereduction treatment does not produce visible modifications in the spectrum for the sample prereduced at 650 °C, but it dramatically changes the spectrum of the sample prereduced at 700 °C. A weak Co—Co peak is present in the sample prereduced at 650 °C. Since this reduction temperature is higher than the onset of reduction observed in a related TPR experiment using 5% H_2 in He,[7] this weak peak is likely associated with reduced cobalt species still embedded in the silica framework. After exposure to ambient oxygen, while the Co—Co peak is clearly visible in the sample prereduced at 650 °C, it appears only as a shoulder to the Co—O peak in the sample prereduced at 700 °C. However, after the mild rereduction treatment this shoulder becomes a well-defined, intense peak giving evidence for a strong Co—Co interaction in metallic cobalt in the sample prereduced at 700 °C (as is seen in Figure 4 without exposure to ambient oxygen), indicating that reduction at high temperatures leads to the formation of Co clusters at the pore wall surface that can be easily reoxidized upon exposure to air. These differences clearly show that only slight differences in the prereduction conditions, that is, a 50 °C difference in the prereduction temperature, produce significant changes in the state of the catalyst, suggesting the formation of cobalt clusters has a rather high activation barrier.

Even more interesting is the fact that the Co—Co peak in the sample prereduced at 650 °C is not affected by the mild rereduction treatment, as opposed to the behavior of the sample prereduced at 700 °C, suggesting that the metallic species formed by prereduction at 650 °C are not exposed at the surface, or that they are resistant against oxidation upon exposure to the atmospheric oxygen pressure.

The presence of small metallic clusters embedded in or anchored to the silica framework would require either the diffusion of cobalt atoms through the silica framework to nucleate into small metallic Co clusters or diffusion of the reduced atoms through the pore wall to the pore wall surface, migration and nucleation on the surface, and then reincorporation or anchoring of the cluster into the pore wall. Assuming an atomic dispersion of the Co^{2+} ions in the silica framework, for 1% weight cobalt loading each Co^{2+} ion is surrounded by approximately 146 silicon ions and twice as many oxygen ions. This translates into a significant distance of at least 30 Å that

a reduced Co atom would have to travel until it would be able to meet a second atom to nucleate into a cluster. Along these lines, both of the scenarios discussed above seem unrealistic.

An alternative explanation is that the reduced Co atoms diffuse through the pore wall to the surface and nucleate into clusters of a few cobalt atoms that have a reduced chemical reactivity toward reoxidation during exposure to the ambient atmosphere. This high stability against reoxidation may be related to the inability of these clusters to dissociate oxygen, that is, such small clusters may not be capable of dissociating oxygen inherently, or dissociation may be inhibited by anchoring to cobalt ions bound to the silica matrix or, indeed, by direct Co—Si interaction at an oxide ion defect in silica. Once these clusters reach a critical size/morphology/electronic state, they start dissociating oxygen and become oxidized when contacted with the oxygen from the air.

In our previous reports on SWNT synthesis using CO disproportionation on Co-MCM-41 catalysts, we proposed that very small cobalt metal clusters that are not active for SWNT growth can likely be present at the surface and explained that their inability to initiate the growth of SWNT may be related to the low solubility of carbon into the small metallic Co clusters, or to their inability to dissociate CO.[11] The behavior of the Co-MCM-41 sample prereduced at 650 °C can be explained along the lines of our previously proposed hypothesis and is consistent with the near-zero Co—Co coordination number determined from the EXAFS spectrum for this sample.

The Co—Co coordination number determined from the EXAFS spectrum recorded after the mild rereduction of the Co-MCM-41 sample prereduced at 700 °C was 4.2 and increased to 6.4 for the sample further exposed to 6 atm CO at 750 °C for 1 h. The low Co—Co coordination number observed with the sample prereduced at 700 °C, along with the relatively large fraction of the reduced cobalt suggested by the EXAFS spectra plotted in the R space in Figure 5, suggests that the growth rate of the Co clusters is low in a hydrogen atmosphere even at 700 °C. Although this is expected because of the low cobalt loading (1 wt %) in this sample, the strong interaction between the small Co clusters and the curved pore wall of the MCM-41 host may also play an active role in anchoring the small clusters to the surface. The strength of this interaction is likely a function of the radius of curvature of the pore wall
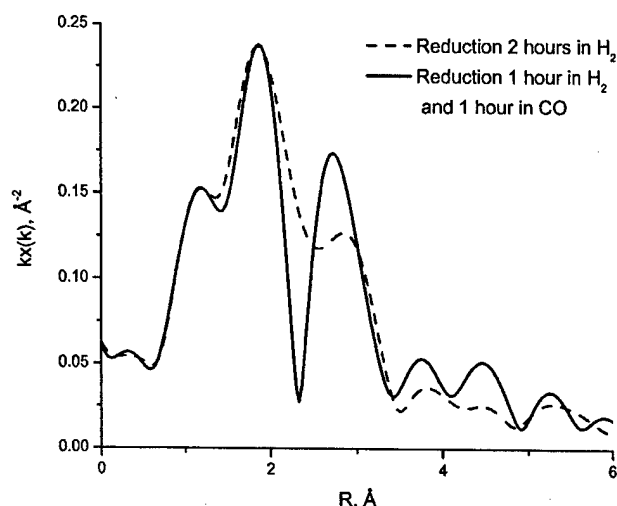
Figure 6. The EXAFS spectra in R space for Co-MCM-41 samples reduced 2 h in H_2, or 1 h in H_2, and 1 h in CO at atmospheric pressure and 650 °C.

offering an opportunity for "engineered" control, as discussed elsewhere.[7]

Assuming an oxygen-terminated pore wall surface as discussed above, a metallic cluster would be in contact with a layer of oxygen ions with a high density of electrons. Thus, a strong interaction between the Co cluster and this oxygen-terminated surface would imply a higher affinity for electrons for smaller Co metallic clusters. Such a strong interaction may be perturbed by adsorption of electron donor molecules, such as CO, leading to an increased mobility of the metallic cobalt clusters upon exposure to gas-phase molecules that can be bound at their surface. This is consistent with the sudden increase in the intensity of the preedge feature upon catalyst exposure to CO following prereduction in hydrogen for 30 min at 500 °C, as depicted in Figure 3B.

Indeed, the Co—Co coordination number observed for a Co-MCM-41 sample reduced in pure hydrogen at 650 °C for 2 h at atmospheric pressure was near zero, suggesting an atomic dispersion of the reduced cobalt in this sample. However, the EXAFS spectrum of this sample plotted in R space in Figure 6 shows a distinct Co—Co peak indicative of the presence of a few very small metallic clusters, confirming the complete reduction of some cobalt clusters observed for the sample reduced in hydrogen for 30 min at 650 °C (see Figure 5). When the same catalyst was reduced for 1 h in pure hydrogen and 1

h in pure CO at the same temperature and pressure, the Co—Co coordination number observed was 3.7 giving evidence for the formation of significantly larger cobalt clusters in the presence of CO compared to hydrogen. The intensities of the Co—O peaks for the samples exposed to different reduction strategies suggest that there is no significant difference in the degree of reduction for these two samples. Since we have shown that exposure of the Co-MCM-41 catalyst to 6 atm CO at 750 °C for 1 h only reduces the Co to a very small extent (see Figure 1A), these results are direct evidence that interaction of CO molecules with hydrogen prereduced Co-MCM-41 accelerates the growth of the Co clusters as discussed above and does not change significantly the rate of reduction. The same degree of reduction for the samples reduced for the same time either under hydrogen or both hydrogen and CO also suggests that the rate of metallic Co cluster formation is controlled by the diffusion of the cobalt species through the silica pore wall rather than by the reduction kinetics.

The intensities of the preedge peaks plotted in Figure 3 were obtained from the XANES spectra in Figure 1. In a hydrogen atmosphere, the metallic clusters interact more strongly with the surface because hydrogen is less likely to donate electrons to the Co cluster. Exposure to CO causes strong CO adsorption on the Co clusters weakening the interaction between the cluster and the pore wall surface, as discussed above. The clusters, thus, become more mobile at the surface and their nucleation rate increases until they reach the size/morphology/electronic state required to dissociate CO and initiate the growth of a carbon nanotube. Cobalt cluster growth ceases as the cobalt particles are covered with carbon, consistent with our previous findings that the Co—Co coordination number only increased during the first 30 min of exposure to CO.[8]

Along the lines of the scenario proposed above, the CO partial pressure should have a strong influence on the rate of cobalt nucleation on prereduced catalysts. Two XANES experiments were performed with Co-MCM-41 pretreated under identical conditions—heated to 500 °C and prereduced under flowing hydrogen for 30 min—and exposed to CO for 1 h at 2 and 6 atm, respectively. The XANES spectra recorded in situ during catalyst exposure to CO at 750 °C are shown in Figure 7. The variations of the intensities of the white line and of the preedge peak are plotted against the duration of the catalyst exposure to CO at 2 and 6 atm in Figure 8. Since the intensity of the preedge increases as the intensity of the white line decreases, it is likely that the variation of the intensity of the white line at these reaction conditions is reflective of the degree of cobalt
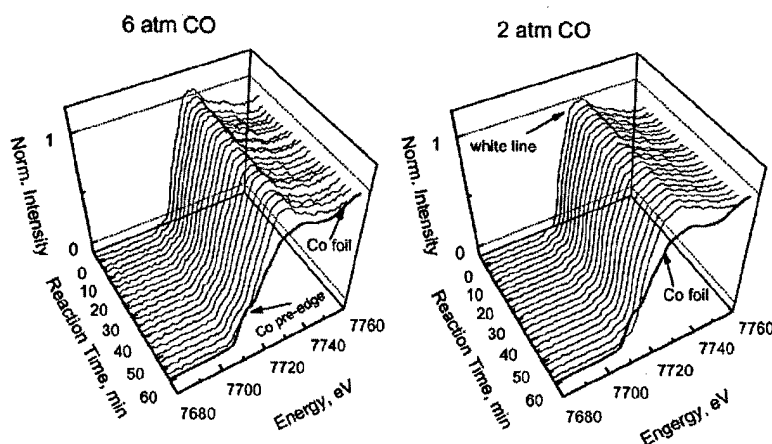

Figure 7. XANES spectra recorded during Co-MCM-41 exposure to CO at 750 °C and different pressures after identical pretreatment in hydrogen at 500 °C for 30 min.
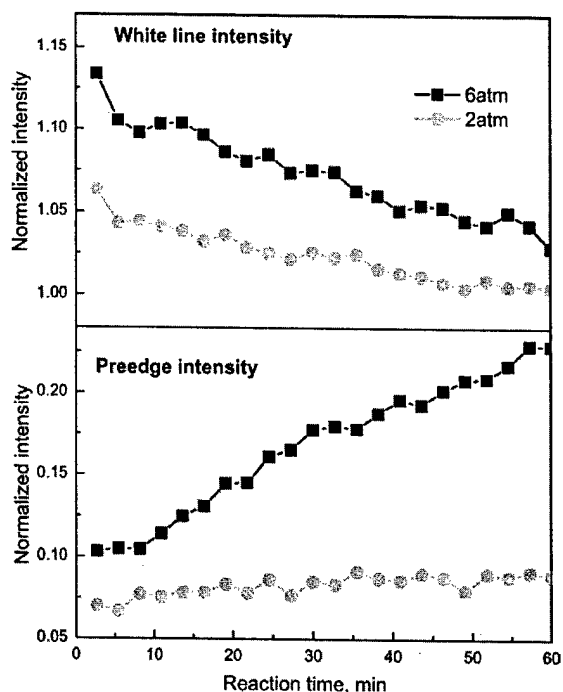
Mechanism of Cobalt Cluster Size Control

J. Phys. Chem. B, Vol. 108, No. 40, 2004 **15571**

Figure 8. Variation of the intensities of the preedge peak and of the white line with the time of exposure to CO at 2 and 6 atm at 750 °C after identical pretreatments.

reduction to metal. The intensity of the white line decreased at approximately the same rate for the two pressures, suggesting the rate of cobalt reduction by CO is not highly sensitive to the CO pressure. The intensity of the preedge peak of the sample exposed 1 h to CO at 6 atm and 750 °C, however, increased at a significantly higher rate than that of the sample reacted for 1 h under 2 atm CO at the same temperature. Since both of the catalysts were exposed to identical pretreatment conditions, and the cobalt reduction rates suggested by the white line intensities are essentially identical, the concentration of the reduced cobalt species at the end of these experiments should be similar for the two samples. Therefore, the significant difference between the rates at which the intensity of the preedge peak increased suggests this spectral feature correlates rather with the size of the cobalt clusters, being an indication of the rate of cobalt nucleation and cluster growth. Indeed, the Co—Co coordination numbers determined for the samples pretreated under identical conditions and reacted with CO for 1 h at 750 °C at 2 and 6 atm were near zero and 4.6, respectively.

Since in a related X-ray diffraction investigation performed on Co-MCM-41 catalysts formation of cobalt silicate was observed only after calcination in oxygen at 900 °C, stabilization of cobalt in an oxidized silicate-like surface compound, similar to the cobalt molybdate-like surface layer in the Co—Mo catalysts, can be ruled out. The stabilization mechanism likely consists of the incorporation of the Co^{2+} ions in the silica rings forming the MCM-41 structure. The variation of the stability of these rings with ring size, as a function of radius of curvature of the pore wall, is discussed in detail elsewhere.[7] This feature allows "engineering" of the Co cluster size and, potentially, of SWNT diameter.

Conclusion

The results presented here suggest that prereduction in hydrogen facilitates the removal of hydroxyl or oxygen from the Co-MCM-41. The oxygen vacancies created by hydrogen reduction allow Co to migrate to the surface and form small metal clusters strongly bound to the surface oxygen and exposed cations, but exposed to the gas phase. Bonding between these Co clusters and CO molecules weakens their interaction with the pore wall and increases their mobility allowing fast migration and formation of larger metallic clusters capable of dissociating CO and initiating the growth of SWNT. When the clusters become coated with carbon, however, their growth ceases. It could be that the minimum diameter of the SWNT that can be grown using a cobalt catalyst is limited by the size/morphology/ electronic structure of the Co cluster required for dissociating the CO molecules to initiate the growth of the nanotube. A potential way to overcome this limitation may be the use of a different carbon precursor, such as alcohols or olefins. However, we are already near the ultimate limit, which is controlled by the ring strain as the SWNT diameter decreases.

References and Notes

(1) Ajayan, P. M.; Zhou, O. Z. *Carbon Nanotubes* **2001**, *80*, 391.

(2) Journet, C.; Maser, W. K.; Bernier, P.; Loiseau, A.; Lamy de la Chapells, M.; Lefrant, S.; Deniard, P.; Lee, R.; Fischer, J. E. *Nature (London)* **1997**, *388*, 756.

(3) Nikolaev, P.; Bronikowski, M. J.; Bradley, R. K.; Rohmund, F.; Colbert, D. T.; Smith, K. A.; Smalley, R. E. *Chem. Phys. Lett.* **1999**, *313*, 91.

(4) Kitiyanan, B.; Alvarez, W. E.; Harwell, J. H.; Resasco, D. E. *Chem. Phys. Lett.* **2000**, *317*, 497.

(5) Resasco, D. E.; Alvarez, W. E.; Pompeo, F.; Balzano, L.; Herrera, J. E.; Kitiyanan, B.; Borgna, A. *J. Nanoparticle Res.* **2002**, *4*, 131.

(6) Ciuparu, D.; Chen, Y.; Lim, S.; Haller, G. L.; Pfefferle, L. *J. Phys. Chem. B* **2004**, *108*, 503.

(7) Lim, S.; Ciuparu, D.; Chen, Y.; Yang, Y.; Pfefferle, L.; Haller, G. L. *J. Phys. Chem. B* **2004**, ASAP DOI:10.1021/jp048881(+).

(8) Chen, Y.; Ciuparu, D.; Lim, S.; Yang, Y.; Haller, G.; Pfefferle, L. *J. Catal.* **2004**, *225*, 453.

(9) Alvarez, W. E.; Kitiyanan, B.; Borgna, A.; Resasco, D. E. *Carbon* **2001**, *39*, 547.

(10) Herrera, J. E.; Balzano, L.; Borgna, A.; Alvarez, W. E.; Resasco, D. E. *J. Catal.* **2001**, *204*, 129.

(11) Chen, Y.; Ciuparu, D.; Lim, S.; Yang, Y.; Haller, G.; Pfefferle, L. *J. Catal.* **2004**, *226*, 351.

(12) Lim, S.; Yang, Y.; Ciuparu, D.; Wang, C.; Chen, Y.; Pfefferle, L.; Haller, G. *Top. Catal.* **2004**, in press.

(13) Barrett, E. P.; Joyner, L. G.; Halenda, P. P. *J. Am. Chem. Soc.* **1951**, *73*, 373.

(14) Stern, E. A.; Newville, M.; Ravel, B.; Yacoby, Y.; Haskel, D. *Physica B* **1995**, *209*, 117.

(15) Ankudinov, A. L.; Ravel, B.; Rehr, J. J.; Conradson, S. D. *Phys. Rev. B* **1998**, *58*, 7565.

(16) Bart, J. C. J. *Adv. Catal.* **1986**, *34*, 203.

(17) Wong, J.; Lytle, F. W.; Messmer, R. P.; Maylotte, D. H. *Phys. Rev. B* **1984**, *30*, 5596.

(18) Feuston, B. P.; Higgins, J. B. *J. Phys. Chem.* **1994**, *98*, 4459.

(19) Frenkel, A. I.; Hills, C. W.; Nuzzo, R. G. *J. Phys. Chem. B* **2001**, *105*, 12689.

Synthesis, Characterization, and Stability of Fe−MCM-41 for Production of Carbon Nanotubes by Acetylene Pyrolysis

Placidus B. Amama, Sangyun Lim, Dragos Ciuparu, Yanhui Yang, Lisa Pfefferle, and Gary L. Haller*

Department of Chemical Engineering, Yale University, 9 Hillhouse Ave., New Haven, Connecticut 06520

Received: June 29, 2004; In Final Form: November 18, 2004

Fe-substituted MCM-41 molecular sieves with ca. 1, 2, and 3 wt % Fe were synthesized hydrothermally using different sources of colloidal silica (HiSil and Cab-O-Sil) and characterized by ICP, XRD, N_2 physisorption, UV−vis, EPR, TPR, and X-ray absorption. Catalysts synthesized from Cab-O-Sil showed higher structural order and stability than those from HiSil. The local environment of Fe in the mesoporous material as studied by UV−vis reveals the dominance of framework Fe in all the as-synthesized Fe−MCM-41 samples. Dislodgement of some Fe species to extraframework location occurs upon calcination, and this effect is more severe for Fe−MCM-41 (2 wt %) and Fe−MCM-41 (3 wt %), as confirmed by EPR and X-ray absorption. These materials have been used as catalytic templates for the production of carbon nanotubes (CNTs) by acetylene pyrolysis at atmospheric pressure. A relationship between the Fe loading in MCM-41 and the carbon species produced during this reaction has been established. Using our optimized conditions for this system, Fe−MCM-41 with ca. 2 wt % Fe showed the best results with particularly high selectivity for single-wall carbon nanotube (SWNT) production. This catalyst was selective for carbon nanotubes with a low amount of amorphous carbon for a narrow range of temperatures from 1073 to 1123 K. To account for the different selectivity of these catalysts for CNTs production, the local environment and chemical state of Fe in the used catalyst was further probed by X-band EPR.

1. Introduction

MCM-41 and related mesoporous molecular sieves of the M41S family are materials of great interest because of their remarkable physical properties such as large surface area (>1000 m^2/g) and pore volumes (>0.8 cm^3/g), very narrow pore size distribution, and the ease with which their surface can be functionalized.[1] Also, their uniform and tunable pore diameters make them well-adapted as good catalytic supports. Generally, pure silica MCM-41 has limited catalytic activity; active catalytic sites can be generated in MCM-41 by isomorphously substituting silicon with a metal.[2] Several studies have been dedicated to the investigation of transition-metal-substituted MCM-41 because of their wide range of applications in catalysis. Specifically, Co, Ni, and Fe-substituted MCM-41 are materials of interest to us because these metals are highly active and selective for the production of carbon nanotubes (CNTs).

In previous studies, this laboratory demonstrated the templated growth of SWNT from highly ordered Co-incorporated MCM-41 using the CO disproportionation reaction.[4,5] The use of mesoporous silica rather than a zeolitic material as a catalytic template for production of CNTs is gaining prominence because of the possibility of controlling the pore diameter independent of the chemical composition of the pore walls. This allows these parameters to be used independently to control the size of the metal particles incorporated in the mesopores from which the initiation of CNT growth is believed to occur. The metal particle plays an important role during CNT production and reports abound showing a direct correlation between the size of the metal nanoparticle and the eventual tube diameter.[5,6] Thus, the

ultimate goal of being able to control the diameter of CNTs would require a thorough understanding of the microstructure, stability, and chemical properties of the catalytic template.

In comparison to the other traditional metals (Co, Ni) used for CNTs synthesis, Fe has been reported by Hernadi et al.[7,8] and Dai et al.[9] to show the highest activity in the decomposition of acetylene. Because hydrocarbon gases are more common, the use of acetylene offers a means of scaling up production of CNTs. Acetylene is considered a good carbon source for single-wall carbon nanotubes (SWNT) production because it contains fewer number of carbon atoms per molecule and greater activity in comparison to other hydrocarbons such as benzene.[10] In reality, several reports[11−15] reveal that CNTs formed by the pyrolytic decomposition of acetylene over Fe catalysts are usually multiwalled carbon nanotubes (MWNT). This has been widely rationalized to be due to the high reactivity of acetylene. Parallel studies carried out hitherto involved the use of Fe supported on alumina or silica by either sol−gel,[13,16] adsorption precipitation,[17] or impregnation[18] techniques and have been used mostly in CVD[16] studies. So far, only the work of Duxiao and co-workers[12] has demonstrated the use of Fe-impregnated mesoporous molecular sieve as a catalytic template to produce CNTs via this method. In their study, the stability of the catalytic template and the state of the catalytically active component and the microstructure of the catalyst were not the focus of the work.

Herein, we present a comprehensive characterization of the catalyst carried out by various techniques such as XRD, N_2 physisorption, UV−vis, EPR, TPR, TEM, and X-ray absorption. This is the first study demonstrating the use of MCM-41 with Fe incorporated into the framework of MCM-41 and the first study of CNT growth on Fe catalyst focusing on thorough

---

characterization of the catalyst. In brief, this study is aimed at investigating the following features of Fe−MCM-41: (i) the effect of Fe amount on the structure and the local environment of Fe species before and after reaction, (ii) the effect of the source of colloidal silica used for the synthesis on the stability and the mesoporous structural integrity, (iii) the effect of Fe amount on the reactivity, and (iv) the relationship between the Fe loading and the selectivity for CNT production.

2. Experimental Section

Synthesis of Catalyst. Fe−MCM-41 was synthesized under hydrothermal conditions adapted from the recipe previously described for V-substituted MCM-41 by Lim and Haller[19] using cetyltrimethylammonium hydroxide (CTMAOH) as the template. CTMAOH was prepared by the ion-exchange of 20 wt % aqueous solution of $C_{19}H_{42}NBr$ (Aldrich) with equal molar exchange capacity of Amberjet 4400 (OH) ion-exchange resin (SIGMA Co.) under vigorous magnetic stirring for ~24 h. Silica sources were HiSil-915 from Pittsburgh Plate Glass (~90 wt % SiO_2 as well as 0.5 wt % $NaSO_4$), Cab-O-Sil (99.8%+ SiO_2) from Cabot Corporation, and tetramethylammonuim silicate (10 wt % SiO_2) from Aldrich. Typically, 2.5 g of the colloidal silica (HiSil or Cab-O-Sil) and 10.4 g of soluble silica (tetramethyl-ammonium silicate) were dissolved in 50 mL of deionized water and stirred vigorously for 30 min. This was followed by the dropwise addition of known amounts of 2 wt % $Fe(NO_3)_3 \cdot 9H_2O$ solution corresponding to 1, 2, and 3 wt % from a pipet to the resulting mixture under vigorous stirring. After 30 min, a small amount of antifoaming agent (Antifoam A, Sigma Chemical Co.) corresponding to 0.2 wt % of surfactant was added to the mixture to improve the reproducibility and remove excess foam. The anitifoaming agent is a silane polymer alkyl terminated by methoxy groups. This was followed by the addition of 28.8 g of CTMAOH and was allowed to mix for over 30 min under vigorous stirring. The pH was reduced to ~11 by the dropwise addition of acetic acid (Baker, 99.9%). The mixture was then transferred into a polypropylene bottle and autoclaved at 373 K for 6 days. The synthesis of Fe-free siliceous MCM-41 followed the same procedure without the addition of aqueous solution of $Fe(NO_3)_3 \cdot 9H_2O$. The final products obtained were recovered by filtration, washed with deionized water, and dried at ambient conditions for 24 h. The molar composition of the gel subjected to hydrothermal synthesis was as follows: 1.0 SiO_2:0.33 CTMAOH:xFe:yH_2O where x = 0.01, 0.02, and 0.03; y = 81−104.

The as-synthesized samples were calcined to remove the organic surfactants from the pores of MCM-41. Calcination was performed by heating from room temperature to 813 K over 20 h in a He stream (60 cm^3/g-min) and was maintained at this temperature for 1 h in flowing He and 6 h in flowing air (40 cm^3/g-min). All investigations have been limited to calcined samples except those involving diffuse reflectance UV−vis spectroscopy where the local environment of Fe in the as-synthesized and calcined samples have been compared.

Characterization of Catalyst. Except where stated otherwise, the catalysts synthesized from HiSil were used for all investigations.

Elemental Analysis. The final Fe content in each sample was determined by ICP measurements (Galbraith Laboratories, Inc.) because the synthesis process can result in some loss of Fe and silica in the byproduct.

X-ray Diffraction (XRD) Studies. XRD measurements were carried out using a Shimadzu X-ray diffractometer (Cu Kα, λ = 0.154 nm, 40 kV, 30 mA) to confirm the long-range order of the characteristic hexagonal pore structure of the synthesized catalysts after calcination. The d_{100} values were obtained using the Bragg diffraction equation. The distance between the pore centers of the hexagonal structure is calculated from the relation $a_0 = 2d_{100}/\sqrt{3}$.

N_2 Physisorption. N_2 adsorption−desorption studies were carried out at 77 K with a static volumetric instrument Autosorb-1C (Quantachrome) to examine the mesoporous properties of the catalysts. Samples were pretreated by outgassing at 373 K for 30 min and at 473 K for more than 30 min to a residual pressure below 1×10^{-4} Torr. The pore size distribution (PSD) was evaluated from the desorption isotherms using the BJH method.[20] The results of XRD and N_2 physisorption have been used in estimating the wall thickness; it was assumed to be equal to the difference between the spacing of pore centers and the BJH pore diameter.

UV−Vis. The diffuse reflectance UV−vis spectra were recorded on a Hewlett-Packard 8452A diode array spectrometer equipped with a Harrick praying mantis. Samples were hand pressed in the sample holder to obtain a thick wafer and the spectra were collected in a range of 200−800 nm. The reference samples (Fe_2O_3 and $FePO_4$) were diluted to 1 wt % with siliceous MCM-41 before measurement.

Electron Paramagnetic Resonance (EPR). X-band EPR investigations were carried out using a Varian E-9 spectrometer (9.28 GHz/4.5 T) equipped with a TE_{102} cavity and a helium flow cryostat (Oxford Instruments) at 60 K and at room temperature (298 K). Details of the experimental procedure has been described by Lakshmi et al.[21]

X-ray Absorption. Fe K-edge XANES spectra were recorded at beam line X23A2 with Si(111) as the monochromator crystal at the National Synchrotron Light Source at Brookhaven National Laboratory. The intensity of the incident beams (I_o) was determined using a 30-cm-long ion chamber filled with pure N_2. Data were collected in transmission mode by scanning from 200 below to 1600 eV beyond the Fe K edge. Samples were pressed to self-supporting wafers and placed in a stainless steel cell for measurement. A detailed description of the procedure has been reported in ref 5.

Temperature-Programmed Reduction (TPR). The reducibility and the stability of Fe−MCM-41 samples were investigated by TPR using a TCD detector of a gas chromatograph (6890 plus, Agilent). Typically, ~200 mg of the catalyst was put into the quartz cell. Prior to each run, the sample cell was purged with ultra zero grade air while the temperature was increased from room temperature to 773 K at 5 K/min. After 1 h at this temperature, the catalyst was cooled to room temperature in flowing air. This pretreatment procedure produces a clean catalytic surface without altering the surface and the structure before the run is commenced. After this pretreatment, the gas flow was switched to 5% H_2 in Ar balance and the baseline was monitored until it became stable. The sample cell was then heated at 5 K/min and held for 1 h at 1173 K to ensure complete Fe reduction. An acetone trap was installed between the sample cell and the TCD to condense water produced by sample reduction.

Synthesis of CNTs. The production of CNTs by acetylene pyrolysis over Fe−MCM-41 was carried out at atmospheric pressure in a specially designed flow reactor (quartz tube of inner diameter 6.5 cm and length of 44 cm). The reactor was separated by a porous frit to enable the introduction of gas feeds through one end where the catalyst was loaded and flowed out of the reactor through the frit. A thermocouple was placed at the opposite end of the reactor, close to the catalyst bed, to

Synthesis and Characterization of Fe−MCM-41

J. Phys. Chem. B, Vol. 109, No. 7, 2005 **2647**

TABLE 1: Textural Properties of the Various Catalysts Synthesized from HiSil and Cab-O-Sil

colloidal silica	Fe content in synthesis gel (wt %)	Fe content in sample by ICP (wt %)	pore diameter (Å)	pore volume (cc/g)	S_{BET} (m²/g)	d_{100} (Å)	pore wall thickness (Å)	color of calcined sample
HiSil	0		26.89	1.069	1218	35.50	14.10	white
HiSil	1.0	0.99	28.77	0.94	1073	38.50	15.68	white
HiSil	2.0	1.59	29.30	1.01	1144	39.92	16.79	pale yellow
HiSil-R[a]	2.0		25.08	0.24	304			black
HiSil-O[b]	2.0		26.23	1.167	1089			pale yellow
HiSil	3.0	2.25	28.60	0.44	514			brown
Cab-O-Sil	0		27.33	0.935	1045	38.29	16.88	white
Cab-O-Sil	1.0	0.99	29.52	0.813	898	39.61	16.24	white
Cab-O-Sil	2.0	1.78	29.38	0.87	969	41.58	18.63	pale yellow
Cab-O-Sil-R[a]	2.0		27.58	0.682	882			black
Cab-O-Sil-O[b]	2.0		26.84	0.926	990			pale yellow
Cab-O-Sil	3.0	2.37	29.37	0.80	909	42.05	19.19	brown

[a] After reaction. [b] After carbon removal (TPO).

determine the exact temperature of the catalyst. The reactor was placed horizontally in a tubular electric furnace (length = 90 cm, Omega), equipped with a temperature controller. In a typical run, 0.5 g of the calcined catalyst was put into the reactor, heated in He flow (200 cm³/g-min) from room temperature to 1073 K at a heating rate of 10 K/min. Subsequently, C_2H_2/N_2 mixture (99% N_2 and 1% C_2H_2) at a flow rate of 200 cm³/g-min was fed into the reactor and maintained under these conditions for 1 h. The flow rate of the gases was controlled using Omega mass flow controllers. The reactor was then allowed to cool to room temperature in flowing He at the conclusion of each run.

Characterization of CNTs. *Raman Spectroscopy.* Raman spectra were obtained using a LabRam instrument from Jobin Yvon Horiba equipped with an Olympus confocal microscope using an excitation wavelength of 532 nm.

High-Resolution Transmission Electron Microscopy (HR-TEM). The TEM micrographs were recorded on a Philips Tecnai F20 TEM instrument equipped with a field emission gun and accelerating voltages of up to 200 kV. The point resolution and the line resolution were 0.24 and 0.12 nm, respectively, at a focal length of 1.7 mm. Samples were prepared by ultrasonicating ∼1 mg of the final product in 10 mL of ethanol (ACS/USP grade). A drop of this suspension was then put on a lacey carbon coated copper TEM grid.

3. Results and Discussion

Characterization of Catalyst. A summary of the physical properties of the catalysts used in this study is presented in Table 1. The results of ICP measurement as shown in Table 1 reveal that Fe is quantitatively incorporated at low concentration in synthesis gel, but the amount incorporated decreases as the concentration of Fe in the synthesis gel increases. Also, catalysts containing ca. 2 and 3 wt % Fe synthesized from Cab-O-Sil retained more Fe than those from HiSil. The high purity of Cab-O-Sil (>99.8%) may be responsible for this observation because HiSil contains impurities, which may compete for different sites with incorporated Fe in the silica.

In this study, comparisons of the mesoporous structural integrity and stability of the catalytic templates containing ca. 1, 2, and 3 wt % Fe synthesized from HiSil and Cab-O-Sil have been carried out. On the basis of the ICP results presented in Table 1, catalysts containing ca. 2 wt % Fe synthesized from HiSil and Cab-O-Sil are actually a 1.59 wt % Fe (HiSil) to a 1.78 wt % Fe (Cab-O-Sil) and the 3 wt % is actually a 2.25 wt % Fe (HiSil) to a 2.37 wt % Fe (Cab-O-Sil).

XRD pattern of siliceous MCM-41 and Fe-containing MCM-41 (Fe = 1, 2, 3 wt %) synthesized using HiSil and Cab-O-Sil
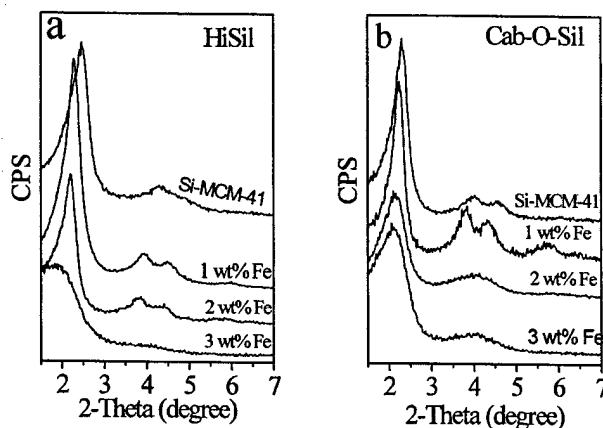

Figure 1. XRD patterns of calcined siliceous MCM-41 and Fe−MCM-41 containing different Fe loadings synthesized using HiSil (a) and Cab-O-Sil (b).

silica are shown in Figure 1a and 1b, respectively. The XRD patterns of all HiSil and Cab-O-Sil samples are consistent with that reported for MCM-41 by Beck et al.[1] They are characterized by a strong, narrow, low-angle reflection at about $2\theta = 2$ ascribed to the (100) reflection and a series of weak peaks in the range of $2\theta = 3-8°$ as shown in Figure 1. These reflections arise from the ordered hexagonal array of parallel mesopores. Higher reflections corresponding to (110), (200), and (210) were well resolved for Fe−MCM-41 (1 wt %) illustrating the high regularity of the structure of this catalyst in comparison to the other catalysts. Upon Fe incorporation, the main diffraction peak {(100) reflection} is shifted to lower 2θ values indicating an increase in the lattice parameters (*d*-spacing and a_0 values). The corresponding lattice parameters of all the catalysts are summarized in Table 1. Given that all template synthesis parameters were kept constant, the increase in the lattice parameter could be considered as a proof of the isomorphous substitution of Si^{4+} ions with those of Fe^{3+} in the framework. This is because the ionic radii of Fe^{3+} (0.65 Å) are much larger than Si^{4+} (0.26 Å). Consequently, the Fe−O bond length is greater than that of Si−O. The absence of a well-defined (100) reflection for Fe−MCM-41 (3 wt %), especially for samples synthesized from HiSil, shows that there is a significant decrease in the structural regularity of the sample upon the introduction of ca. 3 wt % Fe. No peaks were observed in the high-angle range of all samples suggesting the absence of any crystalline phases. This, however, does not rule out the existence of iron species at the surface because of the limitation of XRD to detect very small particles at low concentrations. The brown color of Fe−MCM-
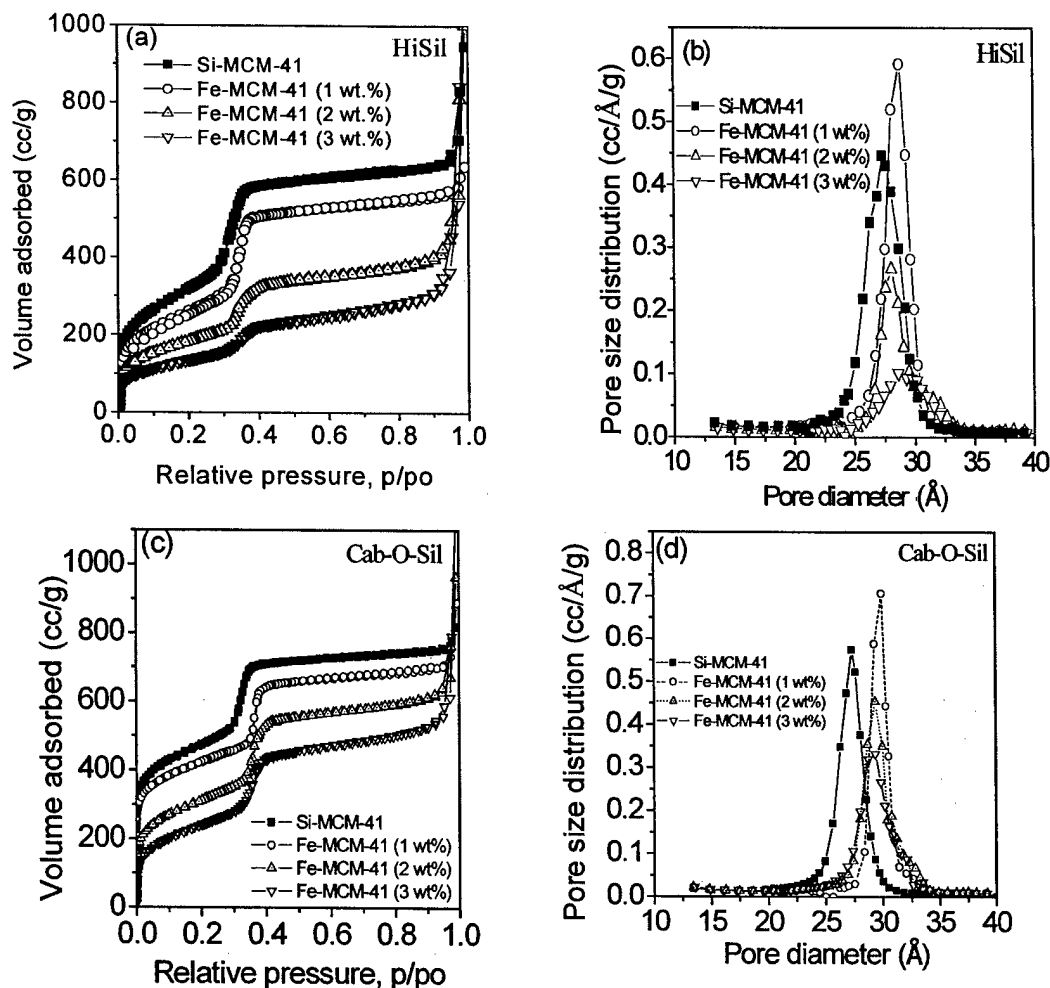
2648 *J. Phys. Chem. B, Vol. 109, No. 7, 2005*

Amama et al.

Figure 2. N_2 adsorption—desorption isotherms of Si—MCM-41 and Fe—MCM-41 (1, 2, and 3 wt %) and their respective pore size distributions synthesized from HiSil (a) and (b) and Cab-O-Sil (c) and (d).

41 (3 wt %), however, is suggestive of the presence of iron oxides.[22,23]

The results of both XRD and N_2 physisorption are complementary with respect to probing the structural integrity of MCM-41. XRD can be used to characterize the two-dimensional hexagonal structure of the catalyst while N_2 physisorption gives information about the extent of the uniformity of the mesopores. While XRD characterizes only the ordered portion of the material, N_2 physisorption gives a volume average measure of order and thus gives a complementary picture of the overall structure of the material. The N_2 adsorption—desorption isotherm and PSD of siliceous MCM-41 and Fe—MCM-41 (1, 2, and 3 wt %) synthesized from HiSil are presented in Figure 2a and 2b, while those synthesized from Cab-O-Sil are shown in Figure 2c and 2d. The isotherms of all samples show a sharp inflection step at p/p_0 of ~0.3—0.4, characteristic of capillary condensation of uniform mesoporous materials.[24] As shown in Table 1, all samples (except Fe—MCM-41, 3 wt %) exhibited relatively high surface areas and pore volumes. The mesopore diameter observed for all samples containing Fe was about 29 Å and was unaffected by the introduction of more Fe^{3+} cations. Siliceous MCM-41 showed pore diameters (~27 Å) somewhat lower than those of Fe—MCM-41. The pore volume does not seem to be affected significantly by the incorporation of Fe. Generally, the pore wall thickness of MCM-41 increases with the Fe loading (Table 1) and this may be due to the longer Fe—O bond length in comparison to that of Si—O. Samples synthesized

from HiSil showed greater increase in wall thickness upon the incorporation of higher Fe loadings.

The isotherm corresponding to $p/p_0 < 0.3$ represents the monolayer adsorption of N_2 on the walls of the mesopore, while that with $p/p_0 > 0.4$ represents the multilayer adsorption on the outer surface of the particles. The point at which the inflection begins is related to the capillary condensation within the uniform mesopores and their diameter. There was a slight shift in the inflection step toward higher p/p_0 upon the introduction of Fe. This signifies an increase in pore size, in consonance with XRD results. There was no noticeable shift in the inflection step of Fe—MCM-41 upon incorporation of more Fe^{3+} cations. A hysteresis loop was observed for Fe—MCM-41 (3 wt %) at $p/p_0 > 0.9$, which is likely due to the interparticle spaces.

As shown in previous studies,[4,25] the slope or the steepness of the capillary condensation step and the full width at half-maximum (fwhm) of the PSD curve can be used as structural indexes to assess the mesoporous structural integrity and stability of these catalysts. As shown in Figure 3a, the value of the slope increased upon the initial introduction of Fe (1 wt %) into the silica framework because of the knitting effect in consonance with previous observation.[4] Further increase in the amount of Fe (> 1 wt %) resulted in a decrease in the value of slope, which could be attributed to the oversaturation of Fe^{3+} in the pore walls of MCM-41. The effect of Fe loading on the fwhm of the PSD curve is shown in Figure 3b. There is a general decrease in the fwhm of the PSD curve upon the incorporation of 1 wt
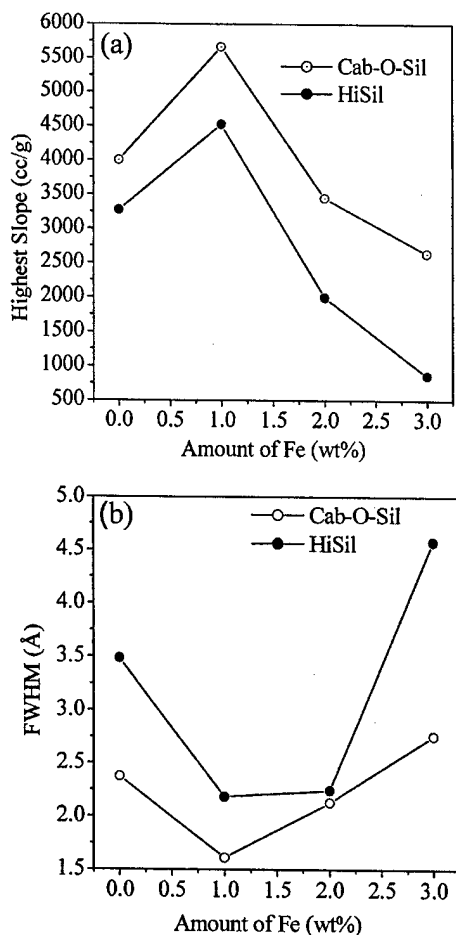
Synthesis and Characterization of Fe—MCM-41

J. Phys. Chem. B, Vol. 109, No. 7, 2005 **2649**

Figure 3. Effect of Fe amount on the slope of the capillary condensation step (a) and the fwhm (b) derived from Figure 2.

Figure 4. DR UV—vis spectra of reference compounds (a) and as-synthesized and calcined Fe—MCM-41 containing 1 wt % Fe (b), 2 wt % Fe (c), and 3 wt % Fe (d).

% of Fe. However, as the Fe amount in MCM-41 is increased beyond 1 wt %, the fwhm increases suggesting a decrease in the structural order. The behaviors of the fwhm of the PSD curves and of the slopes of the capillary condensation steps upon incorporation of different concentrations of Fe into MCM-41 are in consonance. We therefore conclude as follows: (i) there is a significant structural improvement upon the incorporation of 1 wt % of Fe into MCM-41, but a decrease in the structural integrity is observed upon incorporation of higher Fe concentrations, (ii) siliceous MCM-41 and Fe—MCM-41 synthesized from Cab-O-Sil have higher structural order in comparison to those synthesized from HiSil, as evidenced by their higher values for capillary condensation slopes and lower fwhm of the PSD curves. The specific reason for this behavior is not well understood, but it is assumed that the type and the amount of impurities present in these colloidal silica and their synthesis routes may rationalize this observation.

The UV—vis diffuse reflectance spectra in the wavelength range of 200—800 nm of Fe—MCM-41 (1, 2, and 3 wt % Fe) and reference materials of Fe^{3+} in different environments (FePO$_4$ and Fe$_2$O$_3$) are shown in Figure 4. Fe^{3+} in FePO$_4$ and Fe$_2$O$_3$ exist in tetrahedral and octahedral coordination, respectively.[26,27] As shown in Figure 4a, isolated tetrahedral coordination of Fe^{3+} ions are characterized by a significant absorption in the wavelength range of 200—330 nm with a distinct peak at ~260 nm. On the other hand, Fe species having octahedral coordination exhibit a broad absorption band around 320—640 nm with an absorption maximum ~500 nm.
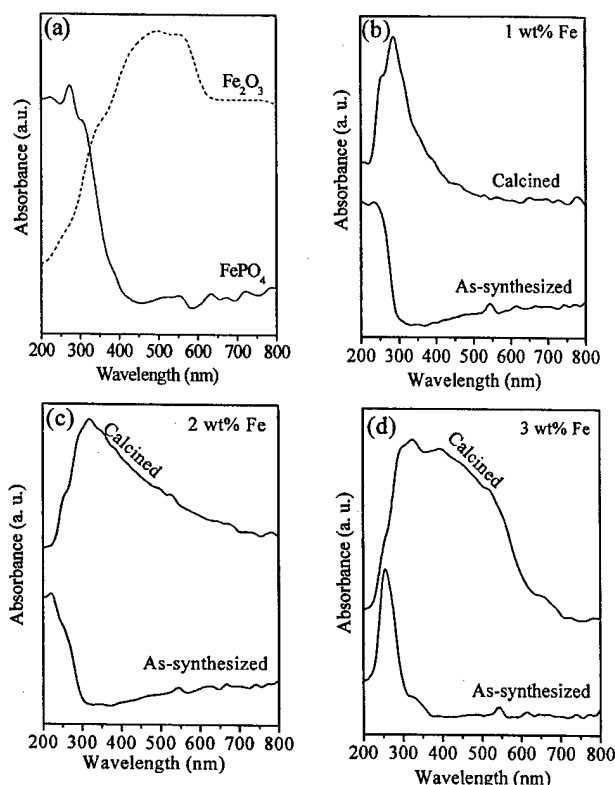
The absorption at 260 nm represents the oxygen ligand to metal charge-transfer transitions associated with Fe^{3+} species in isolated tetrahedrally coordinated sites.[22,23,26—29] All the as-synthesized samples were white and showed significant absorption at 260 nm suggesting the dominance of framework incorporated Fe in the samples. Upon calcination, Fe—MCM-41 (1 wt %) retains its white color while Fe—MCM-41 (2 wt %) and Fe—MCM-41 (3 wt %) became pale yellow and brown, respectively (Table 1). As observed in Figure 4b, calcined Fe—MCM-41 (1 wt % Fe) shows an absorption peak having a maximum at 300 nm and a shoulder at 260 nm, characteristic of framework or tetrahedrally coordinated Fe. For this catalyst, most Fe seems to remain incorporated into the silica framework forming Fe—O—Si bonds. The absence of significant absorption beyond 320 nm is indicative of the absence of substantial amount of extraframework Fe confirming that most of the Fe is incorporated in the pore wall. In contrast, broadening of the absorption band to higher wavelength for calcined Fe—MCM-41 containing ca. 2 and 3 wt % Fe is observed (Figure 4c and 4d). This is suggestive of the presence of Fe^{3+} species in octahedral environment in these catalysts or of the formation of iron oxide clusters because, as shown in Figure 4a, contribution from iron oxide could also result in the broadening of the UV—vis spectra of Fe—MCM-41. The existence of extraframework, or bulk iron oxide, is usually indicated by an off-white or brown color in zeolitic[22] or MCM-41[23] catalysts. The respective pale yellow and brown colors observed in Fe—MCM-41 (2 wt %) and Fe—MCM-41 (3 wt %) upon calcinations could be due to the migration of Fe species from the framework. These Fe species may exist as aggregated oxidic nanoclusters in extraframework environment. Generally, there is a shift of the absorption band to longer wavelength with increasing Fe loading. Even though calcination provokes the migration of Fe
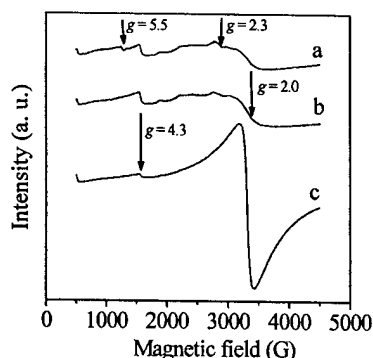
Figure 5. EPR spectra of Fe−MCM-41 containing 1 wt % Fe (a), 2 wt % Fe (b), and 3 wt % Fe (c) recorded at room temperature (298 K).
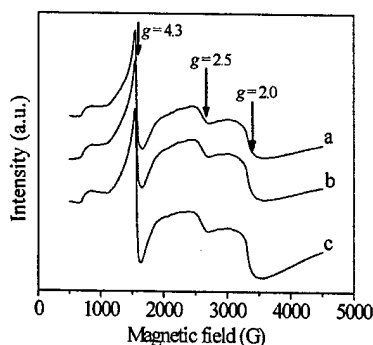

Figure 6. EPR spectra of Fe−MCM-41 containing 1 wt % Fe (a), 2 wt % Fe (b), and 3 wt % Fe (c) recorded at 60 K.

species from the framework of calcined Fe−MCM-41 (2 and 3 wt % Fe), the UV−vis spectra (Figure 4) gives evidence for the presence of framework Fe in these catalysts as evidenced by an absorption shoulder ∼260 nm. The migration of Fe from the framework of Fe-silicate upon the alkyl template removal during calcination in air has been reported.[27,30]

Further characterization of the local environment of Fe has been carried out by EPR spectroscopy at room temperature (298 K) and at 60 K as presented in Figures 5 and 6, respectively. EPR is a highly sensitive tool for probing the local symmetry of Fe because of its paramagnetic nature in the low-spin and high-spin electronic configurations.[31] The interpretation of EPR data of Fe states in zeolites or MCM-41 is still an issue of controversy because the presence of surrounding silanol groups and H_2O molecules tends to interfere with the signal.[31] The unambiguous interpretation of EPR data of Fe−MCM-41 can be accomplished if combined with results of other spectroscopic techniques such as UV−vis, Mössbauer, or X-ray absorption. On the basis of most studies carried out on Fe-containing zeolites,[31] HMS[29] and MCM-41,[23,28,32] the signal corresponding to $g = 4.3$ is considered as evidence of framework Fe and is characteristic of isolated Fe^{3+} paramagnetic cations in a strong rhombic distorted tetrahedral coordination; the signal at $g = 2$ has been assigned to extraframework Fe^{3+} or Fe^{3+} species in octahedral coordination. As observed by Goldfarb et al.,[31] this signal at $g = 2$ could also be partly due to Fe^{3+} in tetrahedral site even though Fe^{3+} in oxidic clusters is known to give a signal at $g = 2$. The signal at $g = 2.3−2.5$ is ascribed to iron clusters or iron oxide species.[29]

The EPR spectra of Fe−MCM-41 containing different loadings of Fe recorded at room temperature (Figure 5) exhibits a weak signal at $g = 4.3$ ascribed to Fe^{3+} in distorted tetrahedral coordination and a broad signal at $g = 2.0$ indicating the presence of either framework or extraframework Fe^{3+}. A weak

signal is also observed at $g = 5.5$ for catalysts containing 1 wt % Fe. This signal is assigned to Fe^{3+} in less distorted tetrahedral sites. The fact that only Fe−MCM-41 (1 wt %) shows this signal confirms the incorporation Fe^{3+} species in very stable sites in this sample. The intensity of the $g = 4.3$ signal decreases with increasing Fe loading suggesting that the amount of Fe^{3+} in tetrahedral sites decreases with increasing Fe loading. Also, there is a conspicuous increase in the line intensity of the $g = 2$ signal with increasing Fe loading which indicates an increase in the Fe amount in octahedral coordination. These results are consistent with those of UV−vis spectroscopy.

Conversely, the spectra of Fe−MCM-41 recorded at 60 K showed a strong signal at $g = 4.3$ and a broad signal at $g = 2.0$ (Figure 6). The line intensity of the $g = 4.3$ signal increases slightly with Fe amount while a more pronounced increase was observed for the $g = 2.0$ signal. The behavior of the $g = 2.0$ signal is similar to that recorded at room temperature. The signal observed at $g = 4.3$ or higher g values is temperature dependent and the intensity generally decreases with increasing temperature and tends to disappear at room temperature because of the faster spin relaxation.[31] In a qualitative sense, the presence of an intense $g = 4.3$ signals for all samples is an indication that all these catalysts have Fe^{3+} in distorted tetrahedral sites.

In consonance with results of UV−vis, it can be concluded that despite the dislodgement of Fe species from the framework as a result of calcination, framework Fe species still exist in a relatively high amount in both Fe−MCM-41 (2 wt %) and Fe−MCM-41 (3 wt %). The signal attributed to the iron oxide species occurs at a g value range of 2.2−2.5. For spectra recorded at room temperature, this signal is observed at $g = 2.3$ but at lower temperature (60 K) it is observed at $g = 2.5$. The presence of a well-defined signal at $g = 2.5$ signifies the presence of iron oxide species in all the catalysts regardless of the Fe loading. The line intensities of this signal for catalysts containing ca. 1, 2, and 3 wt % Fe were 40, 42, and 49, respectively. This suggests that there is a saturation of Fe cations in the pore walls and the surpluses form extraframework species at the surface. This confirms the increase in the amount of iron oxide with Fe loading as qualitatively indicated by the colors of the samples.

The coordination geometry of Fe in these catalysts was also characterized by X-ray absorption spectroscopy. The preedge feature of Fe in X-ray absorption near-edge structure (XANES) spectra is very sensitive to the local coordination status. The position, intensity, and shape of the preedge peaks observed are related to the local environment of Fe species and its electronic structure. The normalized near-edge region of XANES spectra of Fe−MCM-41 containing various Fe loading and Fe_2O_3 is shown in Figure 7a. The enlarged preedge region of the catalysts is shown in Figure 7b. Fe^{3+} in tetrahedral coordination is characterized by a single well-defined preedge peak, attributed to the 1s→3d dipolar transition (Figure 7a).[26,27] This transition is forbidden for octahedral coordination, but is usually present, albeit of low intensity, for distorted octahedral coordination as confirmed by the relative low intensity of the preedge peak of Fe_2O_3. The intensity of the preedge feature is related to the coordination number of the transitional metal. As the intensity decreases, there is a change in the coordination environment of the metal from tetrahedral → distorted tetrahedral → pyramidal → distorted octahedral → octahedral. On the basis of the preedge features and their corresponding intensities observed for these catalysts, it is obvious that Fe^{3+} in Fe−MCM-41 (1 wt %) exists mainly in tetrahedral environment, evidenced by the high intensity. The intensity decreases
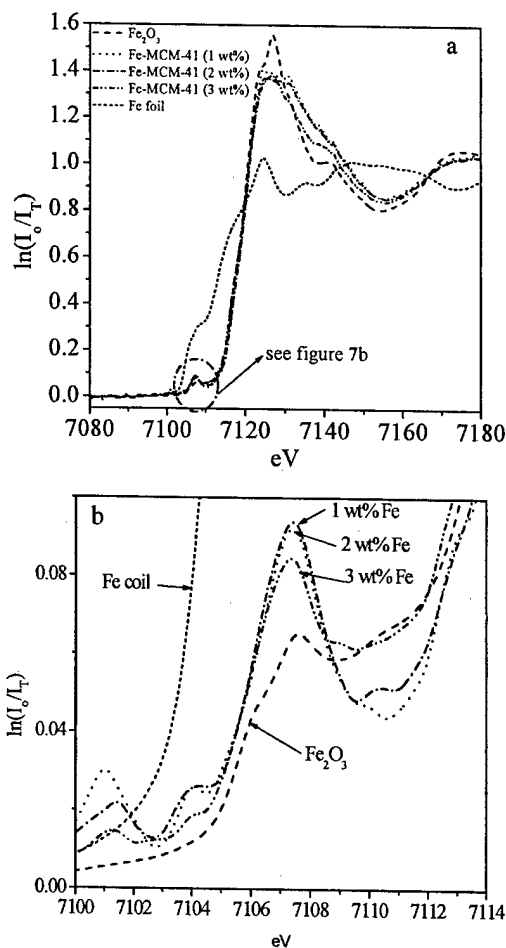
Figure 7. Fe K-edge XANES spectra for Fe—MCM-41 containing different Fe loading (a) and their enlarged preedge features (b).

Figure 8. TPR profiles of Fe—MCM-41 containing 1 wt % Fe (a), 2 wt % Fe (b), and 3 wt % Fe (c).

slightly for catalysts containing 2 wt % Fe suggesting the gradual change from tetrahedral to distorted coordination by some Fe species. However, catalysts containing 3 wt % Fe showed a preedge peak of low intensity suggesting the dominance of distorted and octahedrally coordinated Fe species resulting from surface Fe oxide species. The decrease in the preedge peak intensities with increasing the Fe loading observed in these catalysts may be rationalized by Laporte law. As explained by this law, the $A_{1g} \rightarrow T_{2g}$ and $A_{1g} \rightarrow E_g$ transitions are symmetrically forbidden in the octahedrally coordinated Fe^{3+} species, even though they are allowed for distorted octahedral symmetry, while the $A_1 \rightarrow T_2$ transition is allowed for Fe^{3+} species in tetrahedral sites. It is evident from these results that the fraction of Fe^{3+} species in tetrahedral coordination decreases with increasing Fe loading. This conclusion is consistent with the results of EPR and UV—vis.

TPR has been employed to investigate the reduction characteristics of Fe. The TPR profiles of Fe—MCM-41 containing different loadings of Fe are shown in Figure 8. The main feature of the TPR profiles of Fe—MCM-41 (1 wt %) and Fe—MCM-41 (2 wt %) is a distinct reduction peak with maximum at 675 and 653 K, respectively, while that of Fe—MCM-41 (3 wt %) shows three defined peaks in the temperature range of 600—850 K. The Fe—MCM-41 (3 wt %) has a reduction rate similar to Fe—MCM-41 (2 wt %) evidenced by their similar reduction peak maxima at 653 K. This suggests a similarity in the local environment of the Fe^{3+} species present in these catalysts. The reduction temperature of Fe—MCM-41 (1 wt %) is slightly
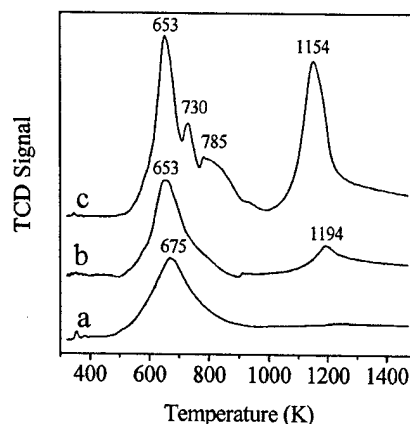
higher than Fe—MCM-41 containing ca. 2 and 3 wt % Fe. This is not surprising because more framework Fe species exist in stable tetrahedral sites in Fe—MCM-41 (1 wt %) than in the other samples, as confirmed by spectroscopic data. As observed in the TPR profile of Fe/SiO₂ with high Fe loading (2.9 wt %),[33] the three reduction peaks we observed in the profile of Fe—MCM-41 (3 wt %) can also be accounted for by the three steps of iron oxide reduction: $Fe_2O_3 \rightarrow Fe_3O_4 \rightarrow FeO \rightarrow Fe$. A second peak is also observed at higher reduction temperature (> 1000 K), and its intensity increased with the Fe loading. This peak is not visible in Fe—MCM-41 (1 wt %) because of the scale used. As shown by the TPR profiles of reference compounds (Fe_2O_3 and Fe_3O_4),[34] the complete reduction of Fe^{3+} and Fe^{2+} is generally completed at temperatures lower than ~973 K. This suggests that the second peak observed in the TPR profiles of our catalysts is not associated with any of the reduction steps of Fe. High-temperature peaks of this nature have been observed in the TPR profiles of Co—MCM-41 performed in our laboratory and have been attributed to the reduction of cobalt silicate formed during high-temperature treatment.[35] It is therefore assumed here that the reduction of Fe-silicate produced during the course of increasing the temperature accounts for the high-temperature reduction peak observed in these profiles.

Characterization of CNTs. The products obtained from the pyrolytic decomposition of acetylene over these catalysts have been characterized by Raman spectroscopy, thermogravimetry, and TEM. A typical Raman spectrum of CNTs is characterized by a D-band, G-band, and in some cases a radial breathing mode (RBM). The D-band is associated with the amount of disordered carbon and occurs in the 1200—1400 cm⁻¹ part of the spectrum. The G-band reveals the intense tangential modes of CNTs and the good arrangement of the hexagonal lattice of graphite, which occurs in the high-frequency region of 1500—1600 cm⁻¹. The RBM usually occurring in the low-frequency region (100—250 cm⁻¹) is generally considered as a special signature of SWNT. The frequencies of the RBM are inversely proportional to the nanotube diameters. The carbon loading in the product was determined gravimetrically by air oxidation under a programmed temperature between 373 and 1173 K at 10 K/min.

Because of the high reactivity of acetylene, previous investigators[36] have shown that a narrower range of operating conditions exists for selective production of SWNT when compared to the CO disproportionation process. Preliminary studies using Fe—MCM-41 (2 wt % Fe) were carried out to determine the optimal temperatures, reaction times, and reactant flow rates. In general, we find that for a 60-min growth run using a reactant flow rate of 200 mL/g-min at 973 K, few

2652 *J. Phys. Chem. B, Vol. 109, No. 7, 2005*

Amama et al.

TABLE 2: Summary of the Carbon Yields and the Carbon Species Obtained from the Reaction Catalyzed by the Various Catalysts Synthesized from Different Colloidal Silica HiSil and [Cab-O-Sil]

catalyst	Fe content in synthesis gel (wt %)	carbon yields[b] (wt %)	carbon species[a]
Si-MCM-41	0	8.49 [7.23][c]	amorphous carbon
Fe-MCM-41	1.0	9.70 [9.17]	amorphous carbon graphite
Fe-MCM-41	2.0	10.55 [9.84]	SWNT MWNT graphite amorphous carbon
Fe-MCM-41	3.0	5.36 [7.23]	MWNT graphite amorphous carbon

[a] On the basis of HR-TEM studies. [b] Determined by gravimetric analysis. [c] Values in brackets are for samples synthesized from Cab-O-Sil.

SWNTs are produced. However, the yield of SWNTs increased for samples synthesized at 1073 K and as the temperature is increased further, MWNT becomes predominant.

Studies of the effect of Fe amount on the production of CNTs were carried out at 1073 K using a C_2H_2/N_2 flow rate of 200 cm³/g-min for 60 min, the optimal experimental conditions for high selectivity of CNTs during acetylene decomposition over Fe–MCM-41. Total carbon yields measured by thermogravimetry is expressed in terms of weight percent (wt %) and are given in Table 2. An increase in carbon yield was observed for catalysts containing 1 and 2 wt % of Fe. Catalysts containing 3 wt % of Fe showed slightly lower activity for carbon production as evidenced by their lower carbon yields of ∼5−7 wt %. Indiscriminate production of carbon was observed even in the absence of a metal catalyst evidenced by the high carbon yield (∼8 wt %) obtained for reactions carried out over Fe-free siliceous MCM-41. This may be attributed to the self-pyrolysis of acetylene at high temperature to form high deposits of undesired carbonaceous material, such as amorphous carbon. Siliceous MCM-41 synthesized from HiSil showed slightly higher activity toward carbon production than those from Cab-O-Sil. This behavior was also observed for Fe–MCM-41 samples except those containing 3 wt % Fe. The presence of some metal impurities in HiSil could be responsible for the higher reactivity associated with catalysts synthesized from HiSil.

Despite the high carbon yields observed in the products of reactions catalyzed by siliceous MCM-41, Raman studies revealed the absence of CNTs as evidenced by their featureless spectra (not shown). The Raman spectra of products obtained from reactions catalyzed by Fe–MCM-41 (1 wt %) also showed a similar result (not shown). The absence of any of the characteristic bands of CNTs in these products suggests that reactions involving these catalysts result in the formation of undesired carbonaceous species. This conclusion was also reached after the samples were studied by HR-TEM. The Raman spectra of products obtained from reactions over Fe–MCM-41 (2 wt %) and Fe–MCM-41 (3 wt %) are shown in Figure 9. Product formed over Fe–MCM-41 (2 wt %) shows a distinct G-band, which is accompanied by the presence of an RBM (insert of Figure 9), while that formed over Fe–MCM-41 (3 wt %) shows a G-band of comparatively low intensity and no RBM. There are several RBM peaks in the range of 175−333 cm⁻¹, which corresponds to SWNT diameters in the range of 0.67−1.28 nm on the basis of the following relationship, $\omega_r =$
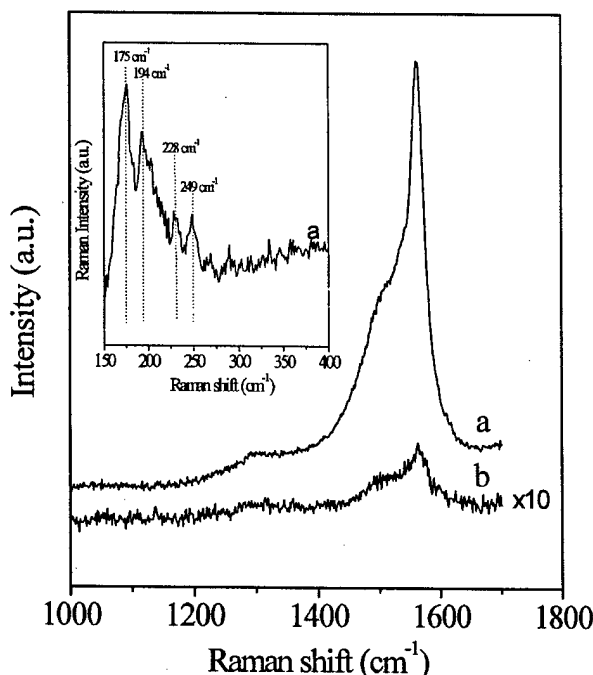

Figure 9. Raman spectra of CNTs synthesized over Fe–MCM-41 containing 2 wt % Fe (a) and 3 wt % Fe (b) at 800 °C for 1 h using reactant flow rate of 200 sccm.

223.75 (cm⁻¹ nm)/d (nm),[39] where ω_r and d are the RBM frequency and the tube diameter, respectively. It is expected that if other tube diameters are present they cannot be detected with a single wavelength experiment (532 nm) because of their diameter-dependent resonances. Thus, the range of the diameter distribution of these CNTs cannot be determined. The relatively low intensity of the D-band observed in both spectra illustrates the absence of large amounts of amorphous carbon if reactions are carried out at these optimized conditions. It is evident from this result that under these reaction conditions, Fe–MCM-41 (2 wt %) shows selectivity for SWNT production while Fe–MCM-41 (3 wt %) are selective for MWNT production. Even though the source of colloidal silica affected the activity of Fe–MCM-41, no noticeable difference in their selectivity for CNT production was observed. The Fe loading and the local environment of Fe in MCM-41 were observed to be key factors in determining selectivity toward CNTs.

Figure 10 shows representative HR-TEM images of the products of the reaction over siliceous MCM-41 and Fe–MCM-41 containing various Fe loadings. Amorphous carbon was the main carbon material observed in the products of reactions catalyzed by Si–MCM-41 and Fe–MCM-41 (1 wt %) as shown in their TEM micrographs (Figure 10a and 10b). However, some graphitic materials were observed in the products obtained from reactions catalyzed by Fe–MCM-41 (1 wt %). We observed mostly bundles of SWNT (Figure 10c and 10d) along with fewer individual SWNTs in the products obtained from reactions catalyzed by Fe–MCM-41 (2 wt %). Also, some MWNTs covered with amorphous carbon were observed. The TEM image of product of reaction catalyzed by Fe–MCM-41 (3 wt %) shows the presence of large Fe metal particles with a graphitic layer covering (Figure 10e). Although not shown here, MWNTs were also observed for this catalyst. The actual amount of CNTs present in these products has not been determined because of the difficulty associated with the quantification of CNTs. However, on the basis of TEM studies, qualitative thermogravimetric analysis, and Raman spectroscopy (low D/G band ratio),
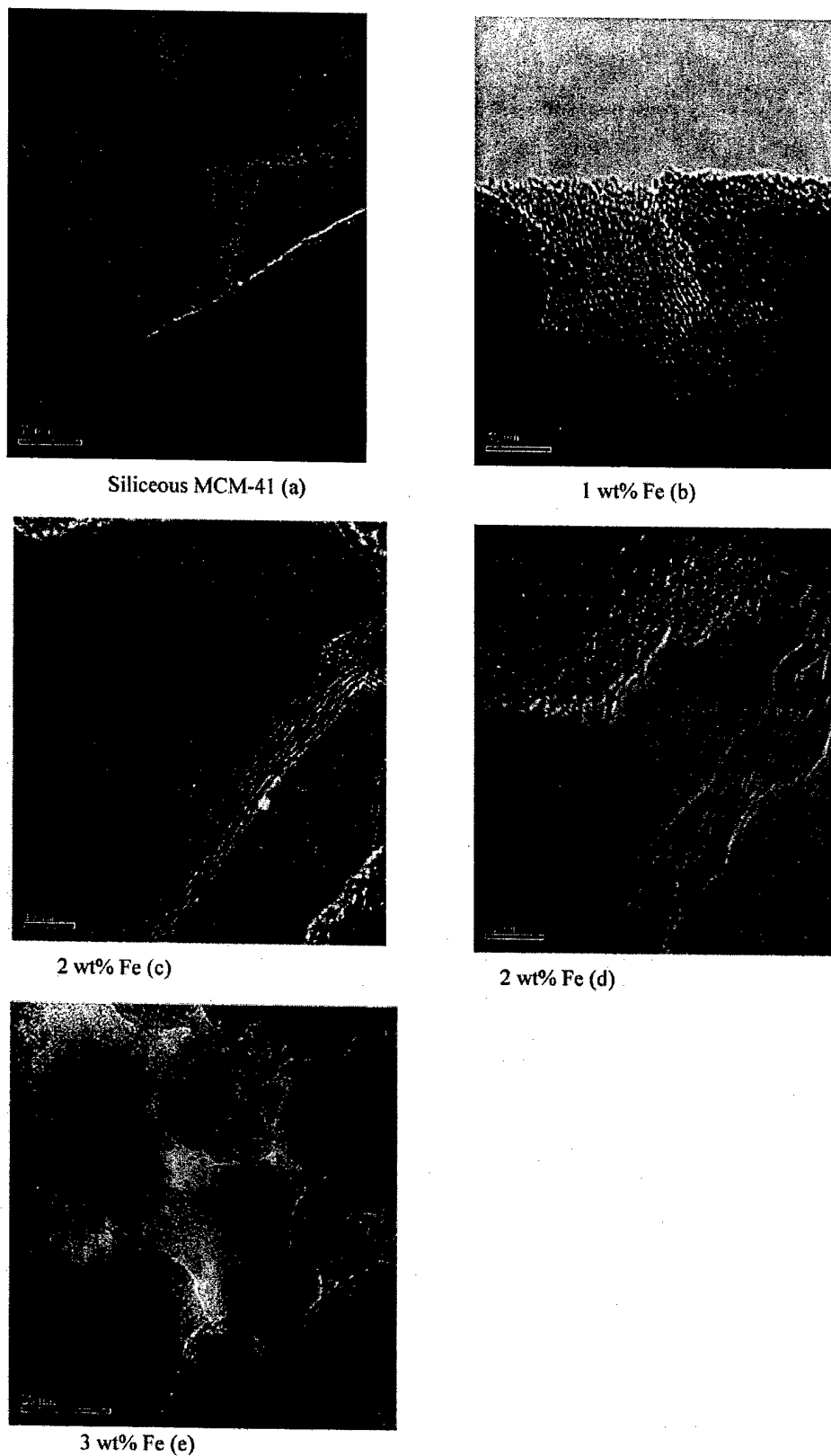
Synthesis and Characterization of Fe−MCM-41

J. Phys. Chem. B, Vol. 109, No. 7, 2005 **2653**

Siliceous MCM-41 (a)

1 wt% Fe (b)

2 wt% Fe (c)

2 wt% Fe (d)

3 wt% Fe (e)

Figure 10. HR-TEM micrographs of carbon products formed over the various catalysts as labeled.

large amounts of CNTs of relatively high quality and purity were produced.

Local Environment of Fe after Reaction. The catalytic templates (Fe-incorporated MCM-41 with different loadings) were characterized by EPR at 60 K to probe the local environment and state of Fe after the reaction. Figure 11 shows the EPR spectra of the different catalysts before and after the reaction. As mentioned previously, the EPR signal corresponding to $g = 4.3$ is ascribed to high-spin Fe^{3+} species in distorted tetrahedral coordination. For all the fresh catalysts, the intensities
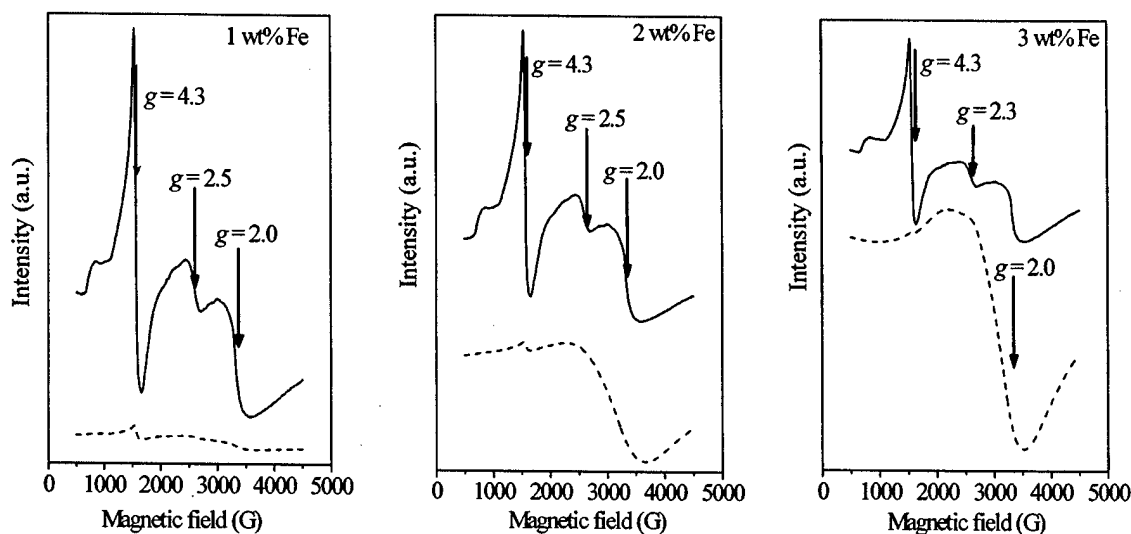
2654 *J. Phys. Chem. B, Vol. 109, No. 7, 2005*

Amama et al.

Figure 11. EPR spectra of Fe—MCM-41 containing 1 wt % Fe (a), 2 wt % Fe (b), and 3 wt % Fe (c) recorded at 60 K before (bold lines) and after (dashed lines) reaction.
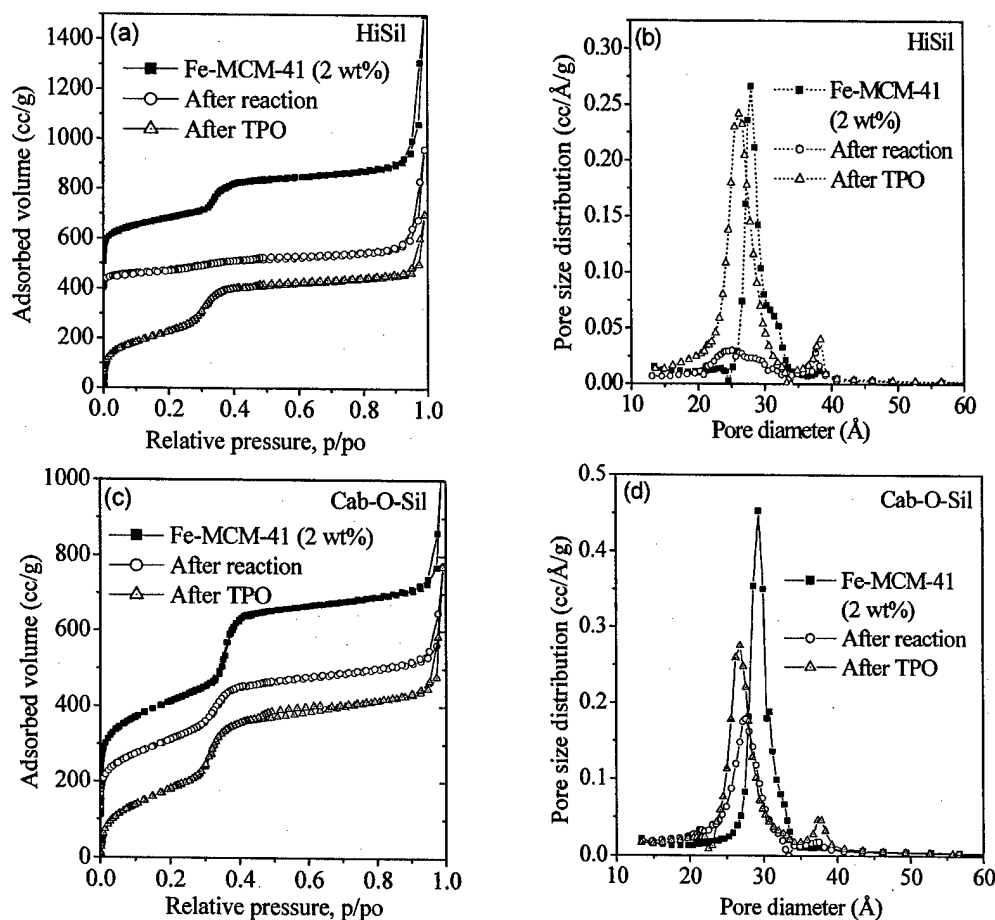

Figure 12. N_2 adsorption—desorption isotherms and their respective pore size distributions of Fe—MCM-41 (2 wt %) after reaction and carbon removal (TPO) synthesized from HiSil (a) and (b) and Cab-O-Sil (c) and (d).

of the $g = 4.3$ signals are higher than their corresponding $g = 2.0$ signal. This is, however, not the case for the used catalyst particularly for catalysts containing ca. 2 and 3 wt % Fe as the intensities of their $g = 2.0$ signals become dramatically higher than their $g = 4.3$ signal. It was also observed that the $g = 4.3$ signal diminished for catalysts containing ca. 1 and 2 wt % Fe after the reaction, and for catalysts containing 3 wt % Fe this

signal disappears completely. This reveals that the Fe^{3+} species still exist in tetrahedral environment for catalysts containing ca. 1 and 2 wt % Fe even after the reaction. The migration of Fe^{3+} species of Fe—MCM-41 from its framework positions to extraframework environment increases in the following order of Fe amount in synthesis gel: 1 wt % Fe < 2 wt % Fe < 3 wt % Fe. In situ reduction of Fe by the hydrogen produced during

Synthesis and Characterization of Fe—MCM-41

J. Phys. Chem. B, Vol. 109, No. 7, 2005 **2655**

acetylene decomposition is believed to occur, and this process is responsible for the formation of metallic Fe, which likely provides the "seeds" for SWNT nucleation. As observed in a recent study,[37] the size of the metallic clusters formed is determined by the radius of curvature of the pore size of MCM-41. The mechanism associated with the formation of these metal clusters in MCM-41 has been addressed in another study.[38] Reduction may induce the migration of Fe species from framework to extraframework environment. In general as observed in Fe-silicates, upon reduction the $g = 4.3$ signal should decrease in intensity while its corresponding $g = 2.0$ signal should increase. However, it is of interest that in situ reduction had very little effect on Fe—MCM-41 (1 wt %) as shown in their EPR spectra (Figure 11a) probably because of the higher stability of Fe in the framework. The signal at $g = 2.5$ for all samples disappears after the reaction and indicates the reduction of these surface iron oxide species to metallic Fe.

Stability of Fe—MCM-41. For Fe—MCM-41 to be used as good catalytic templates for CNTs synthesis, it is important that it shows good stability under the reaction conditions which include carbon deposition at high temperature and oxidation. The structural stability of Fe—MCM-41 (2 wt %) after reaction and temperature-programmed oxidation (TPO) was assessed by N_2 physisorption, Figure 12. Catalysts synthesized from Cab-O-Sil were more stable and maintained their high mesoporous structural integrity after the reaction better than those synthesized from HiSil. The N_2 adsorption—desorption isotherm of the former still showed a distinct capillary condensation step at p/p_0 of ~3.5 (highest slope = 1330) while the latter showed an inconspicuous step (highest slope = 239). After the reaction, Fe—MCM-41 (Cab-O-Sil) still maintained a fairly narrow PSD as the fwhm increased from 1.72 Å for fresh catalyst to 3.84 Å while that of Fe—MCM-41 (HiSil) shows a broad PSD, evidenced by the dramatic increase in the fwhm from 2.29 Å to 9.31 Å. This suggests that the uniform mesoporous structure of the HiSil catalyst is either destroyed or the pores are largely blocked after carbon deposition. As shown in Table 2, the carbon yields obtained for reactions catalyzed by Fe—MCM-41 (Cab-O-Sil) and Fe—MCM-41 (HiSil) containing 2 wt % Fe were 9.84 and 10.55 wt %, respectively. The difference in carbon yields of these samples is quite insignificant and does not seem to account for the loss of porosity of Fe—MCM-41 synthesized from HiSil. As expected, there was a general decrease in the pore diameter, pore volume, and S_{BET} upon carbon deposition as shown in Table 1. This decrease was much higher for Fe—MCM-41 (HiSil) samples. After carbon removal via TPO in air between 373 and 1173 K at 10 K/min, a recovery of their high mesoporous structural order was observed. After TPO, the maximum slopes of the inflection step for catalyst synthesized from HiSil and Cab-O-Sil became 2016 and 3099 while their fwhm of their PSDs also decreased to 3.73 Å and 2.84 Å, respectively. The recovery of mesoporosity of the Fe—MCM-41 (HiSil) demonstrates almost complete pore blockage after carbon deposition but not destruction of the pore structure.

Conclusions

There is an improvement in the structural order of siliceous MCM-41 upon the incorporation of 1 wt % Fe as a result of the knitting effect, but it diminishes as more Fe is incorporated. Catalysts synthesized from Cab-O-Sil showed higher structural order and higher stability during acetylene pyrolysis than catalysts synthesized from HiSil. Fe^{3+} species in all of the as-synthesized samples were found in the framework environment. Calcination causes the dislodgement of the Fe^{3+} species from

framework location and this effect is more severe for catalysts with ca. 2 and 3 wt % Fe. Fe^{3+} species occupying tetrahedral coordination decreases with increasing Fe loading.

This work reveals that Fe—MCM-41 (2 wt %) exhibits high selectivity for CNTs production under our optimized conditions (1073 K, 200 cm³/g-min C_2H_2/N_2, reaction duration of 1 h). Bundles or individual SWNTs in large amounts are obtained. Fe—MCM-41 (3 wt %) exhibit much lower selectivity toward CNT production and those formed are MWNT. Fe—MCM-41 (1 wt %) is not selective for CNT production. The relationship between the amount of Fe incorporated in MCM-41 and the carbon species produced during acetylene pyrolysis has therefore been established. Compared to the CO disproportionation process over Co—MCM-41, the acetylene pyrolytic process over Fe—MCM-41 provides lower selectivity to a narrow tube size distribution but very high overall yield.

Spectroscopic studies (EPR) of the catalysts after reaction revealed that Fe^{3+} species in Fe—MCM-41 (1 wt %) remained mainly in the framework and this partly accounts for its poor selectivity for CNTs. Fe^{3+} species in Fe—MCM-41 (2 wt %) appears to be well distributed in both framework and extra-framework environments. On the other hand, Fe^{3+} species in Fe—MCM-41 (3 wt %) are well reduced and exist mainly in extraframework locations.

References and Notes

(1) (a) Kresge, C. T.; Leonowicz, M. G.; Roth, W. J.; Vartuli, J. C.; Beck, J. S. *Nature (London)* **1992**, *359*, 710. (b) Beck, J. S.; Vartuli, J. C.; Roth, W. J.; Leonowicz, M. E.; Kresge, C. T.; Schmit, K. D.; Chu, C. T.-W.; Olson, D. H.; Sheppard, E. W.; McCullen, S. B.; Higgins, J. B.; Schlenker, J. L. *J. Am. Chem. Soc.* **1992**, *114*, 10834.

(2) Corma, A. *Chem. Rev.* **1997**, *97*, 2373.

(3) (a) Iijima, S. *Nature* **1991**, *354*, 56. (b) Huczko, A. *Appl. Phys. A* **2002**, *74*, 617.

(4) Lim, S.; Ciuparu, D.; Pak, C.; Dobek, F.; Chen, Y.; Harding, D.; Pfefferle, L.; Haller, G. *J. Phys. Chem. B* **2003**, *107*, 11048.

(5) Ciuparu, D.; Chen, Y.; Lim, S.; Haller, G. L.; Pfefferle, L. *J. Phys. Chem. B* **2004**, *108*, 503.

(6) (a) Li, Y.; Kim, W.; Zhang, Y.; Rolandi, M.; Wang, D.; Dai, H. *J. Phys. Chem. B* **2001**, *105*, 11424. (b) Li, W. Z.; Xie, S. S.; Qian, L. X.; Chang, B. H.; Zou, B. S.; Zhou, W. Y.; Zhao, R. A.; Wang, G. *Science* **1996**, *274*, 1701.

(7) Hernadi, K.; Fonseca, A.; Nagy, J. B.; Bernaerts, D.; Lucas, A. A. *Carbon* **1996**, *34*, 1249.

(8) Hernadi, K.; Fonseca, A.; Nagy, J. B.; Siska, A.; Kiricsi, I. *Appl. Catal., A* **2000**, *199*, 245.

(9) Kong, J.; Cassele, A. M.; Dai, H. *Chem. Phys. Lett.* **1998**, *292*, 567.

(10) Rao, C. N. R.; Satishkumar, B. C.; Govindaraj, A.; Nath, M. *Chem. Phys. Chem.* **2001**, *2*, 78.

(11) Pérez-Cabero, M.; Rodríguez-Ramos, I.; Guerrero-Ruiz, A. *J. Catal.* **2003**, *215*, 305.

(12) Duxiao, J.; Nongyue, H.; Yuanying, Z.; Chunxiang, X.; Chunwei, Y.; Zuhong, L. *Mater. Chem. Phys.* **2001**, *69*, 246.

(13) Willems, I.; Kónya, Z.; Colomer, J.-F.; Van Tendeloo, G.; Nagaraju, N.; Fonseca, A.; Nagy, J. B. *Chem. Phys. Lett.* **2000**, *317*, 71.

(14) Kulovecz, A.; Kónya, Z.; Nagaraju, N.; Willems, I.; Tamási, A.; Fonseca, A.; Nagy, J. B.; Kiricsi, I. *Phys. Chem. Chem. Phys.* **2000**, *2*, 3071.

(15) Müller, T. E.; Reid, D. G.; Hsu, W. K.; Hare, J. P.; Kroto, H. W.; Walton, D. R. M. *Carbon* **1997**, *35*, 951.

(16) Huang, L.; Wind, S. J.; O'Brien, S. P. *Nano Lett.* **2003**, *3*, 299.

(17) Coquay, P.; Vandenberghe, R. E.; De Grave, E.; Fonseca, A.; Piedigrosso, P.; Nagy, J. B. *J. Appl. Phys.* **2002**, *92*, 1286.

(18) Ivanov, V.; Fonseca, A.; Nagy, J. B.; Lucas, A.; Lambin, P.; Bernaerts, D.; Zhang, X. B. *Carbon* **1995**, *33*, 1727.

(19) Lim, S.; Haller, G. L. *J. Phys. Chem. B* **2002**, *106*, 8437.

2656 *J. Phys. Chem. B, Vol. 109, No. 7, 2005*

Amama et al.

(20) Barrett, E. P.; Joyner, L. G.; Halenda, P. P. *J. Am. Chem. Soc.* **1951**, *73*, 373.

(21) Lakshmi, K. V.; Eaton, S. S.; Eaton, G. R.; Frank, H. A.; Brudvig, G. W. *J. Phys. Chem. B* **1998**, *102*, 8327.

(22) Ratnasamy, P.; Kumar, R. *Catal. Today* **1991**, *9*, 329.

(23) Wang, Y.; Zhang, Q.; Shishido, T.; Takehira, K. *J. Catal.* **2002**, *209*, 186.

(24) Gregg, S. J.; Sing, K. S. W. *Asorption, Surface Area and Porosity*; Academic Press Inc.: London, 1982.

(25) Yang, Y.; Lim, S.; Wang, C.; Harding, D.; Haller, G. *Microporous Mesoporous Mater.* **2004**, *67*, 245.

(26) Echchahed, B.; Moen, A.; Nicholson, D.; Bonneviot, L. *Chem. Mater.* **1997**, *9*, 1716.

(27) Bordiga, S.; Buzzoni, R.; Geobaldo, F.; Lamberti, C.; Giamello, E.; Zecchina, A.; Leofanti, G.; Petrini, G.; Tozzola, G.; Vlaic, G. *J. Catal.* **1996**, *158*, 486.

(28) Samanta, S.; Giri, S.; Sastry, P. U.; Mal, N. K.; Manna, A.; Bhaumik, A. *Ind. Eng. Chem. Res.* **2003**, *42*, 3012.

(29) Tuel, A.; Arcon, I.; Millet, J. M. M. *J. Chem. Soc., Faraday Trans.* **1998**, *94*, 3501.

(30) Berlier, G.; Spoto, G.; Fisicaro, P.; Bordiga, S.; Zecchina, A.; Giamello, E.; Lamberti, C. *Microchem. J.* **2002**, *71*, 101.

(31) Goldfarb, D.; Bernardo, M.; Strohmaier, K. G.; Vaughan, D. E. W.; Thomann, H. *J. Am. Chem. Soc.* **1994**, *116*, 6344.

(32) Stockenhuber, M.; Hudson, M. J.; Joyner, R. W. *J. Phys. Chem. B* **2000**, *104*, 3370.

(33) Berry, A.; O'Neill, H. C.; Jayasuriya, K. D.; Campbell, S. J.; Foran, G. *J. Am. Miner.* **2003**, *88*, 967.

(34) Lin, H.-Y.; Chen, Y.-W.; Li, C. *Thermochim. Acta* **2003**, *400*, 61.

(35) Lim, S.; Ciuparu, D.; Chen, Y.; Pfefferle, L.; Haller, G. L. *Top. Catal.* (In Press).

(36) (a) Liu, B. C.; Lyu, S. C.; Jung, S. I.; Kang, H. K.; Yang, C.-W.; Park, J. W.; Park, C. Y.; Lee, C. J. *Chem. Phys. Lett.* **2004**, *383*, 104. (b) Ci, L.; Xie, S.; Tang, D.; Yan, X.; Li, Y.; Liu, Z.; Zou, X.; Zhou, W.; Wang, G. *Chem. Phys. Lett.* **2001**, *349*, 191. (c) Bladh, K.; Falk, L. K. L.; Rohmund, F. *Appl. Phys. A* **2000**, *70*, 317.

(37) Lim, S.; Ciuparu, D.; Chen, Y.; Yang, Y.; Pfefferle, L.; Haller, G. L. *J. Phys. Chem. B* **2004**, ASAP DOI: 10.1021/jp048881(+).

(38) Ciuparu, D.; Chen, Y.; Lim, S.; Yang, Y.; Haller, G. L.; Pfefferle, L. *J. Phys. Chem. B* **2004**, *108*, 15565.

(39) Bandow, S.; Asaka, S.; Saito, Y.; Rao, A. M.; Grigorian, L.; Richter, E.; Eklund, P. C. *Phys. Rev. Lett.* **1998**, *80*, 3779.